Title

Cell morphology and cell-fluid interactions affects colony strategy and propagation in Serratia marcescens swarms

Permalink

Author

Tamayo, Joshua C

Publication Date

2024

Peer reviewed|Thesis/dissertation

UNIVERSITY OF CALIFORNIA, MERCED

Cell morphology and cell-fluid interactions affects colony strategy and propagation in *Serratia marcescens* swarms

A dissertation submitted in partial satisfaction of the

requirements for the degree

Doctor of Philosophy

in

Bioengineering

by

Joshua Tamayo

Committee in charge:

Professor Victor Muñoz, Chair
Professor Miriam Barlow
Professor Arvind Gopinath
Professor Joel Spencer

2024

The dissertation of Joshua Tamayo is approved, and it is acceptable in quality and form for publication on microfilm and electronically:

_____
(Professor Miriam Barlow)

_____
(Professor Arvind Gopinath)

_____
(Professor Joel Spencer)

_____
(Professor Victor Muñoz, Chair)

University of California, Merced

2024

TABLE OF CONTENTS

LIST OF FIGURES

LIST OF TABLES

ACKNOWLEDGEMENTS

Thank you to my advisor, Dr. Arvind Gopinath, for all the support, knowledge, and intriguing discussions we've had over the past 8 years. We met my first semester at UC Merced in Fall of 2016; I took his thermodynamics course where he talked about his research interest in studying active matter. I reached out to him toward the end of the course, and thus, my pathway into academic research began by analyzing the passive-active interfaces and tracking of particles that became a part of this dissertation. After my Bachelors, I joined the Bioengineering PhD program and we continued to work together. From there, I experienced a whole new world of science, and the hard work and rigor that goes into it. We spent many times discussing projects and nearly every time we talked, I got to learn something new and interesting. Thank you for your time and effort into helping me complete this PhD and making me a better scientist.

Thank you loving my dad and sister: to you both I owe everything. Thank you for raising the person I am today. To dad, I cannot imagine raising two kids by yourself and sending both to college. I'm not sure of your thoughts at the time when I told you I was still going to continue staying at the university as a PhD student, but you un-apologetically supported my decision which gave me motivation to keep moving forward. To ate, thank you being there every step of the way, holding down the fort, and supporting me. My only wish is to support you in each and every one of your own endeavors. To Owen, I wish you were still here to see this! You wouldn't have cared for the diploma, but you would have been excited for all the food during the celebrations. You were the best dog, and I miss and love you so much.

Elaine, thank you for being there every step of the way. Thank you for making the days bearable, the successes sweeter, and the hardships easier to manage. Thank you for standing by my victories, and holding me up when I felt defeated. Even though our lives were miles apart from each other, we still held it together. Thank you for listening to me when I was frustrated and holding me when I cried from the stress. I can't wait for our future together and what's in store next.

Thank you to Dr. Alison Patteson for allowing me to learn and work in your lab for two summers, learning the tools and tricks of the trade. Thank you to Dr. Merrill Asp, who at the time, was a PhD candidate himself. He taught me with care and patience, and also gave me someone to talk to about swarms and active matter.

Special thanks go to everyone in both the Gopinath and Subramaniam labs. From enriching discussions about science to late evenings and to weekend work, thank you all for making work fun and being great people. Special thanks to Alexis Cooper, who I am happy to have met and happy to call a friend. Your discussions, quips, complaints, and banter have made the last few years bearable and special. I look forward to referring each other as "Doctor" in the future.

Thank you to my committee, Professors Victor Munõz, Joel Spencer, and Miriam Barlow for their guidance and discussions throughout my PhD.

Thank you to all the other friends and family who have supported me throughout this journey and are simply too many to thank and acknowledge in this section. Every conversation, every nudge of support has been received.

The research in **chapter 2** of this dissertation is a part of the preprint "Swarming bacterial fronts: Dynamics and morphology of active swarm interfaces propagating through passive frictional domains" hosted on bioRxiv. Initial experiments and analysis presented in **chapter 2** of *Serratia marcescens* were conducted by Dr. Alison Patteson (Syracuse University), and by Dr. Arvind Gopinath. Further analysis, especially related to the plots on roughness was conduced by me. The self-propelled rod (SPR) model introduced in **chapter 2** was extended to bacterial systems with specific steric interactions by Dr. Arezoo Ardekani (Purdue University) and Dr. Arvind Gopinath, and initially implemented by Dr. Ardekani's group. The code was adapted by me to study diluted swarms in Newtonian fluids, with results presented in Chapter 3. I have indicated specific contributions in-text where relevant. The work presented in **chapter 4** has been published ("Size-Dependent Diffusion and Dispersion of Particles in Mucin" 2023, *Polymers*), with co-author Dr Parveen Kumar, and I contributing equally to the experiments and the coding.

Curriculum Vitae

Education

Fall 2024	Ph. D, Bioengineering, University of California, Merced
2018	B. S., Mechanical Engineering University of California, Merced

Publications

Tamayo J., Zhang Y., Patteson A., Ardekani A., Gopinath A. Factors affecting the persistence of clusters in diluted swarms (*Royal Society Interface*, in preparation)

Tamayo J., Zhang Y., Patteson A., Ardekani A., Gopinath A. Swarming bacterial fronts: Dynamics and morphology of active swarm interfaces propagating through passive frictional domains (*Soft Matter*, in review)

Fylling, C., **Tamayo, J.**, Gopinath, A., & Theillard, M. (2024). Multi-population dissolution in confined active fluids. *Soft Matter*, 20(7), 1392–1409. doi:10.1039/d3sm01196h

Kumar P., **Tamayo J.**, Shiu R.-F., Chin W.-C., Gopinath A. (2023). Size-Dependent Diffusion and Dispersion of Particles in Mucin. *Polymers*, 15(15), 3241. doi:10.3390/polym15153241

Tamayo J., Mishra A., Gopinath A. (2022). Ambient Fluid Rheology Modulates Oscillatory Instabilities in Filament-Motor Systems. *Frontiers in Physics*, 10, 895536. doi:10.3389/fphy.2022.895536

Presentations

Tamayo J., 2024, "Survival as a swarm: Cell morphology, cell-fluid interactions, and substrate properties affect colony strategy and propagation in Serratia marcescens swarms", BIOE Young Investigator's Symposium, Keynote talk

Tamayo J., Ardekani A., Patteson A., Gopinath A., 2023, "The Role of Hydrodynamic Interactions in Modulating Persistent Structural Features in Bacteria Swarms", American Institute of Chemical Engineers 2023 Annual Meeting, Orlando, FL, USA, Oral Presentation

Kumar P., **Tamayo J.**, Shiu R.-F., Chin W.-C., Gopinath A., 2023, "Size-Dependent Diffusion and Dispersion of Particles in Mucin", Biomedical Engineering Society Annual Meeting, Seattle, WA, USA, Poster Presentation

Tamayo J., Ardekani A., Patteson A., Gopinath A., 2022, "Bacterial Swarm Simulations Highlight the Roles of Hydrodynamic Interactions, Cell Morphology and Steric Interactions on Emergent Patterns", CCBM Workshop 2022: Synthetic Biology and Mimetics, Poster Presentation

Tamayo J., Ardekani A., Patteson A., Gopinath A., 2022, "Bacterial Swarm Simulations Highlight the Roles of Hydrodynamic Interactions, Cell Morphology and Steric Interactions on Emergent Patterns ", American Institute of Chemical Engineers 2022 Annual Meeting, Phoenix, Arizona, Oral Presentation

Tamayo J., Gopinath A., 2022, "Hydrodynamic simulations of bacterial swarms highlight the role of cell morphology and cell-cell interactions on emergent patterns", APS March Meeting, Chicago, IL, Oral Presentation

Fellowships & Awards

Spring 2024	Graduate Dean's Dissertation Fellowship
Spring 2024, Fall 2022	Graduate Student Association Travel Award
Summer 2023	CCBM Summer Fellowship
Fall 2022-Spring 2023, Fall 2019 - Fall 2021	CCBM Graduate Student Scholar
Summer 2023, 2022, Summer 2021, 2020	BIOE Bobcat Fellowship
Fall 2022	CCBM Travel Award

Service & Outreach

Summer 2023	**CCBM-CREST STEM Camp** Session leader/presenter
Summer 2022	**CCBM Summer Outreach Fellow**
Nov. 2021, Oct. 2020	**Fresno American Indian Health Project** Group leader/presenter
Summer 2020	**CCBM Virtual Sessions** Guest Lecturer

Teaching

Fall 2023	Biomechanics - BIOE 115
Spring 2022	Introduction to Material Science - ENGR 045
Fall 2021, Fall 2019	Computing for Bioengineers - BIOE 021
Spring 2020	Research Methods in Cognitive Science - COGS 105

ABSTRACT OF THE DISSERTATION

Cell morphology and cell-fluid interactions affects colony strategy and propagation in *Serratia marcescens* swarms

by

Joshua Tamayo

Doctor of Philosophy in Bioengineering

University of California Merced, 2024

Professor Arvind Gopinath, Dissertation Advisor

Professor Victor Muñoz, Committee Chair

Swarming is a multicellular mode of motility common to flagellated bacteria species which enables coordinated rapid surface translocation, expansion, and colonization. Swarming typically follows bacterial cells changing phenotype from planktonic to elongated and hyper-flagellated states and is triggered by the presence of soft elastic, and permeable surfaces. These motile and multi-cellular bacteria colonies display characteristics uniquely representative of wet active matter systems, including intense fluctuating vortices, self-emergent long-ranged velocity fields, and persistent flocks. In this dissertation, I report on dense and semi-dense suspensions of the canonical swarming species, *Serratia marcescens* under various conditions when hydrodynamic interactions between bacterial cells is important. First, I present experimental and computational studies of dense swarm front interacting with and moving through domains of immotile bacteria that resist motion. I show that the active-passive swarm interface in this system has unique morphological features that are critically dependent on the relative importance of hydrodynamic interactions. The swarm region adjacent to the boundary develops spatially periodic and transient vortices of alternating sense that continuously convect immotile cells away from the interface, allowing for the active swarm to move into that territory. Additionally, the roughness of the evolving interface exhibits partial self-similar features that I compare with classical, continuum interface models. Motivated by the important role played by hydrodynamics in dense swarms, I next present experimental and computational results relevant to dilute systems such as the pre-swarming state or bacterial cells in the vicinity of a free interface. Here the object is to focus on the role of cell length and hydrodynamics and identify their individual and synergistic impacts on emergent collective motion. To complement experimental data, and circumvent the difficulty in devising experiments that decouple these effects, I explore the role of cell aspect ratio, cell-cell interactions, and hydrodynamics using a minimal agent-based model that treats the swarm as a suspension of self-propelled active rods (cells) moving in a plane. These *in silico* swarmers have tunable cell size, aspect ratio, cell-cell interactions, and fluid mediated hydrodynamic interactions that allow for exploration of these effects independently and in combination. I find that an increase in aspect ratio enhances overall cluster size and cluster persistence time. Hydrodynamic effects have a mixed effect and may either stabilize emergent structural features or weaken them. Strong hydrodynamic interactions can destabilize large-scale structures, due to significant fluid and velocity gradients that depress and prevent persistent clustering. I conclude this dissertation with a chapter detailing the workflow to image, segment, and analyze immotile *Serratia marcescens* as they

proliferate, elongate, and form motile multi-cellular forms ranging from small clusters to large correlated swarming domains. This workflow will aid significantly in future investigations into the physical mechanisms that initiate the swarming process, as well help quantity these living active polar nematic systems.

Chapter 1

Introduction

1.1 Swarming motility allows for faster propagation

Bacteria species present themselves in many morphologies in nature, ranging from spherical-shaped (cocci) to rod-shaped cells. *Serratia marcescens* is gram-negative, flagellated, rod-shaped bacteria species that commonly presents itself in damp areas and may be identified by its pink pigment in these types of environments [1]. The typical length of isolated cells ranges from 0.5-4 μm with a width of approximately 1 μm as indicated by Table 1.1 and illustrated in figure 1.1(a). The speeds of these cells are measured to be approximately 20 μm/s and comparable to other flagellated, rod-shaped bacteria species. Single, isolated cells typically migrate through liquid environments by swimming. For these flagellated bacteria, they propel themselves forward by rotating their flagella counter-clockwise at frequencies $\geq$ 100 Hz to generate thrust [2, 3, 4]. This swimming behavior is commonly referred to as *run-and-tumble motility*, where the bacteria propel themselves forward in a "run", then suddenly reorient themselves in a random direction [5]. Measured run times are $\approx$ 1s and tumble times are $\approx$ 0.1s [6, 7]. This type of motility does not allow for efficient transportation through a medium or surface which colonies require for nutrient acquisition and proliferation.

To overcome this limitation, *S. marcescens* and other flagellated bacteria alter their morphologies to initiate swarming migration or *swarming* for short. Swarming is a multicellular mode of flagella-based motility [8, 9] featuring collective long-ranged flows that allows bacterial colonies to rapidly and efficiently cover and subsequently colonize surfaces [1, 10, 11, 12, 13, 14, 15, 16, 17, 18]. Unlike swimming, which is a 3D movement in a fluid, swarming is a form of surface translocation where a solid surface is a key requirement. The swarming response can be initiated by transferring planktonic free-swimming bacteria in liquid media to soft agar gels. Typically, this range is between 0.5-1.0% agar as anything below that range, cells penetrate the large pores and swim through the substrate while above that range, colonies prefer to form biofilms. This process results in a change to bacterial phenotypes that are morphologically different from their swimming kin as swarmers elongate and hyperflagellate [1, 13]. The drastic change in morphology is highlighted in figure 1.1(b).

1.1.1 Surface tension reduction and surfactant production in swarmers

As a colony grows, its community collectively extracts fluid from the substrate by releasing osmolytes into the substrate [19] in order to form a thin layer of fluid that lubricates and reduces surface tension, allowing for rapid movement [9]. The secretion of osmolytes alters the osmotic pressure of the substrate across distances much higher than the length of a bacteria. Approximately 30 μm in front of the leading edge, the osmotic pressure draws fluid from the substrate, which subsequently is drawn back in and delivered to the swarm $\approx$ 120 μm from the edge, in the direction of the center of the colony [20]. In addition to the fluid, *S. marcescens* and a few other species can create surfacatants to further reduce surface tension and aid in movement [21, 22]. *S. marcescens* creates its own surfactant, *serrawettin* [23, 24]. In *E. coli*, surfactant production reduces cell speed to nearly stationary at the upper edge (air-liquid interface) of the swarm [25]. *Serratia* utilize surfactant in a similar manner. With surfactant present, cells are nearly non-motile at the air-liquid interface [26]. For *Serratia* in particular, it has been suggested that its surfactant production reduces tumble bias [27]. The benefit of surfactant production in *Serratia* is when antibiotics are present at the substrate surface. In the presence of surfactant, bacteria migrate away from the antibiotic surface and form a protective avoidance zone that minimizes their exposure to the antibiotic and increases colony fitness. The addition of exogenous surfactant is also of interest, as it can restore swarming ability in mutants defective of producing surfactant. Using a non-species specific surfactant in agar substrates, the spread of *P. aeruginosa* was increased and the flagellated and pililated WT strain was able to spread similarly to pili-less (ΔPilA) mutants [21]. This particular mode of motility is highly relevant to understanding infectious diseases caused by these bacteria [28, 29] and their ability
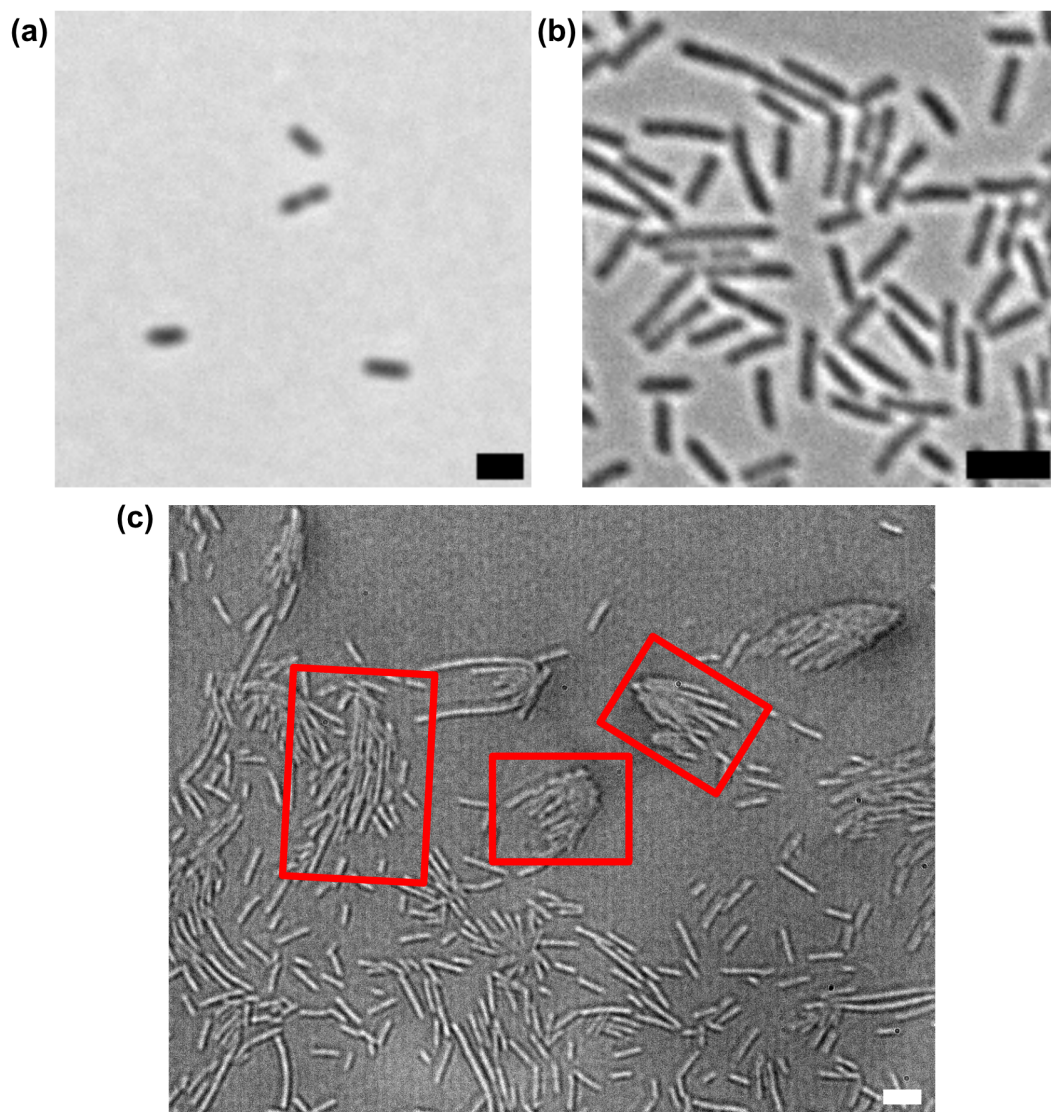
Figure 1.1: Morphological differences between swimming (a) and swarming (b) *Serratia marcescens.* (c) In the swarming state, bacteria form rafts (indicated by red boxes) of aligned cells and aid their rapid surface motility. The scale bar in (a) is 3 μm, (b) is 5 μm, and in (c) is 10 μm. (a) and (b) were imaged at 40x magnification (NA = 0.6) on 0.5% agar on a Zeiss Axioimager.A2. (c) was imaged at 30x magnification (NA = 0.45) on 0.6% agar on a Nikon Eclipse Ti-U.

to develop antibiotic resistance [30, 31, 32].

1.2 Morphological changes in bacteria swarmers

1.2.1 Bacteria elongate when transitioning to the swarming phenotype

Elongation in bacteria species is hypothesized to be due to defects in cell division, as seen in Kearns et al., where stains of swarming *Bacillus subtilis* (WT 3610) revealed some morphological changes and forming of filaments of multinucleoid cells [33]. However, the exact mechanism of elongation is unclear and may vary between different species of swarmers. To better quantify these morphological changes, researchers describe the morphology of swarmers by their aspect ratio. I define in this disseration the aspect ratio in this dissertation as the ratio of length-to-width of the cell, $A = L/\lambda$ where L is the length of a bacteria cell or rod along its major axis and λ is the width of a cell. Table 1.1 gives an overview of the morphological differences between swimming and swarming *E. coli* and *S. marcescens*. Cell width is typically maintained as cells change phenotype while length increases, hence the use to aspect ratio to describe morphology. Additionally, speeds of swarmers are dramatically increased compared to swimmers which can explain swarmer's ability to rapidly colonize surfaces. While these are average values, swarm populations have a large variation of cell lengths ranging from 3-50 μm [34] and careful consideration of density must be taken into account.

Elongation is known to influence swarm dynamics by increasing cell correlation times and increasing cell speeds at aspect ratios higher than swimming cell lengths [34]. This has the overall effect of increased fitness of the colony as the increased speeds allow for faster territory acquisition. Due to the difficulty of study, published speeds and correlation times of swarmers are associated with single sets of aspect ratios, e.g., we cannot trivially determine that a bacterium moves with a certain speed independent of adjacent cells that may be of varying lengths. Nonetheless, its clear from these studies that elongation shows an increase in mean speed compared to swimming cells [36, 34]. But, it is of importance to also note that the fastest swarmers are not the longest ones. Rather, the fastest swarmers are those of the mean WT swarming lengths. This leads to an interesting question: What purpose do highly elongated bacteria serve in a swarm?

A potential benefit to elongation aside from increased speeds is the possibility that longer length swarmers promote clustering and rafting. Swarms possess a wide distribution of bacterial lengths and have sub-populations of highly elongated bacteria. In one study by Peled et al. [37], they were able to generate a system with only two, distinct cell length populations of wild type cells (aspect ratio = 7 ± 2.2) and hyperelongated mutants (aspect ratio = 19 ± 5.6). In these systems, they found that the longer mutants act as nucleation sites for small

	Swimming *E. coli*	Swimming *S. marcescens*	Swarming *E. coli*	Swarming *S. marcescens* (WT 274)
Mean Length [μm]	2 [6]	0.5-2 [1]	3-7.6 [13]	5-30 [27]
Mean Width [μm]	1 [6]	1 [1]	1 [13]	1 [1]
Mean Speed [μm$\cdot s^{-1}$]	8.3 [7]	20 [35]	40 [13]	28 [7]

Table 1.1: Literature values for swimming (state observed of single cells swimming in liquid broth) and swarming *E.coli* and *S. marcescens*.

cells to gather and formed align clusters. The mix of cell lengths and the effect of elongation in natural swarms suggest that elongation and well as the heterogeneity of the swarms are of key importance to the overall survival and spreading of swarming bacteria colonies.

1.2.2 Hyperflagellation in swarming species

The changes in morphology of swarming species allows for another addition to the swarmer's toolkit: An increase in the number of flagella present on the cell, also known as *hyperflagellation*. As swarming only occurs in species that are flagellated, without flagella, an inoculated colony is unable to spread across a surface [38, 39]. A swimming bacteria typically has 1-7 flagella [2, 14] whereas swarming cells, upon hyperflagellating, increase their counts to 10-100 flagella [1, 14]. To propel themselves with such a numerous amount of filaments, the flagella bundle together and rotate CCW to generate torque. One might assume that the increased number of flagella would generate additional torque, however, this is found to not be true and the mean torque of both swimming and swarming bacteria strains of *E. coli* were approximately 1100 pN/nm [40]. If the torques are similar between the two phenotypes, how then are swarming cells faster than swimming cells? One key finding by Partridge et al. reports that tumbling is suppressed in multiple swarming species [27]. This bias' the cells to do longer, faster runs which enable their observed rapid motility. While much is reported and observed in regards to hyperflagellation, it is currently unclear on how the increase in flagella benefits the swarm and aids in the fitness of the colony if it does not increase the torque generated.

1.3 Factors affecting swarming ability

1.3.1 Density dependence in swarming colonies

While fully grown colonies are highly dense, multilayered communities, it is still of interest to study how swarmers at different densities interact and how their dynamics change. As swarming is a collective form of motion, density may play a crucial role in the ability to swarm. Depending on the aspect ratio, densities can induce swarming and influence the formation of small, local clusters, or larger clusters that are comprised of several dozen bacteria. A mapping of the effect of density and aspect ratio on *B. subtilis* was conducted, mapping a wide range of aspect ratios from planktonic length to hyper elongated cells at very low and very high densities ($\Psi = 0.1 - 0.7$) in monolayered systems [34]. At low bacterial densities, cells exhibit the aforementioned run-and-tumble motion. In this state, prior to swarming, no collective motion takes places as cells randomly explore their surroundings in search of nutrients. When swarming cells are diluted to densities where they can be observed in small groups, the cells exhibit collective motion, clustering, and rafting. Very low densities may inhibit swarming motion as there will be lower frequency of cell-cell interactions which are required for bacteria to cluster and move together. Very high densities, across all measured aspect ratios in the study can induce jammed states that hinder bacteria motility. This finding contracts what can be observed in actual colonies where cells are packed into multilayers, suggesting that while density does play a role, it does not completely contribute to swarming.

1.3.2 Light sensitivity of *S. marcescens*

A study by Yang et al. reported that swarm *S. marcescen* colonies can be affected by standard brightfield imaging depending on exposure time and light intensity. Regions of the active swarming colony were exposed to wide-spectrum light generated by a mercury lamp. Intensities measured were reported at a wavelength of 535 nm. Three regimes were reported

depending on the above parameters: 1) Active, unaffected cells, 2) Temporarily passivized (immobilized) cells, and 3) Permanently passivized cells. For short exposure times and relatively low intensities (≤ 40 s & at intensities ≤ 220 mW), cells are unaffected by the light. Durations exceeding 60 s and intensities > 220 mW, cells appear permanently passivized and remain immotile. Only in the narrow regime between the two phases are cells temporarily passivized. I use this information in this study to ensure that in experiments, *S. marcescens* is unaffected for my studies.

1.3.3 Swarming in confined areas

In nature, bacteria colonies are found in tortuous, highly confined environments. Colonies in such states must adapt to these conditions that restrict the individual movement of bacteria, nutrient uptake, and colony expansion. Recently, studies have imaged colony and bacterium interaction with these boundaries. The authors in [41] suggest that when confined in circular well with a diameters $\leq 80\mu m$ in diameter, swarmers can form a single large vortex, significantly larger the $20 - 25\mu m$ diameter vorticies formed in dense swarming suspensions in free space [42, 43]. The passive domain mentioned in section 1.3.2 also serves the purpose of acting as soft confinement where the movement of the active front is impeded, but not completely restricted unlike hard boundaries [43, 42]. There, the passive region can be deformed by the actively moving vorticies. The jets and streams formed by the counter-rotating, periodic vorticies convect passive cells away, freeing up room for active cells to overtake. This phenomena may not limited to systems of a single species. While not directly observed, this feature can be utilized in porous soil to move dirt and small material around, or the displacement of dead bacteria.

Looking at confinement on a scale of a bacterium, the movement and motility of a bacterium is largely affected by obstacles and the size/dimensions of said obstacles. Smooth-swimming bacteria (that are deficient in tumbling) are influenced in a periodic pillar array, either remaining trapped along the pillars or escaping depending on the cell length [44]. Short bacteria cells with lengths comparable to swimming bacteria, tend to remain along the perimeter of the pillars, trapping themselves on the pillar for several minutes. In contrast, long bacterial cells with lengths comparable to elongated swarming bacteria are not as easily trapped. Elongated cells whose lengths are similar or longer than the pillar spacing interact with adjacent pillars and orient themselves in such a way that they do not circulate. This may be analogous to dense suspensions of swarmers that prevent individual reorientation and allow for rapid, forward movement throughout their environment. These findings suggest that the collective behavior of swarmers may be affected in ways that are influenced by size and geometry of confinement. Periodic obstacles have the possibility of disrupting colony formation due to the restriction placed on local density or jamming cells.

1.4   A mesoscopic view of swarming bacteria colonies

A key ability of swarming colonies is that they are able to quickly colonize surfaces. The persistent speed of a swarm front/colony expansion rate is measured to be around 1-4 μm/s [13, 43]. Ubiquitous to swarmers are unique features and sub-populations of the colony that are segregated based on proximity to the leading edge of the swarm. Darnton et al. clearly illustrates these features with high resolution images of a swarm of *E. coli* at different positions with in the swarm. At the leading edge and at distances approximately 100 μm away from the front, the bacteria form a monolayer of cells that comprise of the highly motile, rafting cells that enable their rapid front movement. Behind the monolayer, at distances $\geq$ 100-200 μm away from the front, is a dense multilayer band of cells.

The morphology of the colony is highly species dependent, as not every swarming

species has the same mechanisms or cell morphology. *E. coli* and *S. marcescens* have a relatively smooth colony front and radially expand at a constant rate. *Proteus mirabilis* colonies presents themselves in a different manner due to their dual appendages comprising of both flagella and pili. The colony also radially expands, but does not do so constantly, favoring to engage in periods of high activity, followed by periods of slow motility [45, 46]. The result are concentric rings on a petri dish that give a "bullseye" pattern. *Pseudomonas aeruginosa*, while also having flagella and pili, do not form concentric rings. Rather, they migrate in long trails called *dendrites* that have a tendril like appearance [47].

1.4.1 The mesoscopic view of *S. marcescens*

S. marcescens presents itself with a slightly different colony morphology, although the pattern of a monolayer followed by a multilayer is still present. Patteson et al. conducted particle image velocimetry (PIV) measurements on swarms of *S. marcescens* to measure the flow speeds and streamlines of an active swarm due to the difficult of tracking fast-moving cells, especially within the dense multilayer [43]. The monolayer consists of a thin band of cells, with a width of only a few cells. Ahead of the monolayer and within free, unoccupied territory, is a surfactant layer (that can seen in phase contrast as a white band) that appears to jam cells between that surfactant layer and the dense, active multilayer behind it, and a dense, non-motile region deeper in to the center of the colony. The width of the active multilayer is approximately 200-300 μm. They report that region is comprised of active vortices that have a characteristic diameter of $\approx$ 20-25 μm and a characteristic lifetime of 0.1 s. By seeding tracer particles within the active swarm, they reveal that the vortices enable efficient cell and material transport which may contribute not just to better front propagation, but removal of dead cells, small objects, and increased antibiotic resistance [16, 48, 32].

1.5 Current approaches to modeling swarming bacteria

1.5.1 Active Brownian Particle Models

It is of interest to model swarming bacteria not only to understand the fundamental and underlying physics behind their collective motion and rapid surface movement, but swarming bacteria are also resembling of complex, active matter systems such as nematic liquid crystals [49, 50]. Computer models developed to study swarming bacteria are limited as they do not capture every possible variable observed in experiments but still offer insight in how specific features of swarmers such as aspect ratio, speeds, confinement, or fluid viscosity play a role in the dynamics of growing colonies. Various models have been published in order to better understand how these systems move, align, and propagate. A simple model that has been used are Active Brownian Particles (ABPs) with excluded volume, steric, and hydrodynamic interactions An ABP is modeled through the Langevin equations that include self-propulsion terms and effects from thermal noise to capture the motion of bacterial swimmers and crawling mammalian cells [51, 52, 53]. Periodic vortex arrays, have been simulated using a minimal model that includes only steric interactions between particles and neglects long-range hydrodynamics, highlighting the importance of steric cell-cell interactions in the formation of structures in collective motion [54]. The steric terms are short-range interactions, modeled as either short-range force dipoles or have terms that align or repel other particles as a function of particle-to-particle distance [55, 56, 57]. At low densities, particles are able to align in small clusters. At densities comparative to swarms, these dynamics break down and do not exhibit the same vortex dynamics seen in experiments. However, ABPs are inherently limited in studying active swarmers due to their morphology as rigid circles as opposed to being rod-like structures.

1.5.2 Self-propelled rod models

To address the morphological limitation, self-propelled rod (SPR) models are agent-based models that simulate cells as a series of connected points [58] or spherocylinders. In conjunction with similar parameters and terms in ABP models, the advantage of SPR models are their tunable lengths which can model the different lengths observed in bacteria swarms. By modeling swarmers as actual rods with defined aspect ratios, cell-cell collisions lead to the global alignment of cells in small system sizes [59]. At large system sizes (higher packing fractions), rods are not globally aligned. Rather, they form aligned microdomains like swarming rafts that move independently of other align rafts in the system. This observation appears to be abolished for SPR systems of higher aspect ratios at higher packing fractions (A $\geq$ 5, Φ = 0.65). Under these conditions, higher aspect ratios form rafts comprising of most of the rods in the system [60]. Wensick et al. looks at the turbulence generated by hydrodynamics in experiments, continuum, and agent based models, they find that in a minimal model, without hydrodynamics, SPR systems were able to model vortexing and turbulence similar to what was observed in *B. subtilis* [58].

The inclusion of hydrodynamics is of great interest as swarming is a surface movement on a thin layer of fluid. Stresses on the fluid generated by bacteria propulsion can affect the movement and collective ability of these systems, possibly disrupting the features seen in steric-only systems. In these studies, inclusion of hydrodynamics are commonly referred to as "wet" systems while the exclusion of hydrodynamics are referred to as "dry" systems. One possible way to model hydrodynamics in swarms are modeling rods as force dipole "pushers", whose flagella create fluid flow moving behind the cell/rod (flow direction from head to tail) [61, 62]. Lushi et al., looked at small systems of confined, active rods with hydrodynamics and were inspired by confined *B. subtilis* [63, 64]. In that study, the model predicted that hydrodynamic pushers move *against* the fluid flow, indicating that pusher cells generate thrust to overcome the flow and actively move against the flow in coordinated groups. A review by Bär et al. highlights these key findings and importance of both "dry" and "wet" SPR systems [49]. In summary, short-ranged interactions between rods promote greater alignment and clustering of agents [65], much like what is seen in swarming systems. Many of these studies are limited either by modeling cells as ABPs, excluding hydrodynamic interactions, or by not exploring dynamics between aligned clusters of cells.

1.6 Overview of Dissertation

In this chapter, I focused on swarming motility and how it differs from other movement modalities, and review the current literature on swarming bacteria species, emphasizing research conducted on swarming *Serratia marcescens*. I provided an overview of the critical factors necessary to induce swarming, the key features of swarming bacteria, and highlight gaps in studying swarming on a microscopic scale ($\mathcal{O}(1) - \mathcal{O}(10^2)$) and mesoscopic scale ($\mathcal{O}(10^4)$). I also review *in silico* continuum and agent-based modeling of bacteria swarmers, and how the modeling contributed to our current understanding of swarming.

In **chapter 2**, I provide a mesoscopic view of swarming *Serratia marcescens* as the colony traverses through a passive frictional region of immotile bacteria. Previous work from our group suggest that when a colony is exposed to a sufficient intensity of UV light for a sufficient amount of time, bacteria will remain permanently immotile (passive) without killing or lysing the cells. Typically, studies observe swarming colonies moving through *free-space*, or space where there are no physical obstructions present and the colony front is free to move into the unexplored territory. By passivating a sub-region of a swarming colony, this allows for study of a natural scenario where an active colony must displace immotile material in order to gain new ground. I describe the experiments in which we observe and analyze how an active swarm displaces these passive cells at their interface (referred to as the active-passive

interface). Our findings describe the collective motion of the active phase, and how the dynamic structural features and hydrodynamics of the swarm facilitate efficient material transport and displacement of passive cells. We also study the coupling between interface dynamics, roughness and emergent active interfacial flow. As in experiments, it is difficult to decouple the effects of short-range physical steric interactions and far-field hydrodynamics. Therefore, I use an agent-based model of self-propelled rods to simulate dilute and dense systems of swarming bacteria with tunable steric interactions, cell morphology, and hydrodynamic interactions in order to independently study the effects of either steric interactions between cells or hydrodynamic flows.

In **chapter 3**, I contrast the previous simulations on dense bacteria systems by simulating dilute systems of swarming *S. marcescens*. Current literature explores either larger systems of swarmers where direct cluster interactions cannot be easily observed, or systems comprised of only few cells to study key morphological features of swarmers. I explore densities in between the two, where clusters can be readily observed and discriminated in order to study their spatiotemporal dynamics. As described previously and in **chapter 2**, experiments cannot decouple the multiple factors that influence cell dynamics and collective motion. Therefore, I also utilize the SPR model to study dilute systems and how the formation and persistence of clusters is affected by cell morphology, short range cell-cell interactions, and long-range hydrodynamic interactions. Cell elongation is found to play a critical role in the size and persistence of clusters. Simulations with long cells that mimic the elongated lengths of swarming cells increase both the size and persistence whereas short cells comparable to planktonic or swimming cells suffer in their ability to collectively move. The inclusion of hydrodynamics (often referred to as "wet" systems) decreases the size and persistence of clusters compared to systems without hydrodynamics (referred to as "dry" systems). However, hydrodynamics actively mix cells in these systems, which provides a net benefit to the motility of cells and transport of material. These results ultimately suggest that elongation in bacteria swarming species is a key factor in their ability to form clusters and collectively move, and for dense systems, form vortex structures that enable rapid propagation across a surface.

In **chapter 4**, I present a method/workflow to study the pre-swarming phase (often referred to and will be referred to in this text as the lag time or lag period) of swarming bacteria species. The lag period is a period of time, often several hours, after inoculation where the colony grows and develops, but does not swarm. After which, the colony appears to swarm and spread. Very few papers up until to this point has attempted to observe cells during this lag period, where it has been hypothesized that growing cells gather resources by extracting fluid from the substrate in order to begin swarming. Additionally, I present a validation of particle tracking methods that can utilized to study the mechanical properties of swarming colonies.

Bibliography

[1] L. Alberti and R. M. Harshey, "Differentiation of Serratia marcescens 274 into swimmer and swarmer cells.," *Journal of Bacteriology*, vol. 172, no. 8, pp. 4322–4328, 1990.

[2] G. Lowe, M. Meister, and H. C. Berg, "Rapid rotation of flagellar bundles in swimming bacteria," *Nature*, vol. 325, no. 6105, p. 637–640, 1987.

[3] H. C. Berg, "The rotary motor of bacterial flagella," *Annual Review of Biochemistry*, vol. 72, no. 1, p. 19–54, 2003.

[4] S. Chattopadhyay, R. Moldovan, C. Yeung, and X. L. Wu, "Swimming efficiency of bacterium escherichia coli," *Proceedings of the National Academy of Sciences*, vol. 103, p. 13712–13717, 2006.

[5] H. C. BERG and D. A. BROWN, "Chemotaxis in escherichia coli analysed by three-dimensional tracking," *Nature*, vol. 239, no. 5374, p. 500–504, 1972.

[6] H. Berg, *Random Walks in Biology*. Princeton paperbacks, Princeton University Press, 1993.

[7] A. E. Patteson, A. Gopinath, M. Goulian, and P. E. Arratia, "Running and tumbling with E. coli in polymeric solutions," *Scientific Reports*, vol. 5, no. 1, p. 15761, 2015.

[8] H. C. Berg, *E. coli in Motion*. Springer, 2004.

[9] Y. Wu, B. G. Hosu, and H. C. Berg, "Microbubbles reveal chiral fluid flows in bacterial swarms," *Proceedings of the National Academy of Sciences*, vol. 108, no. 10, pp. 4147–4151, 2011.

[10] R. M. Harshey, "Bacterial motility on a surface: Many ways to a common goal," *Annual Review of Microbiology*, vol. 57, no. 1, p. 249–273, 2003.

[11] M. F. Copeland and D. B. Weibel, "Bacterial swarming: a model system for studying dynamic self-assembly," *Soft Matter*, vol. 5, no. 6, pp. 1174–1187, 2009.

[12] L. Hamouche, S. Laalami, A. Daerr, S. Song, I. B. Holland, S. J. Séror, K. Hamze, and H. Putzer, "Bacillus subtilis Swarmer Cells Lead the Swarm, Multiply, and Generate a Trail of Quiescent Descendants," *mBio*, vol. 8, no. 1, pp. e02102–16, 2017.

[13] N. C. Darnton, L. Turner, S. Rojevsky, and H. C. Berg, "Dynamics of bacterial swarming.," *Biophysical journal*, vol. 98, no. 10, pp. 2082–90, 2010.

[14] L. Turner, R. Zhang, N. C. Darnton, and H. C. Berg, "Visualization of flagella during bacterial swarming ," *Journal of Bacteriology*, vol. 192, no. 13, p. 3259–3267, 2010.

[15] D. B. Kearns, "A field guide to bacterial swarming motility," *Nature Reviews Microbiology*, vol. 8, no. 9, p. 634–644, 2010.

[16] R. M. Harshey and J. D. Partridge, "Shelter in a swarm," *Journal of Molecular Biology*, vol. 427, no. 23, p. 3683–3694, 2015.

[17] S. Ulitzur, "Induction of swarming in vibrio parahaemolyticus.," *Archives of microbiology*, vol. 101, no. 4, p. 357–63, 1974.

[18] J. Henrichsen, "Bacterial surface translocation: a survey and a classification.," *Bacteriological Reviews*, vol. 36, no. 4, p. 478–503, 1972.

[19] H. C. Berg, "Swarming motility: It better be wet," *Current Biology*, vol. 15, no. 15, p. R599–R600, 2005.

[20] L. Ping, Y. Wu, B. G. Hosu, J. X. Tang, and H. C. Berg, "Osmotic pressure in a bacterial swarm," *Biophysical Journal*, vol. 107, no. 4, p. 871–878, 2014.

[21] A. Yang, W. S. Tang, T. Si, and J. X. Tang, "Influence of Physical Effects on the Swarming Motility of Pseudomonas aeruginosa," *Biophysical Journal*, vol. 112, no. 7, pp. 1462–1471, 2017. This paper is of interest because it tells us different factors of the substrate that affect swarming.

[22] W.-J. Ke, Y.-H. Hsueh, Y.-C. Cheng, C.-C. Wu, and S.-T. Liu, "Water surface tension modulates the swarming mechanics of bacillus subtilis," *Frontiers in Microbiology*, vol. 6, p. 1017, 2015.

[23] T. Matsuyama, A. Bhasin, and R. M. Harshey, "Mutational analysis of flagellum-independent surface spreading of serratia marcescens 274 on a low-agar medium.," *Journal of Bacteriology*, vol. 177, no. 4, p. 987–991, 1995.

[24] T. Matsuyama, T. Tanikawa, and Y. Nakagawa, "Biosurfactants, from genes to applications," *Microbiology Monographs*, p. 93–120, 2010.

[25] R. Zhang, L. Turner, and H. C. Berg, "The upper surface of an escherichia coli swarm is stationary," *Proceedings of the National Academy of Sciences*, vol. 107, no. 1, p. 288–290, 2010.

[26] J. D. Partridge, G. Ariel, O. Schvartz, R. M. Harshey, and A. Be'er, "The 3D architecture of a bacterial swarm has implications for antibiotic tolerance," *Scientific Reports*, vol. 8, no. 1, p. 15823, 2018.

[27] J. D. Partridge, N. T. Q. Nhu, Y. S. Dufour, and R. M. Harshey, "Tumble Suppression Is a Conserved Feature of Swarming Motility," *mBio*, vol. 11, no. 3, 2020.

[28] M. Pezzlo, P. J. Valter, and M. J. Burns, "Wound infection associated with vibrio alginolyticus," *American Journal of Clinical Pathology*, vol. 71, no. 4, p. 476–478, 1979.

[29] J. Overhage, M. Bains, M. D. Brazas, and R. E. W. Hancock, "Swarming of pseudomonas aeruginosa is a complex adaptation leading to increased production of virulence factors and antibiotic resistance †," *Journal of Bacteriology*, vol. 190, no. 8, p. 2671–2679, 2008.

[30] J.-L. Bru, B. Rawson, C. Trinh, K. Whiteson, N. M. Høyland-Kroghsbo, and A. Siryaporn, "Pqs produced by the pseudomonas aeruginosa stress response repels swarms away from bacteriophage and antibiotics," *Journal of Bacteriology*, vol. 201, no. 23, 2019. Relevant because we can observe from this study that antibiotics repel swarms of bacteria. Very little studies of swarm dynamics and characterization of flows have been done response to antibiotics.

[31] M. T. Butler, Q. Wang, and R. M. Harshey, "Cell density and mobility protect swarming bacteria against antibiotics," *Proceedings of the National Academy of Sciences*, vol. 107, no. 8, pp. 3776–3781, 2010.

[32] S. Bhattacharyya, D. M. Walker, and R. M. Harshey, "Dead cells release a 'necrosignal' that activates antibiotic survival pathways in bacterial swarms," *Nature Communications*, vol. 11, no. 1, p. 4157, 2020.

[33] D. B. Kearns and R. Losick, "Swarming motility in undomesticated bacillus subtilis," *Molecular Microbiology*, vol. 49, no. 3, p. 581–590, 2003.

[34] A. Be'er, B. Ilkanaiv, R. Gross, D. B. Kearns, S. Heidenreich, M. Bär, and G. Ariel, "A phase diagram for bacterial swarming," *Communications Physics*, vol. 3, no. 1, p. 66, 2020.

[35] R. Hertle and H. Schwarz, "Serratia marcescens internalization and replication in human bladder epithelial cells," *BMC Infectious Diseases*, vol. 4, no. 1, p. 16, 2004.

[36] B. Ilkanaiv, D. B. Kearns, G. Ariel, and A. Be'er, "Effect of Cell Aspect Ratio on Swarming Bacteria," *Physical Review Letters*, vol. 118, no. 15, p. 158002, 2017.

[37] S. Peled, S. D. Ryan, S. Heidenreich, M. Bär, G. Ariel, and A. Be'er, "Heterogeneous bacterial swarms with mixed lengths," *Physical Review E*, vol. 103, no. 3, p. 032413, 2021.

[38] J. O'Rear, L. Alberti, and R. M. Harshey, "Mutations that impair swarming motility in serratia marcescens 274 include but are not limited to those affecting chemotaxis or flagellar function.," *Journal of Bacteriology*, vol. 174, no. 19, p. 6125–6137, 1992.

[39] F. F. V. Chevance and K. T. Hughes, "Coordinating assembly of a bacterial macromolecular machine," *Nature Reviews Microbiology*, vol. 6, no. 6, p. 455–465, 2008.

[40] K. M. Ford, J. D. Antani, A. Nagarajan, M. M. Johnson, and P. P. Lele, "Switching and torque generation in swarming e. coli," *Frontiers in Microbiology*, vol. 09, p. 2197, 2018.

[41] W. Chen, N. Mani, H. Karani, H. Li, S. Mani, and J. X. Tang, "Confinement discerns swarmers from planktonic bacteria," *eLife*, vol. 10, p. e64176, 2021.

[42] J. Yang, P. E. Arratia, A. E. Patteson, and A. Gopinath, "Quenching active swarms: effects of light exposure on collective motility in swarming Serratia marcescens," *Journal of The Royal Society Interface*, vol. 16, no. 156, p. 20180960, 2019.

[43] A. E. Patteson, A. Gopinath, and P. E. Arratia, "The propagation of active-passive interfaces in bacterial swarms," *Nature Communications*, vol. 9, no. 1, p. 5373, 2018.

[44] P. Chopra, D. Quint, A. Gopinathan, and B. Liu, "Geometric effects induce anomalous size-dependent active transport in structured environments," *Physical Review Fluids*, vol. 7, no. 7, p. L071101, 2022.

[45] J. F. M. Hoeniger, "Cellular changes accompanying the swarming of proteus mirabilis: I. observations of living cultures," *Canadian Journal of Microbiology*, vol. 10, no. 1, p. 1–9, 1964.

[46] J. F. M. Hoeniger, "Cellular changes accompanying the swarming of proteus mirabilis: Ii. observations of stained organisms," *Canadian Journal of Microbiology*, vol. 12, no. 1, p. 113–123, 1966.

[47] N. C. Caiazza, R. M. Q. Shanks, and G. A. O'Toole, "Rhamnolipids modulate swarming motility patterns of pseudomonas aeruginosa," *Journal of Bacteriology*, vol. 187, no. 21, p. 7351–7361, 2005.

[48] S. Benisty, E. Ben-Jacob, G. Ariel, and A. Be'er, "Antibiotic-Induced Anomalous Statistics of Collective Bacterial Swarming," *Physical Review Letters*, vol. 114, no. 1, p. 018105, 2015.

[49] M. Bär, R. Großmann, S. Heidenreich, and F. Peruani, "Self-Propelled Rods: Insights and Perspectives for Active Matter," *Annual Review of Condensed Matter Physics*, vol. 11, no. 1, pp. 1–26, 2019.

[50] G. Gompper, R. G. Winkler, T. Speck, A. Solon, C. Nardini, F. Peruani, H. Lwen, R. Golestanian, U. B. Kaupp, L. Alvarez, T. Kirboe, E. Lauga, W. C. K. Poon, A. DeSimone, S. Muios-Landin, A. Fischer, N. A. Sker, F. Cichos, R. Kapral, P. Gaspard, M. Ripoll, F. Sagues, A. Doostmohammadi, J. M. Yeomans, I. S. Aranson, C. Bechinger, H. Stark, C. K. Hemelrijk, F. J. Nedelec, T. Sarkar, T. Aryaksama, M. Lacroix, G. Duclos, V. Yashunsky, P. Silberzan, M. Arroyo, and S. Kale, "The 2020 motile active matter roadmap," *Journal of Physics: Condensed Matter*, vol. 32, no. 19, p. 193001, 2020.

[51] G. Volpe, S. Gigan, and G. Volpe, "Simulation of the active Brownian motion of a microswimmer," *American Journal of Physics*, vol. 82, no. 7, pp. 659–664, 2014.

[52] S. Bose, K. Dasbiswas, and A. Gopinath, "Matrix stiffness modulates mechanical interactions and promotes contact between motile cells," *Biomedicines*, vol. 9, no. 4, p. 428, 2021.

[53] S. Bose, P. S. Noerr, A. Gopinathan, A. Gopinath, and K. Dasbiswas, "Collective states of active particles with elastic dipolar interactions," *Frontiers in Physics*, vol. 10, p. 876126, 2022.

[54] R. Großmann, P. Romanczuk, M. Bär, and L. Schimansky-Geier, "Vortex Arrays and Mesoscale Turbulence of Self-Propelled Particles," *Physical Review Letters*, vol. 113, no. 25, p. 258104, 2014.

[55] N. Kumar, H. Soni, S. Ramaswamy, and A. K. Sood, "Flocking at a distance in active granular matter," *Nature Communications*, vol. 5, no. 1, p. 4688, 2014.

[56] S. Das and R. Chelakkot, "Morphological transitions of active Brownian particle aggregates on porous walls," *Soft Matter*, vol. 16, no. 31, pp. 7250–7255, 2020.

[57] L. Caprini and U. M. B. Marconi, "Spatial velocity correlations in inertial systems of active Brownian particles," *Soft Matter*, vol. 17, no. 15, pp. 4109–4121, 2021.

[58] H. H. Wensink, J. Dunkel, S. Heidenreich, K. Drescher, R. E. Goldstein, H. Löwen, and J. M. Yeomans, "Meso-scale turbulence in living fluids," *Proceedings of the National Academy of Sciences*, vol. 109, no. 36, pp. 14308–14313, 2012.

[59] S. Weitz, A. Deutsch, and F. Peruani, "Self-propelled rods exhibit a phase-separated state characterized by the presence of active stresses and the ejection of polar clusters," *Physical Review E*, vol. 92, no. 1, p. 012322, 2015.

[60] P. Bera, A. Wasim, J. Mondal, and P. Ghosh, "Mechanistic underpinning of cell aspect ratio-dependent emergent collective motions in swarming bacteria," *Soft Matter*, vol. 17, no. 31, pp. 7322–7331, 2021.

[61] K. Drescher, R. E. Goldstein, N. Michel, M. Polin, and I. Tuval, "Direct measurement of the flow field around swimming microorganisms," *Phys. Rev. Lett.*, vol. 105, p. 168101, Oct 2010.

[62] A. Baskaran and M. C. Marchetti, "Statistical mechanics and hydrodynamics of bacterial suspensions," *Proceedings of the National Academy of Sciences*, vol. 106, no. 37, p. 15567–15572, 2009.

[63] A. Baskaran and M. C. Marchetti, "Enhanced diffusion and ordering of self-propelled rods," *Physical Review Letters*, vol. 101, no. 26, p. 268101, 2008.

[64] E. Lushi, H. Wioland, and R. E. Goldstein, "Fluid flows created by swimming bacteria drive self-organization in confined suspensions," *Proceedings of the National Academy of Sciences*, vol. 111, no. 27, pp. 9733–9738, 2014.

[65] F. Peruani, A. Deutsch, and M. Bär, "Nonequilibrium clustering of self-propelled rods," *Physical Review E*, vol. 74, no. 3, p. 030904, 2006.

Chapter 2

Dynamics of active swarm interfaces propagating through passive frictional domains

2.1 Introduction

The experimental protocols to prepare the swarms of *Serratia marcescens*, the method of creating immotile (passive) domains within actively swarming regions and some of the experimental analysis presented in this chapter have been published previously in [1, 2].

An important feature of bacterial swarms are the dynamically evolving interfaces and propagating fronts that form naturally. A prototypical example of these fronts are spatiotemporally rich interfaces that separate motile active domains from passive domains comprised of dead or non-motile bacteria. Non-motile bacteria are inextensible, and they may still generate stresses in the fluid around them behaving as an effectively highly frictional material. In recent work from the lab [1, 2], the response of bacterial cells to wide-spectrum light to used to create internal active-passive interfaces within dense active swarms of *Serratia marcescens*. The overall effect of light – in terms of immobilizing bacterial cells – was found to depend on exposure time, and intensity, and wavelength. For fixed wavelengths, especially in the UV region of the spectrum, high intensities coupled with long exposure times caused a permanent loss of motility [2]. When combined with suitable shadowing material or screens to direct the incident light, this provided a controllable method to generate macroscopic domains with arbitrary geometries as required. For instance, a straight interface could be created whereby the immobilized (passive) domain and swarming (active) domain interacted [1]. Experiments revealed that the interface region has a well-defined thickness, with a quantifiable surface energy and raises the possibility that the propagation speed of the diffuse interface couples to local swarm velocity and interface curvature [1, 3].

In this chapter, we examine and investigate an equally important aspect of the active-passive interface, namely its spatiotemporal structure that enables the manner of propagation and colonization. The passive region comprises of densely packed aligned bacteria arranged in static domains that are typically smaller than the structure of the collective flow structures. Over length scales associated with multiple domains, the passive region appears as a dense frictional half-space which swarming bacteria have to penetrate in order to propagate. The interface is not sharp - rather it posses attributes of a classical diffuse interface with a well defined interfacial thickness. Employing PIV techniques and intensity based image analysis, we find that the diffuse, moving interface region is also characterized by a well-defined roughness profile. Correlations between spatially and temporally separated surface undulations are controlled by the interaction of the interface region with the intense adjacently located active flows. Dynamical and growth exponents characterizing the spatiotemporal roughness profile differ from the classical scaling values derived for passive growth or erosion. Our experiments also suggest possible self-similar behavior for the experimentally measured interfacial roughness opening up additional questions for future exploration.

In section 2.2, I describe recent work from the group and by collaborators [1, 2] on the observed behavior of swarming *Serratia marcescens* to UV-light and how, at sufficient time and durations, UV-light can render bacteria permanently passivized without killing them. This experimental setup allows observation of actively swarming cells moving through passive, highly frictional domains similar to situations where bacteria colonies must navigate through tortuous, frictional environments. These studies highlight how motile swarms feature long-range collective motions [4, 5, 6, 7, 8, 9, 10, 11, 12, 1, 2] featuring structures with defined length scales and persistence times. I analyze these experiments later in this section, focusing on the active-passive interface and how the spatiotemporal dynamics of the interface, active region, and passive region change. Additionally, the interface between the active-passive interface was tracked and the roughness measured spatiotemporally. The roughness of the interface correlates with the mean bacteria length (5 - 10 μm in length) and scaling of the roughness is found to deviate from the traditional Edward-Wilkinson (EW) and the Kardar-Parisi-Zhang (KPZ) scaling laws that attempt to describe the self-similar nature of interfaces.

Besides being relevant in biology and medicine, swarming bacteria are a convenient

experimental system to study and test models for dense active matter and active fluids [13, 14, 12, 15, 16, 17]. Recent numerical and theoretical studies have focused on the collective flows and identified dynamical exponents characterizing the energy spectrum and spatiotemporal features as well as variations near interfaces [13, 1]. To explain these features, theoretical models for swarming systems based on adaptations of classical nematic hydrodynamic theories and hydrodynamic multiphase models have been used to characterize the phase-separating active nematic and passive phases and propagation of interfaces of active nematics on substrates [18, 19, 20, 21]. Understanding the role of swarming in enabling bacterial collective motility and rapid propagation is both important and timely; this will require combination of experimental, analytical and computational approaches.

Informed by these experiments and other numerical and theoretical studies, section 2.3 describes the self-propelled rod (SPR) model I use to simulate individual swarming bacteria cells. A key feature that many previous models simulating high-density swarms lack is the inclusion of hydrodynamics that affect cell movement and collective features observed in swarms. – in other words, they simulate "dry" active systems rather than wet, fluid infiltrated systems. Our experiments on *Serratia marcescens*, and those of others, do not allow us to discriminate and separate the impact of purely steric effects from fluid mediated hydrodynamic interactions on the collective motion well within the active phase as well as in the vicinity of the interface. In other words, it is difficult to elucidate the effect of steric interactions and hydrodynamic interactions in the experiments described in section 2.2. To investigate each effect separately and also their combined effect, we analyze a discrete agent based simulations that treat the bacteria as inertialess self-propelled rods moving in a viscous fluid in two dimensions with parameters chosen to mimic the bacterial system. The simulation allows us the ability to combine and study the effects of important parameters separately or in combination, with each parameter encapsulating a desired physical mechanism.

In consideration of both steric and hydrodynamic interactions in bacterial swarms, our experiments and additional simulations, using codes built on original ones developed by Dr. Ardekani's group at Purdue suggest that hydrodynamic and steric interactions enable different modes of surface dynamics, morphology and front invasion. I begin by describing experiments on active-passive swarm systems and interfaces presented and discussed in earlier work [1, 2]. Then I summarize the analysis of images and data derived from these works (with permission). Data analysis and interpretation are then presented next. Following this, in 2.4, I report first details of the simulation scheme used to interpret these experiments, present results for dense active-passive systems as in the experiments, and conclude with a comparison between simulation predictions and experimental results. Specifically, I compare in this section two systems: one with hydrodynamics enabled and another with hydrodynamics disabled and assess that hydrodynamics introduce active mixing into the system that reduces the size and lifetime of structural features present in bacteria swarms, while promoting more efficient cellular and material transport that benefit the ability of a swarming colony to spread.

2.2   Experiments on swarming *S. marcescens* moving through passive-frictional domains

I use swarming *Serratia marcescens* as the model system to study two aspects of the swarming process as an active swarm propagates into a non-motile dense bacterial medium. The first aspect relates to the spatiotemporal structure of the interface and changes in morphology as it propagates. The second aspect is the relationship and competing roles of direct (steric) cell-cell interactions, and fluid mediated interactions on emergent active flow structures such as streamers, flocks and vortices.

Cultures of *Serratia marcescens* (WT ATCC 274) were grown from frozen glycerol stock in LB media consisting of 1 wt% Bacto Tryptone, 0.5 wt% yeast extract, and 0.5 wt%

NaCl in deionized water. The culture was incubated overnight at 34 °C until mid-exponential phase of growth ($0.4 \leq$ OD600 ≤ 0.8). Solid agar media was created by adding 0.6 wt% Bacto Agar and to LB media. The solution was autoclaved and cooled to room temperature to solidify and aliquoted into 50 mL Falcon tubes for later use. To prepare plates for experiments, 22.5 mL of agar was reheated in a hot water bath until molten, poured into a 100x15 mm petri dish and resuspended with 425 μL of 25% glucose solution. The plates were then left to cool until solidified. Cultures were diluted to an OD600 $= 0.6$. The solid agar plates were then inoculated with 5 mL of diluted culture.

2.2.1 Analysis of experiments

Features of the swarming base state prior to exposure

As a point of departure we summarize observations of our base state - the unexposed actively swarming region. In collectively-moving swarms, individual self-propelling cells are influenced by steric and hydrodynamic interactions with their neighbors [24, 7, 4, 1, 8]. These interactions result in complex structural and flow features including fluctuating regions of high vorticity and streamers as seen in Figure 2.1(a-b) (see also [1, 2]) that superimposes PIV derived velocity fields on a static image of the active swarm. The intensity and transient of these emergent flows increases as one moves from the leading front of the swarm as indicated by the faint white curve in Figure 2.1(a).

The probability distribution function $p(v)$ of averaged speeds (based on the PIV measurements) v in a region of area 400 μm^2 and at a distance 100 μm from the edge of the expanding colony shows a peak at 18 μm/s, an expectation value ≈ 28 μm/s and a tail that extends to 100 μm/s. The advancing front of the swarm is approximately 3 μm/s [1]. The spatial correlation function $C_v(\Delta r)$ and the temporal correlation $C_t(\Delta t)$ of the velocity fields were also calculated using

$$C_r(\Delta r) = \left\langle \frac{\mathbf{v}(r_0) \cdot \mathbf{v}(r_0 + \Delta r)}{|\mathbf{v}(r_0)|^2} \right\rangle, \tag{2.1}$$

and

$$C_t(\Delta t) = \left\langle \frac{\mathbf{v}(t_0) \cdot \mathbf{v}(t_0 + \Delta t)}{|\mathbf{v}(t_0)|^2} \right\rangle \tag{2.2}$$

respectively, with brackets denoting averages over reference positions r_0 and times t_0. Application of equation (2.1) yielded typical vortex sizes $\lambda_c \approx 20$ μm. For $\Delta r < \lambda_c$, bacterial velocities are correlated positively, $C_r > 0$. As Δr increases, the function C_r decays crossing zero and then stays negative for 21 μm $< \Delta r <$ 32 μm indicating neighboring vortices are typically anti-correlated. For $\Delta r > 32$ μm, velocity fields become progressively uncorrelated. Fitting $C_t(\Delta t) = \exp(-\Delta t/\tau)$, we estimate $\tau \approx 0.25$ s.

In Figure 2.1(b), we show a snapshot of the PIV derived vorticity field in the interior of the swarm region away from any interfaces. Note the organized, arrayed groups of clockwise and counter-clockwise vortices. The intensity and temporary nature of these vortices is clearly evidenced upon seeding the swarm with small 2 μm colloidal polystyrene spheres; these particles are strongly advected by the bacteria and follow tortuous trajectories (insets, Figure 2.1(b)). The particle trajectories obtained from standard particle tracking techniques are shown for 4 second time intervals. The particle speed distribution $p(v)$ was determined by pooling the particle speed over time for hundreds of particles; the particle speed is defined as the two-dimensional particle displacement over a 1 second time interval. The particle speed distribution measurement (blue circles) was found to follow a 2D Maxwell-Boltzmann distribution [1, 2], $p(v) = vm(k_B T_{\text{eff}})^{-1}\exp(-mv^2/2k_B T_{\text{eff}})$, where m is the mass of the polystyrene particle, k_B is the Boltzmann constant, and $T_{\text{eff}} \approx 2.2 \times 10^5$ K, approximately 700 times the thermal temperature (293 K). The mixing produced by these fluctuating flows
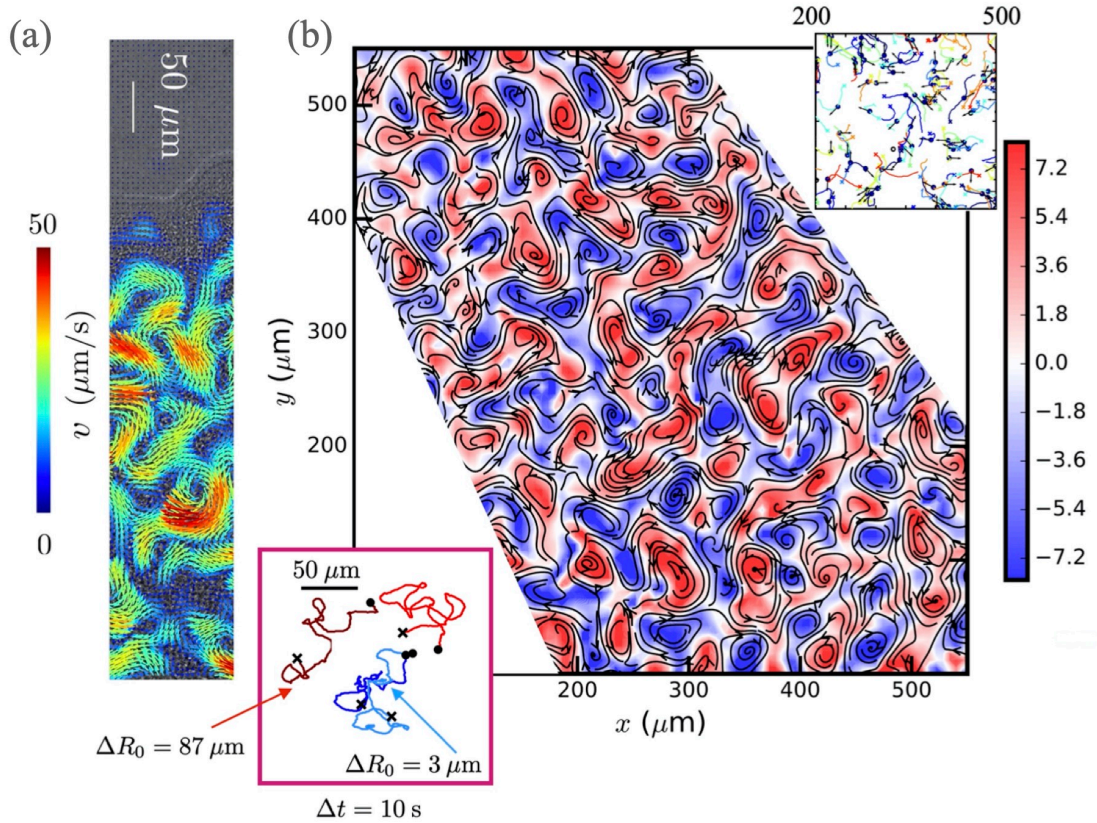
Figure 2.1: (a) (left) A section of a swarm front with velocity fields obtained using PIV and superimposed onto the image [22, 23]. The direction of propagation is upward. The free edge of the swarm is seen on the top as the white curve. Estimated speeds of the swarm increases rapidly as one moves from the interface and into the swarm (downward). The substrate is agar. We note that swarm speeds can reach values of 50 μm/s. (right) Snapshot of the vorticity field in the active phase that illustrates the alternate arrangement of well defined vortical structures. (b) (Inset, Top right) The vortical and time-dependent nature of the collective flows are easily observed by seeding the swarm film with 2μm particles (top, scale bar 50 μm) and then tracking their absolute as well as relative motions over time (Inset, Bottom left). (Center) We note persistent motion for small times leading to complex diffusion-like response. Tracers that are close to each other may move apart rather rapidly. The length scales of the vortical structures are $\sim 20 - 25$ μm; the residence time of structures is around 0.8 seconds [1]. Also note the presence of vortices of both signs as indicated by the organized arrangement of blue and red colored areas. Note the vortex lengths comprise of a few bacterial lengths. Experimental images and PIV analysis were reproduced from raw and processed data from experiments described in earlier work [1, 2]. The insets show characteristic trajectories of tracers particles indicating changes in the distance between particle sets with time.

is illustrated in the inset below (bottom left inset, Figure 2.1(b)) where we plot trajectories of spatially separated tracers (initial separations 3 μm and 87 μm) tracers.

Collective flows drive the propagating front

Figures 2.3(a) (i)-(ii) illustrate the interface region of the swarm (shown magnified in (i)) and also during light exposure (Figure 2.3 (c) - (ii)). The top half of the image (bright) is the domain that is exposed to light incident through a half-plane aperture. The dark (bottom) half is the unexposed active swarm. Note that the (apparent) boundary between the two phases
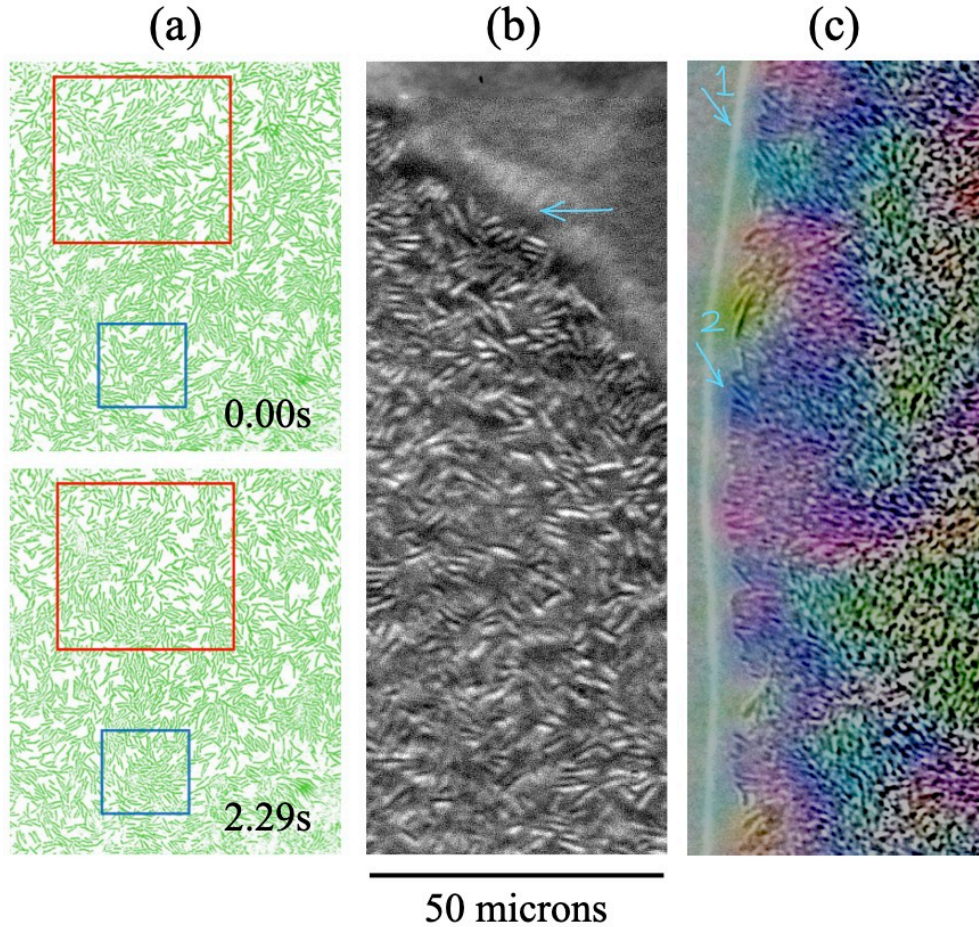
Figure 2.2: (a) Snapshots at two different times in the low-density and/or pre-swarming states indicating mechanisms by which bacterial clusters navigate jammed, stuck or otherwise immotile bacteria. Images are thresholded and color contrasted snapshots from raw videos. (b,c) Structural analysis using ImageJ and the OrientationJ plugin (c) of a section of a swarm near an interface.

is straight on very large length scales but wavy and diffuse on shorter length scales.

Focusing on the interface region in Figure 2.3(c)-(iii), we observe the velocity fields obtained from PIV analysis superposed on the raw image. Swarming bacteria in the active segment of the figure exhibit strong collective motion *right up to* the boundary region (flow speeds $\sim 50\ \mu$m/s). Vortices align along the interface, and are arrayed normal to it. Dynamic vortices (typical lifetime, ~ 0.24 s, frequency 0.8 s, characteristic vortex size $\sim 20-25\ \mu$m) etch the interface into cusps and valleys and are observed to control the morphology and structure of the interface.

Theoretical and computational studies of dense suspensions of passive rods suggest that polar and/or nematic alignment may be induced due to a combination of excluded volume effects – modeled for instance using a mean-field Maier-Saupe or Onsager potential – and thermal diffusion [25, 26]. Recognizing that bacterial swarms may behave similarly, we examined the structure and alignment of bacterial clusters in the active and passive phases as the interface position changed in time using the *Directional J* and *OrientationJ* plugins that are a part of the open source software [22] *ImageJ*. Qualitatively, the orientation is visualized as a false-color image with colored domains with domains of the same color indicating similarly aligned bacteria and intensity quantifying degree of coherence. Structural information
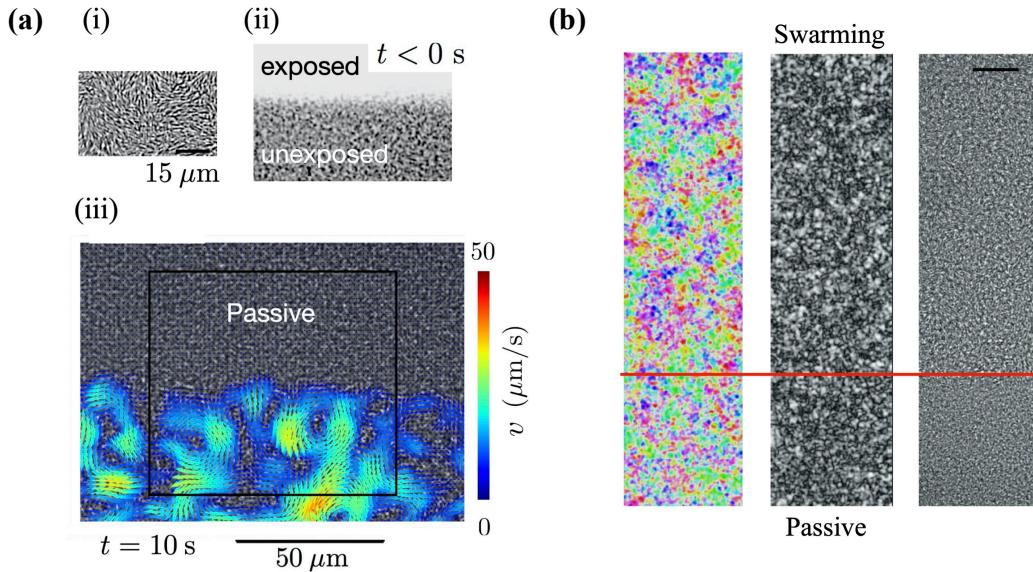
Figure 2.3: (a) (i) Raw image of the active (dark) - passive (light) edge generated by light exposure. (ii) Examination of the vicinity of the front separating the active and passive domains 10s after exposure ($t > 0$) reveals strong velocity gradients (in color) in the active region. Far from the interface, the active flows show intense vortical patterns. The snapshots are from videos taken with 63x (NA = 0.7) objective in a Nikon inverted microscope and includes a larger area of view. (b) Structural analysis using *ImageJ* and the *OrientationJ* plugin of a section of the active-passive interface. Snapshot from raw video acquired using 20x Nikon objective at 30 fps. We show (left) - length scales of similarly clusters, (middle, grayscale indicating degree of alignment) the degree of alignment and (right) an instantaneous snapshot. Images and analysis in **(a)** and raw images from **(b)** were used with permission, and correspond to analysis of previously published data (see [1, 2]).

such as size of coherently arrayed structures and length scales over which structural features are correlated may thus be obtained. Using these plugins, the domains are seen to span a distribution of sizes, with values typically between 10-20 μm accompanied by continuously changing orientational fields [2]. Figure 2.3(b) shows the result of such an image based analysis of the structural features demonstrating the presence of many intertwined aligned domains. This however, is just a static representation of the highly dynamical swarming process.

Intensity field quantify interface shape and roughness

The raw videos obtained from the images provide a sequence of snapshots of the intensity field over the domain of observation as a function of time. Noting that the mean intensity fluctuations in the active and passive phases far from the boundary, $|\Delta I_A(t)|$ and $|\Delta I_P(t)|$, remained relatively constant over the duration of the longest experiments, we defined a scalar order parameter, $\phi_{\mathrm{E}} \in [-1, 1]$ (the subscript E denotes experiments)

$$\phi_{\mathrm{E}} = \frac{2|\Delta I| - |\Delta I_A(t)| - |\Delta I_P(t)|}{|\Delta I_A(t)| - |\Delta I_P(t)|} \tag{2.3}$$

that was computed from intensity fluctuations ΔI between successive images to locate and track the inter-phase boundary. To reduce noise in the system (due to pixel resolution, short-range fluctuations and background light fluctuations), we then filtered the pixel-wise calculated order parameter by smoothing the data over a 3×3 μm^2 area. The filtered phase field has value
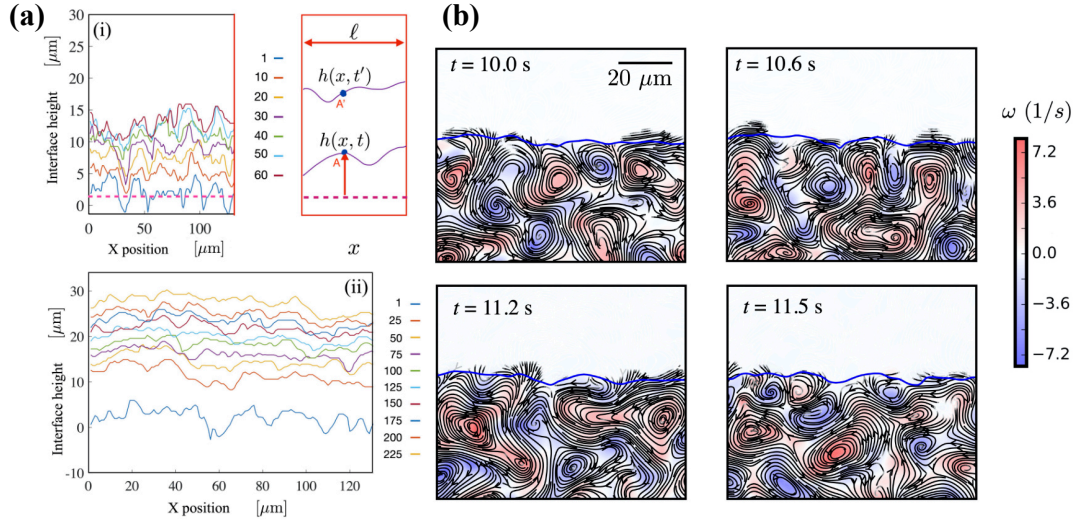
Figure 2.4: (a) Interface profiles in the (x, y) plane obtained from the phase-field based on intensity fluctuations for two experimental data sets - (i) & (ii). The shapes are obtained by fitting a vertically averaged (along y) one-dimensional phase field and seeking the location of $\phi_E = 0$ as a function of the lateral position, x. Time stamps are in seconds. For these profiles, the one-dimensional, averaged phase field (system size $L = 200$ μm) $\langle \phi_E \rangle_x \equiv \int_0^L (\phi_E/L) \, dx$ follows a quasi-static form. Also shown is a schematic demonstrating the definitions of the variables used to calculate the interface location and thence the interface height $h(x, t)$. (b) Snapshots focusing on a subdomain of the active-passive interface in Figure 2.1(b). The filtered two-dimensional interface position identified by the locus $\phi_E(\mathbf{r}_{Int}, t) = 0$ is shown as the blue curve for various times after cessation of exposure. PIV derived snapshots of the vorticity field and overlaid streamlines reveal the dynamic motion of individual vortices. Individual vortices - red (counter-clockwise) and blue (clockwise) - etch the interface boundary (blue line). Interface profiles in **(a)** were produced in this dissertation from raw datasets taken from [1, 2]. Streamline plots showing the vorticity field in **(b)** were generated by analyzing data corresponding to experiments in [1, 2] (with permission).
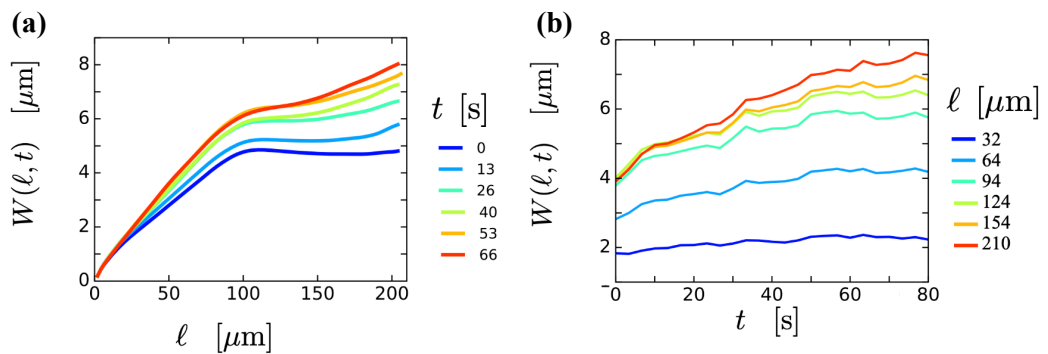
Figure 2.5: Interface roughness as a function of box length and time. The upper and lower roughness bounds, are measured from four experiments. (a) Local interface roughness profiles W as a function of box length ℓ measured over time t for a single experiment. (b) Sample interface roughness W values for various ℓ in a single experiment as a function of time, t. Roughness profiles were produced from raw data discussed in [1], that were then discretized and analyzed.

-1 corresponding to the completely passive phase and +1 corresponding to the fully active phase. The interface boundary was identified as the characteristic region over which ϕ_E changes from one asymptotic value to the other; sharp variation occurring over a finite length that is identified[1] as a characteristic interface width. To obtain a clear value for the mean interface position, we therefore defined the interface position (in the two dimensional $x - y$ plane) $\mathbf{r}_{\text{Int}}(t)$ implicitly by the locus of points such that $\phi_E(\mathbf{r}_{\text{Int}}, t) = 0$. Our system being approximately two-dimensional, we chose to orient the x axis along the edge of active-passive interface observed at the instant exposure is stopped $t = 0$. The interface shapes extracted from the phase field did not feature overhangs.

Snapshots of the interface location (here the two dimensional curve in the $x - y$ plane) for two representative experiments are shown in Figure 2.4(a) - (i) & (ii) along with a schematic sketch of the notation and definitions used. The profiles clearly exhibit significant roughness. Figure 2.4(b), illustrates the PIV derived snapshots of the vorticity field and overlaid streamlines for the experiment corresponding to Figure 2.3(c)-(iii) illustrating the rapid turnover of collective flow features before the interface has the time to propagate significantly.

Averaging over the lateral dimension normal to the direction of propagation, we obtain a one-dimensional, phase field profile $\langle \phi_E \rangle_x \equiv \int_0^L (\phi_E/L)\, dx$ that, after initial transients, is well represented by

$$\langle \phi_E \rangle_x = \int_0^L \frac{\phi_E}{L}\, dx \approx \tanh\left(\frac{y - Y(t)}{d(t)} \right). \tag{2.4}$$

Equation (2.4) provides the *mean averaged* interface location $Y(t)$ and the intrinsic thickness $d(t)$. Details of the procedure and the connection between the spatiotemporal variations in d and Y and the collective flow in the active phase have been analyzed[1, 2] in previous studies and will not be addressed here.

Roughness profiles

Interface roughness is related to the extrinsic thickness W (the width correlation function) [27, 28, 29, 30], that is defined as

$$W^2(\ell, t) = \left\langle \int_{x_0}^{x_0+\ell} \frac{1}{\ell} \left| h(x', t) - \overline{h(x', t)} \right|^2 dx' \right\rangle_{x_0} \tag{2.5}$$

where $\overline{h(x', t)}$ is the local average over distance ℓ, x_0 is the reference position and ℓ the averaging box length that in our series of experiments varies from around 2 μm up to the system size $L = 200$ μm.

Figure 2.5 shows sample interface roughness profiles $W(\ell, t)$: Focusing first on the ℓ dependence of W - shown in Figure 2.5(a) - we observe two regimes, the first corresponding to $\ell < 80$ μm and the second to $\ell > 80$ μm. For either regime, W increases with t (blue to red) with the curves eventually collapsing to a single curve (c.f the orange at 53 s and the red curve at 66 s). We find $\langle W \rangle_t \sim \ell$ for $\ell < 80$ μm. For $\ell > 80$ μm, the dependence is very weak (the exponent being smaller than 1/2). The data in Figure 2.5(a) suggests that for interfacial separations less than ≈ 80 μm, roughness is perhaps correlated (power law $> 1/2$). This result may be a consequence of the periodicity of the active vortical flows. However a clear understanding of the length scale is elusive.

We use our experimental data to analyze the interface roughness W values for various ℓ in a single flat interface experiment as a function of time, t. As seen in Figure 2.5(c), we observe an increasing power law in time with increasing ℓ; of course, eventually for large ℓ (up to $\ell = L$), we observe the curves approaching each other. Erosion is caused by the swirling vortical flows that form (arrayed periodically) adjacent to the interface. This spatial organization combined
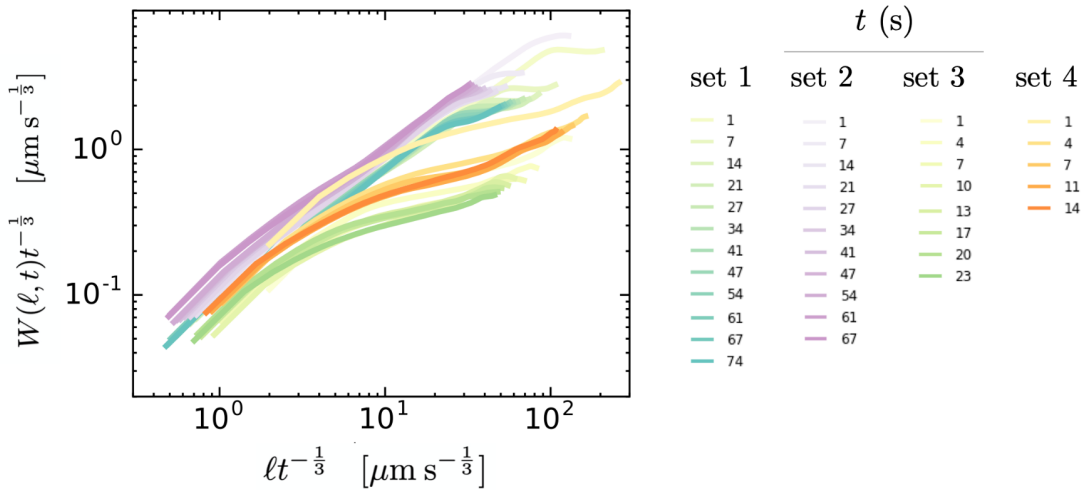
Figure 2.6: We estimate the roughness and dynamic exponents by measuring the extrinsic width $W(\ell, t)$ over time. The scaled interface roughness profiles collapse for four separate experimental realizations with each experiment collapsing into its own curve The growth exponent is $b = 1/3$ and the dynamic exponent is $z = 3$. Here, we show four experiments, denoted as set 1-4; each curve is plotted using a different time value in that experimental set.

with time dependence of the positions at which vortices are located, results in fluctuations in W observed in Figure 2.5(c).

Dynamic scaling approaches for the description of initially flat, self-affine, single-valued interfaces that roughen with time have been proposed based on continuum models of the growth/erosion process in a variety of geophysical and materials physics contexts[27, 28, 30, 31]. Self-similar roughness profiles in these theoretically studied cases follow scalings given by $W(L,t) \sim t^{\beta}$, $(t \ll t^{*})$, $W(L,t) \sim \ell^{\alpha}$, $(t \gg t^{*})$ and $t^{*} \sim \ell^{z}$ with $z = \alpha/\beta$. Here α, β and ℓ are the local roughness exponent, local growth exponent and system size respectively. The scaling relation here means that for early time $(t \ll t^{*})$, the roughness grows as a power law of time till it saturates for characteristic time t^{*}. After time t^{*}, the roughness grows as a power law of ℓ with z defined as the dynamic exponent,

$$W(L,t) \sim \ell^{\alpha} \mathcal{F}\left(t/\ell^{\alpha/\beta}\right) = \ell^{\alpha} \mathcal{F}\left(t/\ell^{z}\right) \tag{2.6}$$

A quantity complementary to characteristic time t^{*}, (if it exists) is the characteristic width L^{*}. An alternate manner to describe self-similarity is via the forms

$$W(\ell, t) \quad \sim \quad t^{\alpha/z} \mathcal{G}\left(\ell/\eta(t)\right) = t^{\alpha/z} \mathcal{G}\left(\ell/t^{1/z}\right), \tag{2.7}$$

$$\mathrm{G}(\zeta \ll 1) \quad \sim \quad \zeta^{\alpha}, \quad \mathrm{G}(\zeta \gg 1) \sim \ \mathrm{constant}. \tag{2.8}$$

The spatiotemporal evolution of a flat interface occurs as $W \sim t^{\beta}$ at short time; eventually correlations develop along the interface that saturate when the correlation length becomes the characteristic length. The set of exponents then decides the specific universality class describing the growth [27]. We note that equations (2.6)-(2.8) usually describe process without an imposed external length scale. The Edwards-Wilkinson (EW) class describes an interface that roughens due to random particle deposition and is smoothed by lateral motion, such as at the surface of settled granular aggregates under gravity. The Kardar-Parisi-Zhang (KPZ) class describes interfacial growth due to random particle depositions and explicitly includes a nonlinear term

for growth perpendicular to the interface. Both the KPZ and EW describe the interface through local growth mechanisms.

In order to test if the roughness profiles we obtained from experiments were self-similar, we attempted to plot these in a manner consistent with equations (2.6)-(2.8). Figure 2.6 summarizes these results. We see that scaled roughness profiles from 4 experiments show similar qualitative features. We see domains where the rescaled curves collapse suggesting a self-similar form.

2.3   Simulations of dense bacterial swarms

It is of interest to understand if steric effects and hydrodynamic effects play equal roles in the interface propagation and in determining the spatiotemporal features of the interface, specifically roughness features and swarming intensity. Furthermore, understanding the relative importance of hydrodynamic interactions will shed light on swarming in moist rather than wet environments. Here, bacteria swarm in a film sufficient to maintain their swarming phenotype. The thin film of liquid and the soft underlying substrate act as momentum sinks and confine the effects of hydrodynamic interactions to local and medium range length scales.

As mentioned previously, our experiments on *Serratia marcescens* do not allow us to discriminate and separate the impact of purely steric effects from fluid mediated hydrodynamic interactions on the collective motion well within the active phase as well as in the vicinity of the interface. To investigate each effect separately and when acting in tandem, we next propose and analyze discrete agent based simulations that treat the bacteria as inertialess self-propelled rods (SPR) [13] moving in a viscous fluid. Steric interactions are implemented as explained below using standard interaction potentials that depend on distances between the bacteria with rods interacting with all neighbors within a cut-off distance. Hydrodynamic interactions are implemented by treating each rod as a moving line of force dipoles. We do not include thermal noise in our system and ignore translational and rotational diffusion of the rods.

2.3.1   Agent based simulation model without thermal noise

The simulated bacterial swarm system consists of $N = 56,000$ rod-like bacteria. Each simulated bacteria is idealized as a slender rod of length $\ell_{\rm b}$ and width λ (the aspect ratio is thus $a = \ell_{\rm b}/\lambda = 5$) that can self-propel. These *in-silico* bacteria move in a domain of area $A = 500 \times 800$ (measured in bacterial width units); the ambient fluid is Newtonian with shear viscosity μ, and density ρ. The rods have an intrinsic self-propulsion speed u_o. We note that for *Serratia marcesens*, the self-propulsion speed $u_o \sim 28\mu$m/s swimming in a water-like Newtonian fluid, the Reynolds number $\mathcal{R} \equiv \ell_{\rm b}u_o\rho/\mu \ll 1$ and thus the use of the Stokes equation is appropriate. In accord with the experimental settings, we simulate a dense suspension with an area fraction $\psi = N\ell_{\rm b}\lambda/A = 0.7$. In simulations, lengths are scaled by rod width λ, velocities are scaled by intrinsic self-propulsion velocity u_o, time by $\tau = \lambda/u_o \sim 0.04$ s, and forces by $\mu u_o \lambda$. Experiments on bacteria in the dilute pre-swarming phase (Figure 2.2a) suggest that bacteria in colonies have a range of bacterial lengths with a mean between 5-7 μm; longer bacteria that are 2-3 times the length are possible.

Rods are indexed uniquely so as to be able to track them over time. The position and state of a rod with index α is completely determined once the position of its mass $\mathbf{r}^\alpha$, its orientation vector $\mathbf{p}^\alpha$, its linear velocity $d\mathbf{r}^\alpha/dt$, and its angular velocity ω^α are known. In the overdamped limit characterized by small Reynolds numbers, the evolution of these variables is

governed by

$$\frac{d\mathbf{r}^\alpha}{dt} \quad = \quad \mathbf{u}_h + V\mathbf{p}^\alpha + \mathbf{f}_T^{-1} \cdot \mathbf{F}_s, \tag{2.9}$$

$$\omega^\alpha \quad = \quad \omega_h + \mathbf{f}_R^{-1} \cdot \mathbf{T}_s. \tag{2.10}$$

Here, $\mathbf{u}_h$ and ω_h are the hydrodynamic contributions to the translational and rotational speed of the rod, respectively $V = 1$ is the dimensionless self-propulsion speed, $\mathbf{p}$ is the unit vector of rod orientation, $\mathbf{F}_s$ and $\mathbf{T}_s$ are the force and torque due to the steric effects between neighboring bacteria. The tensors $\mathbf{f}_T$ and $\mathbf{f}_R$ in (2.11) and (2.12) are the translational and rotational friction tensors given by

$$\frac{\mathbf{f}_T}{f_0} \quad = \quad f_\parallel \mathbf{p}^\alpha \mathbf{p}^\alpha + f_\perp(\mathbf{I} - \mathbf{p}^\alpha \mathbf{p}^\alpha), \tag{2.11}$$

$$\frac{\mathbf{f}_R}{f_0} \quad = \quad \lambda^2 f_R \mathbf{I}. \tag{2.12}$$

with $f_0 = 1$ being the Stokesian friction coefficient proportional to the fluid viscosity in scaled units. The three scalar friction coefficients $f_\parallel$, $f_\perp$ and f_R are dimensionless geometric factors that depend on the aspect ratio a of the rods. Here, we adopt the expression for cylinders and use

$$2\pi/f_\parallel \quad = \quad \ln(2a) - \gamma_\parallel, \tag{2.13}$$

$$4\pi/f_\perp \quad = \quad \ln(2a) - \gamma_\perp, \tag{2.14}$$

$$\pi a^2/3 f_R \quad = \quad \ln(2a) - \gamma_R \tag{2.15}$$

with $(\gamma_\parallel, \gamma_\perp, \gamma_R)$ given by Broersma [32].

2.3.2 Steric interactions

Steric interactions between rods (bacteria) are treated in a discrete manner. We partition each rod into $n = 6$ segments with each segment represented by a point. The position of these points may then be used to evaluate interactions. Geometry dictates that two rods α and β interact only if their center-of-mass distance $|\Delta\mathbf{r}^{\alpha\beta}| = |\mathbf{r}^\alpha - \mathbf{r}^\beta|$ is less than $\ell_b + 2\lambda$. Let $r_{ij}^{\alpha\beta}$ be the distance between the i-th segment of rod α and j-th segment of rod β calculated as

$$r_{ij}^{\alpha\beta} = |\Delta\mathbf{r}^{\alpha\beta} + (\ell_i\mathbf{p}^\alpha - \ell_j\mathbf{p}^\beta)| \tag{2.16}$$

where $\mathbf{p}^\alpha$ and $\mathbf{p}^\beta$ are the orientation vectors of rods with indices α and β and parameters $\ell_i, \ell_j \in [-\ell_b/2, \ell_b/2]$ locate positions of the segments along the rods. The total steric derived potential evaluated along rod α is then obtained using the Yukawa potential for the interaction [33, 13]:

$$U^\alpha = \frac{1}{2}\sum_{\beta\neq\alpha} \mathrm{H}(R_c - r^{\alpha\beta}) \; \frac{U_0}{n^2}\sum_{i=1}^{n}\sum_{j=1}^{n} \frac{\exp(-r_{ij}^{\alpha\beta}/\lambda)}{r_{ij}^{\alpha\beta}} \tag{2.17}$$

where $\mathrm{H}(x)$ is the Heaviside step function, $U_0 = 800$ is the dimensionless potential strength with scale of $\mu u_0 \lambda^2$, and R_c is the cutoff radius beyond which the steric interaction is zero. Here we choose $R_c = 1.25\lambda$. A linked-cells algorithm for short-range interaction [34] is used to accelerate the calculation of the steric interaction given the large number of rods in our simulated system.

2.3.3 Hydrodynamic interactions

The hydrodynamic terms $\mathbf{u}_h$ and ω_h are obtained by solving for the background flow experienced by rod α due to the dipolar flows generated by all the rods in the system. This

background flow is obtained by solving the appropriate Stokes equation in 2D - here, the two-dimensional incompressible Stokes equation for the fluid velocity field $\mathbf{u}$ supplemented with extra source terms corresponding to the distribution of dipolar stresslets aligned along each rod in the system. The resulting extra fluid induced drag forces are calculated using the distributed Lagrange multiplier method [35, 36] used earlier in suspensions of active swimmers.

The flow field induced in the fluid due to the distributed active stresslet is given by

$$
\nabla^2 \mathbf{u} = -\nabla p + \sum_{i=1}^{n} \mathbf{F}_i \sigma(\mathbf{x} - \mathbf{x}_i), \tag{2.18}
$$

$$
\nabla \cdot \mathbf{u} = 0, \tag{2.19}
$$

where p is the pressure, and $\mathbf{F}_i = (2\alpha_h/n)(\ell_i/|\ell_i|)V\mathbf{p}$ is the force distribution for each rod segment, where i is the index of rod segments, and α_h is the dimensionless stresslet strength of the bacteria. In our simulations, $\alpha_h = 1$ [10]. In (2.19), the term $\sigma(\mathbf{x} - \mathbf{x}_i)$ converts the forces on rods (Lagrangian grid) to the background flow field (Eulerian grid) with $\mathbf{x}$, $\mathbf{x}_i$ denoting the position of Cartesian grid points and rod segments, respectively. The resulting flow field $\mathbf{u}$ is then interpolated on the rod segments as $\mathbf{v}$, and then integrated along the rod length to obtain the total hydrodynamic contributions to the translational and rotational speed of the rod

$$
M_{\mathrm{b}}\mathbf{u}_h = \int_{\ell_{\mathrm{b}}} \rho\mathbf{v}d\ell, \quad \text{and} \quad \mathbf{I}_{\mathrm{b}} \cdot \omega_h = \int_{\ell_{\mathrm{b}}} \rho\mathbf{r} \times \mathbf{v}d\ell, \tag{2.20}
$$

where $\rho = 1$ is the density ratio between rods and the fluid, ℓ is the distance along the rod length, $\mathbf{r}$ is the position vector evaluated from the center of mass, and M_{b} and $\mathbf{I}_{\mathrm{b}}$ are the dimensionless mass and moment of inertia of the rod, respectively. Evaluation of $\mathbf{u}_h$ and ω_h closes the set of equations (2.9)-(2.15) for the system of rods. Positions and orientations can be tracked in time. Concomitantly, (2.18)-(2.20) provides spatiotemporal features of the fluid.

Using this computational model, I validated the model by testing a range of hydrodynamic values (Figures 2.7, 2.8) and different lengths (Figure 2.9) to validate the model's use for a variety of swarmer lengths.

2.4 Simulation results and analysis

2.4.1 Initialization of SPR systems

In the experiments, the quenched passive bacteria in the exposed region were observed to have significant local nematic alignment [2]. However on the whole when averaged over length scales much larger than 20 μm alignment was more or less random. This is consistent with the paralyzed retaining order at length scales comparable to the size of the collective structures in the active region. The swarming bacteria, when spatially and temporally averaged, are on average randomly oriented (ignoring the small bias due to the speed of the swarming front). Therefore, to maintain consistency across simulations, and to try to mimic this feature in our noise-less simulations, we conducted each simulation in two steps with the domain held fixed. To reduce the uncertainties, we averaged the roughness results based on ten simulation runs with each simulation starting from a different initial rod configuration.

The first step of the simulation allowed us to generate random orientational and spatial distribution of bacteria (rods) at high volume fractions. In order to achieve this, we set all rods to be motile and hydrodynamically interacting; the rods are located initially in a rectangular grid and are aligned. This is shown in Figure 2.7. A perturbation is then superimposed on the rod orientation $\mathbf{p}$. We let each rod move and evolve for a long enough time so that the position and orientation of the rods represent a possible configuration for the bacterial system before

the exposure to light. There are nematic structures in the initial state of the rods, and some regions are void of bacteria because of the swarming effects. It is likely that in the swarming bacteria experiments, noise and possible two-dimensional effects where bacteria can move in and out of the plane may reduce the propensity for such regions devoid of bacteria. The rod positions and orientations are then extracted and used as the initial configuration in the second step.

In the second step, only rods located in the lower half of the domain are set to be motile ($V = 1$, Equation (2.9)) while the rest are passive ($V = 0$, Equation (2.9)). We then advance time with each rod moving and interacting with other rods. As the simulation proceeds, we track the active-passive interface. Here, the simulation domain is a rectangle of a fixed height $H = 800$ with wall boundary conditions applied at the upper and lower boundaries. This height is large enough that the active-passive interface is not affected by the confinement of the walls initially over the time-scale of our simulations. Periodic boundary conditions are applied to the left and right boundaries of the simulation domain. A sample of this evolution is shown in a dilute system in Figure 2.7.
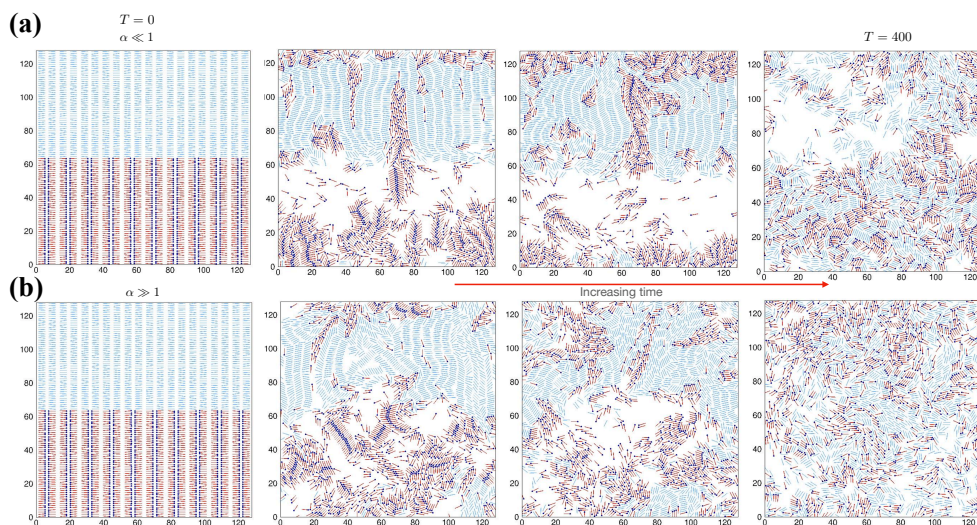
Figure 2.7: Initialization of a half-passive, half-active interface simulation. The top-half are passive rods with no self-propulsion (light blue rods) while the bottom-half are active rods (red with blue head indicating the "front" of a rod). **(a)** A system of N = 900 rods in the dry-limit where hydrodynamic contributions are negligible. **(b)** A system of N = 900 rods where hydrodynamic contributions compete with steric interactions. In **(a)**, negligible hydrodynamics in these systems generate voids as rods tend to cling together due to steric interactions. **(b)**, meanwhile, shows that hydrodynamic interactions actively mix the system such that minimal voids are present and actively moving rods are able to move further into the passive phase in the same amount of time.

2.4.2 Validation of the SPR model

Hydrodynamics in *in silico* models introduces additional terms that act as competing interactions with steric interactions between rods. To test these competing interactions, I created a dilute system ($\psi = 0.33$, L = 5, N = 900) at the dry-limit (α=0.1) and at a value where hydrodynamics are expected to dominate (α=10). With the inclusion of the Yukawa potential (Equation 2.17), rods within the cutoff range are attracted to one another and will tend to stick to one another as shown in Figure 2.8(a). While this does appear to benefit the clustering ability, swarms are characterized as fluidic flows that are able to convect material efficiently (Figure

2.1). Thus, the inclusion of hydrodynamics in models is crucial for modeling realistic swarmers. Figure 2.8(b) validates this point by showing a system dominated by hydrodynamic interactions. The result is a highly disperse system of rods where very little permanent and highly persistent clustering occurs. The corresponding pressure and vorticity plots show increased range and magnitude of the pressure and vorticity, thereby displaying the positive effect hydrodynamics have on the active mixing of the system and efficient particle transport.
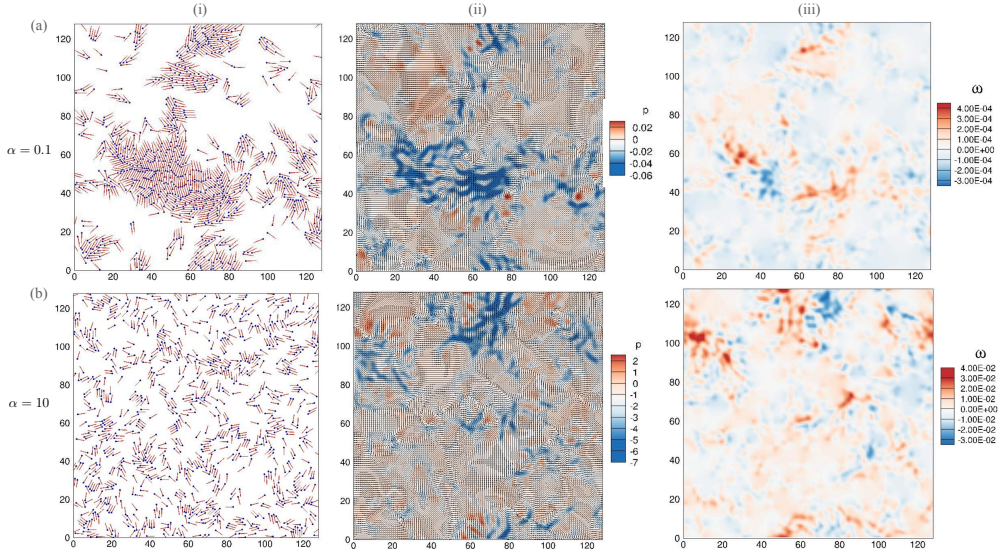
Figure 2.8: Simulations of a fully active system of L = 5 rods at the dry-limit (α=0.1) and where hydrodynamic interactions dominate (α=10). N = 900 in each system. For each system, (i) shows a snapshot of the system, (ii) shows the corresponding pressure fields, and (iii) shows the corresponding vorticity fields. In **(a)**, where the system is in the dry-limit, the rods are held together primarily by steric interactions and form large clusters. Whereas in **(b)**, the hydrodynamic flows introduce heavy active mixing that disperse clusters. These are emphasized in the corresponding pressure and vorticity fields, where in **(a, ii-iii)** the magnitude of the pressure and vorticity are significantly smaller than in systems where hydrodynamics dominate **(a, ii-iii)**.

To further probe the capabilities of the system and assert that the SPR model can indeed be used to test a range of swarming lengths, I increase the length of rods from L = 5 to L = 10 and initialize them in dilute (ψ=0.3, N = 500, α=1) and dense systems (ψ = 0.80 N = 1200, α=1). Figure 2.9 displays both of these systems and show promise of further studies expanding on the role of aspect ratio. These systems of elongated rods show that compared to L = 5, the range and magnitude of the vorticity and pressure are increased, as well as the apparent size of vorticity fields. While this chapter does not further explore the role of rod length, **chapter 3** further explores the role of rod length.

2.4.3 Defining the effective interface position

To calculate the number density and velocity fields of bacteria, we divided the simulation domain into small bins of size $\delta = 4$ and computed the numbers of both active and passive rods in each bin. We smoothed the velocity and vorticity fields by analyzing the data in overlapping cells [13], with cell size 1.5 times bin size.

In our experiments, individual bacteria could not always be clearly visualized especially in the passive region - however their motion was clearly observable. Therefore, we used intensity fluctuations (that are correlated with density fluctuations) to estimate the
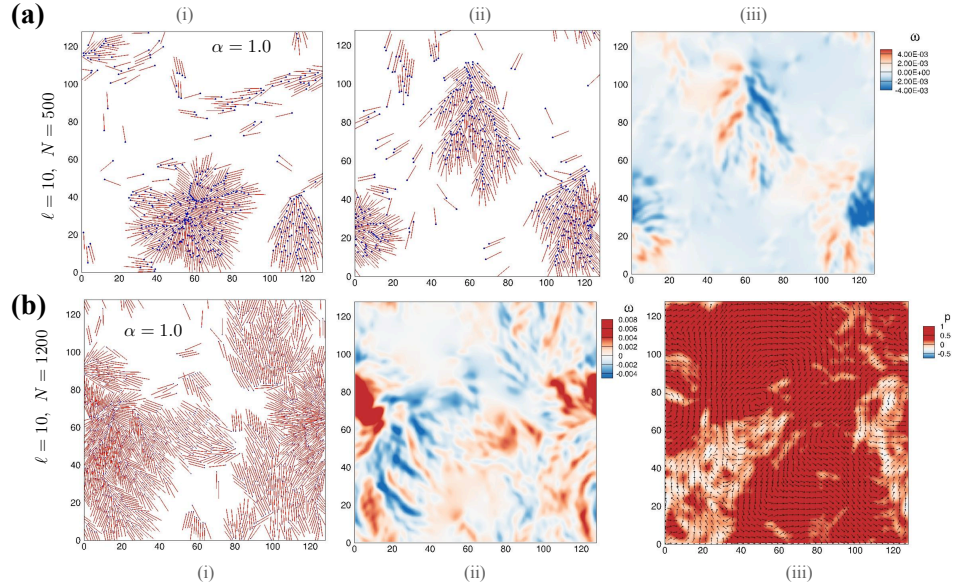
Figure 2.9: Test simulations of elongated rods at two different densities. To further validate the model works with a range of rod lengths, I increased the length of the rods from L = 5 to L = 10 in dilute (ψ = 0.33, **(a)**) and dense (ψ = 0.80, **(b)**) systems. Hydrodynamic strength is fixed at α=1. **(a)**
shows a dilute system where some rods cluster. **(b)** shows the dense system where the size of the calculate vorticity is larger. The effect of aspect ratio is explored further in **chapter 3**.

phase-field order parameter given by equation (2.3). *Note that fluctuations in intensity are tracked not the intensity itself.* The filtered phase field has value -1 corresponding to the completely passive phase and +1 corresponding to the fully active phase. The interface location and shape obtained thus was consistent with the interface obtained using velocity fluctuations [1, 2].

In our simulations however, rods can be directly tracked and there is no direct analogue to intensity fluctuations. We used a modified order parameter based on number densities (the subscript S denoting simulation)

$$\phi_{\mathrm{S}} = \begin{cases} (n_a - n_p)(n_a + n_p)^{-1}, & \text{if } (n_a + n_p) > 0 \\ 0, & \text{otherwise,} \end{cases} \tag{2.21}$$

where n_a and n_d are the number density of rod segments for active and passive bacteria, respectively. Here $\phi_{\mathrm{S}} = 1$ corresponds to the purely active phase and $\phi_{\mathrm{S}} = -1$ corresponds to the purely passive phase. The exact value $\phi_{\mathrm{S}} = 0$ corresponds to the regions of equal number of active and passive rods, or the regions that are void of bacteria. We focus attention on the first case; the second where voids can form in the active phase is interesting in itself and is connected to large scale density fluctuations observed in active matter models [17, 12].

Note that equation (2.21) exhibits a feature that is not observed or cannot be discerned from experiments. The rod simulations sometimes show voids where there are no rods (active or passive) and hence by definition $\phi_S = 0$ since $n_a + n_p = 0$. This should be distinguished from the case where $n_a = n_p$. Consequently, we will distinguish the manner in which the phase-field is evaluated to zero in subsequent discussions.

Motivated by the success of the phase-field approach in tracking the experimentally observed interface location, we employ a similar method. The interface height h, is calculated by fitting ϕ_{S} in a vertical slice with $\phi_{\mathrm{S}} = \tanh((y - h)/d)$. This calculation of interface is
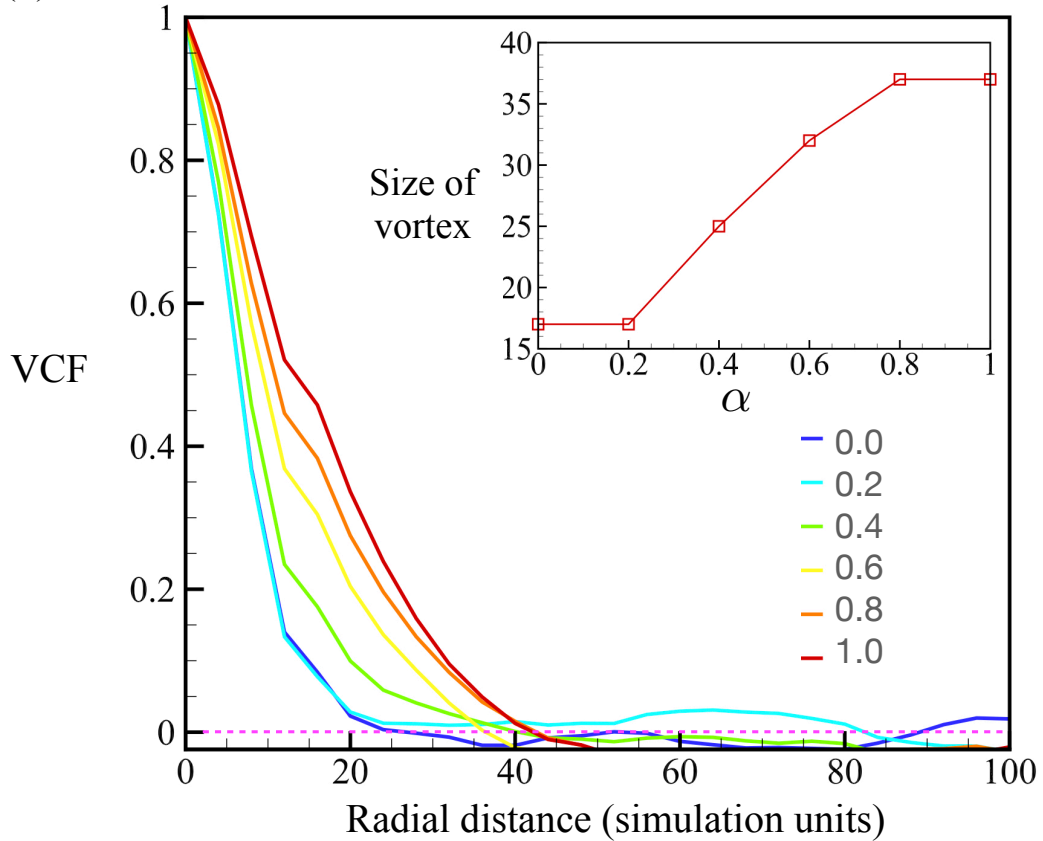
Figure 2.10: Velocity correlation function (VCF) calculated in the active phase are plotted here for a range of hydrodynamic stresslet strengths ($\alpha = 0.0\text{-}1.0$), reproduced from [37]. (Inset) Vortex sizes (diameters) measured in bacterial widths (≈ 1 μm). Vortex sizes in experiments can range from 20-35 μm and the tests shown here encapsulate these ranges and validate the SPR model.

capable of dealing with possible overhangs and mixing in the active-passive interface. The interface roughness is subsequently evaluated by using the same equation as in the experiments - equation (2.5).

2.4.4 Morphology of the propagating interface

We first investigated the rod configuration and averaged density and velocity/vorticity fields in the active-passive interface for self-propelled rods in two limits - without hydrodynamic interactions between rods (no HI), and with full Stokesian hydrodynamics (with HI). Figures 2.7 illustrates striking features of the interface motion and suggest significant changes in interface structure when HI is present.

When the hydrodynamic effects are excluded (Figure 2.7(a)), the rods only interact with each other through the short-range steric interactions. In the active phase, bacteria have a pronounced tendency to form collective structures such as flocks and streamers; these are nematic structures with groups of bacteria are moving towards the same direction. The bacteria comprising these structures are more likely to penetrate and form incisive cracks in the passive phase. Eventually these protrusions form finger-like or island-like (if these are disconnected from the active phase) regions in the passive phase. Since the passive bacteria
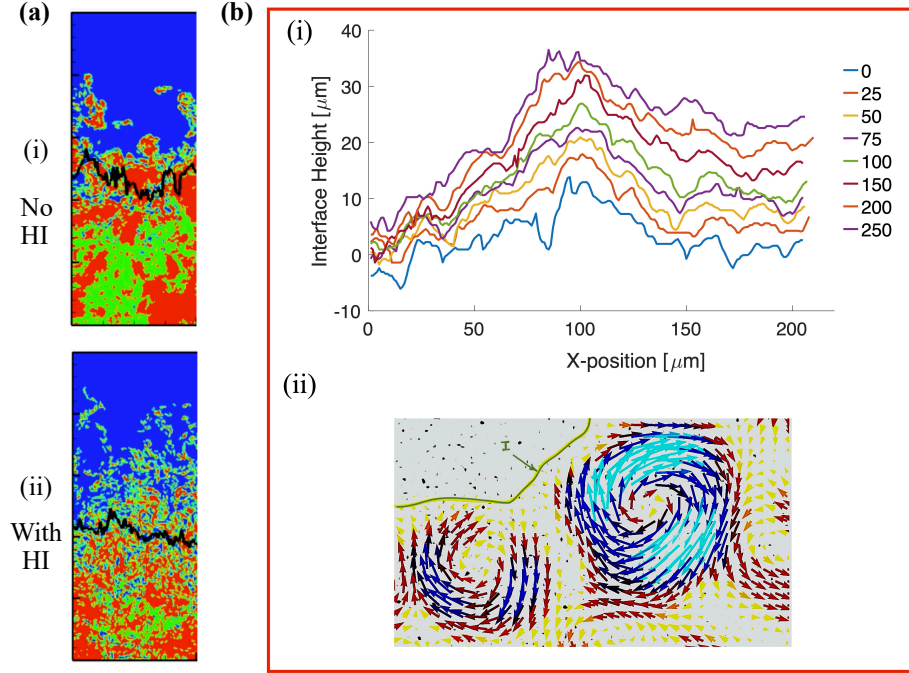
Figure 2.11: (a) Here, we highlight the role of hydrodynamic interactions in significantly modifying both the interface morphology, effective thickness as well as propagation speed. We note that the interface without HI (i), is less diffuse than the interface when hydrodynamic interactions are present (ii). We note also the increase in voids in the active phase, fast moving large-scale flocks traveling in the passive phase and the significantly lower mixing in the absence of HI. Finally comparison of the jagged black lines - the computed interface heights and profiles - suggests that the effective roughness is also dependent on the presence of hydrodynamic interactions. (b) (i) Experimental results for h(x,t) (time stamp here in seconds), illustrating an instance where a local protuberances first forms and then grows (forming fingers) and intrudes into the passive region. However the fingers are not as pronounced; suggesting a response intermediate between the dry state (no HI) and fully wet state (HI dominates). (ii) These sharp features of the evolving interface are typically connected to the presence of sharp vortical structures (either rotating the same way or in opposite senses) that stretch and convect material points (bacteria) in the interface region. Data in **(a)** was produced in collaboration with Dr. Yuchen Zhang and Dr. Arezoo Ardekani. Data in **(b)** was obtained from analysis of experimental datasets from [1, 2].

cannot enter the active phase due to being immotile and have to be convected by the incoming active bacteria, there is net flux of bacteria from the active phase to the passive phase. Right below the active-passive interface, there we observe significant number of voids where very few active bacteria are present. Furthermore, voids span multiple bacterial lengths.

When hydrodynamic interactions are included as shown in Figure 2.7(b), active and passive phases are better mixed and the fingering seen previously is not observed possibly due to HI induced destabilization. The length scale of nematic structures generated in the passive domain decreases due to active flows. Passive bacteria are displaced and advected through the active region in both cases eventually leading to mixing. We anticipate that continuous realignment and instabilities are due to local shearing flows generated over the scale of many bacteria. Note again that we do not have diffusion in our simulations, and hence this destabilization is from hydrodynamic effects; the final result is an active, turbulent motion of rods [10] with highly vortical structures. The flow vortices lead to breakup of the active-passive interface and substantially enhance the mixing between the active and passive phases.

Comparison of sequences in Figure 2.7(a) and Figure 2.7(b) clarify the nature of structural differences in the interface region, and the variations in the manner in which the leading front propagates without and with HI. Hydrodynamic interactions are associated with a reduced occurrence of dendritic protrusions that may pinch off, penetrate and move through the frictional passive region. Furthermore, we see larger (white) voids with lower values of local densities when hydrodynamic interactions are neglected. We also note larger local interface mixing speeds when hydrodynamic interactions are included. The interface region is more smeared out and exhibits the hallmark of a mushy, bi-phasic mixed region when hydrodynamic interactions are present.

As anticipated from Figure 2.7, we observed the following: (i) The front in the absence of HI clearly demonstrates fingering and clustering with these pinching off and moving deep into the passive frictional domain. (ii) Non-HI simulations demonstrate significant density variations in the active phase, reminiscent of the large amplitude density fluctuations seen in model theoretical active polar and nematic systems [13, 10]. These fluctuations are usually smeared out when hydrodynamic interactions are allowed. (iii) Finally, again as expected, HI smears out the interface region which now possesses features of a diffuse interface. Note that a finite interface thickness was calculated in the *Serratia* experiments and reported earlier by us [1] using both intensity variations (a stand-in for density variations) as also independently using PIV. Here we see that hydrodynamic interactions significantly thicken the apparent interface - i.e, there is truly a well mixed bi-phasic region when HI is present.

Examination of the associated vorticity fields shows that vortical structures are slightly larger and more segregated when hydrodynamic interactions are non-existent. For rods without hydrodynamics, the vortices are elongated and connected due to the presence of the nematic structures. When hydrodynamics are included, the vortices are broken, creating mesoscale turbulence and leading to a more disordered flow field. Here, the magnitude of flow velocity and vorticity are larger than those without hydrodynamics interactions, and there is a slight flow in the passive phase since the hydrodynamic interaction decays slowly with distance.

Hydrodynamic interactions impact not just the morphology and structure of the interface region but also the evolution and dynamics. The striking difference between simulations without and with HI are evident in Figures 2.11(a)-(i) and 2.11(a)-(ii). Note the increasingly bi-phasic structure of the interface region due to hydrodynamic interactions; additionally, this mushy region gradually increases in width due to mixing. Green domains deep in the active phase observed in Figure 2.11(a)-(i) corresponding to voids or low density regions are significantly less for the case with HI than without.

2.4.5 Vorticity fields and velocity correlations

To check the effect of the bounding walls as well as to investigate how velocity fields observed in our simulations compared with experiments, we next analyzed the vorticity distribution and velocity correlations far from the active-passive interface region. We note that vorticity magnitudes across the active region are consistently similar once we move away from the interface and deep into the active region (yellow box). As time progresses however the distance between vortical structures increases slightly possibly due to the mixing and convective flux of passive rods into the active phase.

To quantify the structural features of the velocity field, in addition to the vorticity field, of the vortical structures in this region, we calculate the velocity correlation function (VCF) in Figure 2.10, choosing the region $100 < y < 300$. Furthermore, to discern effects due to HI, we analyze simulations with and without HI. Given the VCF, characteristic vortex sizes can be found from the length-scale at which VCF equals 0 and crosses over to positive values. As time goes by, for either with or without hydrodynamics, the number density of active bacteria at the studied region decreases because some active bacteria penetrate into the

passive domain.

Associated with the decrease in number density is an increase in vortex radius. Interestingly, these conclusions are consistent with our reported observations on slightly increases in size and longer residence time of vortical structures close to the interface [1] (and thus higher density of passive rods). Thus our computations capture qualitative features of the swarm and predict correlation lengths consistent with experiments.

2.4.6 Roughness of the interface and comparison with experiments

Finally, combining experiments with simulations, we conclude that hydrodynamic and steric interactions enable different modes of surface dynamics, morphology and thus front invasion. This is clearly seen when one compares the vorticity fields in the interface region for simulations with and without HI (Figure 2.11. In the absence of HI such as for dry systems where the only contribution from ambient fluid is the Stokes drag on the rods, we observe a sharper interface structure, albeit with a more disruptive morphology and extensive fingering. Flocks and streamers can develop at the interface, and exploiting any structural weakening in the passive phase can pinch off and penetrate the frictional medium. What is noteworthy is that these clusters are also characterized by strong vorticity and thus involve circulatory motions.

2.5 Summary and Outlook

Swarming is a complex multi-cellular response featuring fast, collective and long ranged intense bacteria laden flows [38, 39] and enables efficient and rapid colonization of environments and biologically important surfaces. This phenomenon requires the integration of multiple and multimodal chemical and physical signals, including physiological and morphological differentiation of the bacteria into swarmer cells, the optimal presence of nutrient and favorable porous surfaces [38, 39, 7]. A significant component of the swarming state are interfaces or propagating fronts that form naturally allowing swarms to invade free space or highly frictional domains. Here, we study the evolving structural features of an active-passive interfaces using dense colonies of *Serratia marcescens* as a model system. We image the evolution, dynamics and morphology of the interface region between an active (swarming) phase and a passive (immotile) phase. The passive phase is densely packed and micro-structured and hence offers an highly frictional environment. Integrating results from Particle Image Velocimetry (PIV), intensity based image analysis and analysis of surface fluctuations, we quantify the dynamics and morphology of the evolving interface. We show that correlations between spatially separated surface fluctuations and damping of the same are influenced by the interaction of the interfacial region with adjacently located collective flows. Furthermore, dynamical growth exponents characterizing the active manner in which the interfacial region is continuously reshaped differ significantly from classically expected values.

To complement and interpret our experiments, we presented a high-performance numerical simulation that explicitly tracks the motion of each bacteria with consideration of both cell-cell steric interaction and far-field hydrodynamic interactions. The simulations are able to separate the steric and hydrodynamic effects and illustrate the time evolution of mixing between the active and dead bacteria swarms for either with or without hydrodynamic interactions. The hydrodynamic effects have a tendency to create turbulence in active phase, which disturbs the active-passive interface and thus enhance the mixing between passive and active bacteria. The *active turbulence* also decreases the length scale of the nematic structure and make it easier for active bacteria to penetrate the passive phase. At the same time, simulations in the dry regime - where hydrodynamic interactions are neglected - strongly

indicate significant fingering instabilities with macro-scale flocks penetrating the passive phase, pinching off from the rest of the active domain and covering significant territory in the passive region before fragmenting. The interface with hydrodynamic effects shows larger roughness exponent and dynamic exponent than those without hydrodynamic effects, but the growth exponents are similar.

Combining experiments with simulations, we conclude that hydrodynamic and steric interactions enable strikingly different modes of surface dynamics, morphology and thus front invasion. Swarms typically utilize and move in nutrient-laden ambient fluid in a swarm that is extracted from underlying soft poroelastic fluid infiltrated substrates. Our observations imply that surfaces tailored with a friction gradient or a porosity gradient may hinder swarm propagation significantly.

We conclude with some possible extensions of this work. Our results strongly motivate the need for further careful experimentation where bacterial swarm intensity (density and/or self-propulsion), the substrate friction and softness can all be varied independently. This will allow us to investigate carefully the physicochemical and biophysical conditions under which the front propagation and attendant instabilities may be suppressed or enhanced. In turn, this information will also help elucidate the mechanisms underlying the formation of jets and streamers observed in many advancing bacterial interfaces. The agent-based numerical model we studied considered the propagation of swarms into frictional domains and was motivated by the manner in which bacteria may reconstitute and reclaim territory, and also the manner in which bacteria may physically interact with sub-domains of other bacterial species or mutants with strongly contrasting self-propulsion. It would be of interest to generalize our treatment by allowing the self-propulsion speed and viscous friction to depend on biophysical parameters such as substrate properties. Similarly, introducing a dependence on an ambient diffusing chemical may provide a minimal model of quorum sensing. Finally, in order to probe the active matter related aspects of swarming matter such as the co-existence and formation of phases, one can combine the agent-based microscopic models presented in this paper with mesoscale models for active liquid crystals [17, 18, 20, 19, 21].

Bibliography

[1] A. E. Patteson, A. Gopinath, and P. E. Arratia, "The propagation of active-passive interfaces in bacterial swarms," *Nature Communications*, vol. 9, no. 1, p. 5373, 2018.

[2] J. Yang, P. E. Arratia, A. E. Patteson, and A. Gopinath, "Quenching active swarms: effects of light exposure on collective motility in swarming Serratia marcescens," *Journal of The Royal Society Interface*, vol. 16, no. 156, p. 20180960, 2019.

[3] A. Gopinath, R. C. Armstrong, and R. A. Brown, "Second order sharp-interface and thin-interface asymptotic analyses and error minimization for phase-field descriptions of two-sided dilute binary alloy solidification," *J. Cryst. Growth*, vol. 291, no. 1, pp. 272–289, 2006.

[4] N. C. Darnton, L. Turner, S. Rojevsky, and H. C. Berg, "Dynamics of bacterial swarming.," *Biophysical journal*, vol. 98, no. 10, pp. 2082–90, 2010.

[5] E. B. Steager, C.-B. Kim, and M. J. Kim, "Dynamics of pattern formation in bacterial swarms," *Physics of Fluids*, vol. 20, no. 7, p. 073601, 2008.

[6] E. Steager, C. B. Kim, J. Patel, S. Bith, C. Naik, L. Reber, and M. J. Kim, "Control of microfabricated structures powered by flagellated bacteria using phototaxis," *Applied Physics Letters*, vol. 90, no. 26, p. 263901, 2007.

[7] M. F. Copeland and D. B. Weibel, "Bacterial swarming: A model system for studying dynamic self-assembly," *Soft matter*, vol. 5, no. 6, pp. 1174–1187, 2009.

[8] S. B. E. Ben-Jacob, G. Ariel, and A. Be'er, "Antibiotic-induced anomalous statistics of collective bacterial swarming," *Phy. Rev. Lett.*, vol. 114, p. 018105, 2015.

[9] J. Dunkel, S. Heidenreich, K. Drescher, H. H. Wensink, M. Bär, and R. E. Goldstein, "Fluid dynamics of bacterial turbulence," *Physical review letters*, vol. 110, no. 22, p. 228102, 2013.

[10] E. Lushi, H. Wioland, and R. E. Goldstein, "Fluid flows created by swimming bacteria drive self-organization in confined suspensions," *Proceedings of the National Academy of Sciences*, vol. 111, no. 27, pp. 9733–9738, 2014.

[11] A. E. Patteson, A. Gopinath, M. Goulian, and P. E. Arratia, "Running and tumbling with e. coli in polymeric solutions," *Scientific Reports*, vol. 5, p. 15761, 2015.

[12] A. E. Patteson, A. Gopinath, and P. E. Arratia, "Active colloids in complex fluids," *Current Opinion in Colloid & Interface Science*, vol. 21, pp. 86–96, 2016.

[13] H. H. Wensink, J. Dunkel, S. Heidenreich, K. Drescher, R. E. Goldstein, H. Löwen, and J. M. Yeomans, "Meso-scale turbulence in living fluids," *Proceedings of the National Academy of Sciences*, vol. 109, no. 36, pp. 14308–14313, 2012.

[14] M. C. Marchetti, J. F. Joanny, S. Ramaswamy, T. B. Liverpool, J. Prost, M. Rao, and R. A. Simha, "Hydrodynamics of soft active matter," *Review of Modern Physics*, vol. 85, p. 1143, 2013.

[15] S. Ramaswamy, "Active matter," *Journal of Statistical Mechanics: Theory and Experiment*, vol. 2017, p. 054002, 2017.

[16] V. Bratanov, F. Jenko, and E. Frey, "New class of turbulence in active fluids," *Proceedings of the National Academy of Sciences USA*, vol. 112, no. 49, pp. 15048–15053, 2015.

[17] A. Gopinath, M. F. Hagan, and M. C. Marchetti, "and a. baskaran (2012) dynamical self-regulation in self-propelled particle flows," *Physical Review E*, vol. 85, no. 6, p. 061903, 2015.

[18] A. Doostmohammadi, J. Ignés-Mullol, J. M. Yeomans, and F. Sagués, "Active nematics," *Nature Communications*, vol. 9, p. 3246, 2018.

[19] S. Chandragiri, A. Doostmohammadi, J. M. Yeomans, and S. P. Thampi, "Active transport in a channel: stabilisation by flow or thermodynamics," *Soft Matter*, vol. 15, pp. 1597–1604, 2019.

[20] N. A. M. A. R. C. V. Coelho and M. M. T. da Gama, "Active nematic–isotropic interfaces in channels," *Soft Matter*, vol. 15, pp. 6819–6829, 2012.

[21] N. A. M. A. R. C. V. Coelho and M. M. T. da Gama, *Propagation of active nematic–isotropic interfaces on substrates.* Soft Matter, 2020.

[22] J. Schindelin, I. Arganda-Carreras, E. Frise, V. Kaynig, M. Longair, T. Pietzsch, S. Preibisch, C. Rueden, S. Saalfeld, B. Schmid, J.-Y. Tinevez, D. J. White, V. Hartenstein, K. Eliceiri, P. Tomancak, and A. Cardona, "Fiji: an open-source platform for biological-image analysis," *Nature Methods*, vol. 9, no. 7, p. 676–682, 2012.

[23] W. Thielicke and E. Stamhuis, "Pivlab - towards user-friendly, affordable and accurate digital particle image velocimetry in matlab," *Journal of Open Research Software*, vol. 2, p. 1, 2014.

[24] L. Turner, R. Zhang, N. C. Darnton, and H. C. Berg, "Visualization of flagella during bacterial swarming," *Journal of Bacteriology*, vol. 192, no. 13, pp. 3259–67, 2010.

[25] A. Gopinath, R. C. Armstrong, and R. A. Brown, "Observations on the eigenspectrum of the linearized doi equation with application to numerical simulations of liquid crystal suspensions," *The Journal of Chemical Physics*, vol. 121, no. 12, p. 6093–6094, 2004.

[26] A. Gopinath, L. Mahadevan, and R. C. Armstrong, "Transitions to nematic states in homogeneous suspensions of high aspect ratio magnetic rods," *Phys. Fluids*, vol. 18, no. 2, p. 028102, 2006.

[27] M. Kardar, G. Parisi, and Y.-C. Zhang, "Dynamic scaling of growing interfaces," *Physical Review Letters*, vol. 56, p. 889, 1986.

[28] T. Vicsek, *Fractal growth phenomena.* Singapore: World Scientific, 2nd ed., 1992.

[29] A. L. Barabasi and H. E. Stanley, *Fractal concepts in surface growth.* Cambridge University Press, 1995.

[30] L. G. Wilson, V. A. Martinez, J. Schwarz-Linek, J. Tailleur, G. Bryant, P. N. Pusey, and W. C. K. Poon, "Differential dynamic microscopy of bacterial motility," *Phys. Rev. Lett.*, vol. 106, p. 018101, 2011.

[31] S. F. Edwards and D. R. Wilkinson, "The surface statistics of a granular aggregate," *Proc. Roy. Soc. A*, vol. 381, no. 1780, pp. 17–31, 1982.

[32] S. Broersma, "Viscous force and torque constants for a cylinder," *Chem. Phys.*, vol. 74, p. 6989, 1981.

[33] T. Kirchhoff, H. Löwen, and R. Klein, "Dynamical correlations in suspensions of charged rodlike macromolecules," *Phys. Rev. E*, vol. 53, no. 5, p. 5011, 1996.

[34] S. Plimpton, "Fast parallel algorithms for short-range molecular dynamics," *Journal of Computational Physics*, vol. 117, no. 1, pp. 1–17, 1995.

[35] Y. Zhang, G. Li, and A. M. Ardekani, "Reduced viscosity for flagella moving in a solution of long polymer chains," *Physical Review Fluids*, vol. 3, no. 2, p. 023101, 2018.

[36] G. Li and A. M. Ardekani, "Collective motion of microorganisms in a viscoelastic fluid," *Physical Review Letters*, vol. 117, p. 118001, 2016.

[37] J. Tamayo, Y. Zhang, A. E. Patteson, A. M. Ardekani, and A. Gopinath, "Swarming bacterial fronts: Dynamics and morphology of active swarm interfaces propagating through passive frictional domains," *bioRxiv*, p. 2020.04.18.048637, 2020.

[38] L. Alberti and R. M. Harshey, "Differentiation of serratia marcescens 274 into swimmer and swarmer cells," *Journal of Bacteriology*, vol. 172, p. 4322, 1990.

[39] R. M. Harshey, "Bacterial motility on a surface: Many ways to a common goal," *Annual Reviews Microbiology*, vol. 57, pp. 249–273, 2003.

Chapter 3

Factors affecting the persistence of clusters in diluted swarms

3.1 Introduction

In **chapter 2**, I reported on the spatiotemporal dynamics of the active-passive interface in dense swarms and dense SPR simulations. As previously mentioned, however, assessing how these rod-like cells gather into clusters, and the role these clusters play into the formation of swarming structural features is not trivial due to the high density and multi-layer formation of *S. marcescens*. Therefore, it is of interest to study dilute systems of swarming bacteria to elucidate the effects of interactions between small, clearly distinguishable clusters. Here, I utilize the SPR model introduced in **chapter 2** and elaborate on in section 3.2 to simulate systems of rods at low density ($\Psi = 0.33$). At this density, clusters can be observed moving independently and can be observed interacting with one another as opposed to dense simulations where clusters cannot be as clearly identified.

One clear benefit of cell elongation is upregulating flagellar synthesis in a process called hyperflagellation, increasing the flagellar count and increasing the thrust of the cell [1, 2]. The mean speed of bacteria increases when they transition to this state. The increase in speed of longer swarming cells can confer higher rates of propagation and survivability of cells [3, 4]. Another potential benefit to elongation is that longer length swarmers may promote increased clustering and rafting. Swarms possess a wide distribution of bacterial lengths and have sub-populations of highly elongated bacteria. These extremely long cells may act as recruitment sites for rafting, as shorter cells will collide with these cells and reorient parallel to the long cell and raft together [5, 6, 7, 8]. As a precursor, I observe clusters of swarming *S. marcescens* in figure 3.1, where I diluted a dense swarm with LB media in order to better observe smaller numbers of bacteria.

At low bacterial densities, cells exhibit the aforementioned run-and-tumble motion. In this state, prior to swarming, no collective motion takes places as cells randomly explore their surroundings in search of nutrients. As swarming is a collective form of motion, density may play a crucial role in the ability to swarm. When swarming cells are diluted to densities where they can be observed in small groups, the cells exhibit collective motion, clustering, and rafting. A mapping of the effect of density and aspect ratio on *B. subtilis* was conducted, mapping a wide range of aspect ratios from planktonic length to hyper elongated cells at very low and very high densities ($\Psi = 0.1 - 0.7$) [7]. Very low densities may inhibit swarming motion as there will be lower frequency of cell-cell interactions which are required for bacteria to cluster and move together. Very high densities, across all measured aspect ratios from that study can induce jammed states that hinder bacteria motility. Depending on the aspect ratio, different densities can induce swarming and influence the formation of small, local clusters, or larger clusters that are comprised of several dozen bacteria. In section 3.3, I report on the effect of elongation by independently tuning the aspect ratio of the rods from L = 3, 5, 10 which correspond to bacteria aspect ratios similar to their swimming state (L = 3) to very high aspect ratios seen in swarming bacteria (L = 10).

Agent-based models of Active Brownian Particles (ABP) have been utilized to study alignment and rafting behavior of swarming bacteria and active matter systems [9, 10, 11]. An ABP is modeled through the Langevin equations that include self-propulsion terms and effects from thermal noise to capture the motion of bacterial swimmers and crawling mammalian cells [12, 13, 14, 15]. Periodic vortex arrays, observed in the swarm front, have been simulated using a minimal model that includes only steric interactions between particles and neglects long-range hydrodynamics, highlighting the importance of steric cell-cell interactions in the formation of structures in collective motion [16]. Self-organization can occur in active matter systems and is of key importance to the fitness and surviability of a colony [17]. When hydrodynamics are neglected, the vortices are elongated and connected due to the presence of the nematic structures. When hydrodynamics are included, the vortices become irregular and topological defects occur which are characteristic of mesoscale turbulence of the system is observed [18]. A key limitation to ABPs however, is their circular shape and do not represpent the morphology of bacteria swarmers.
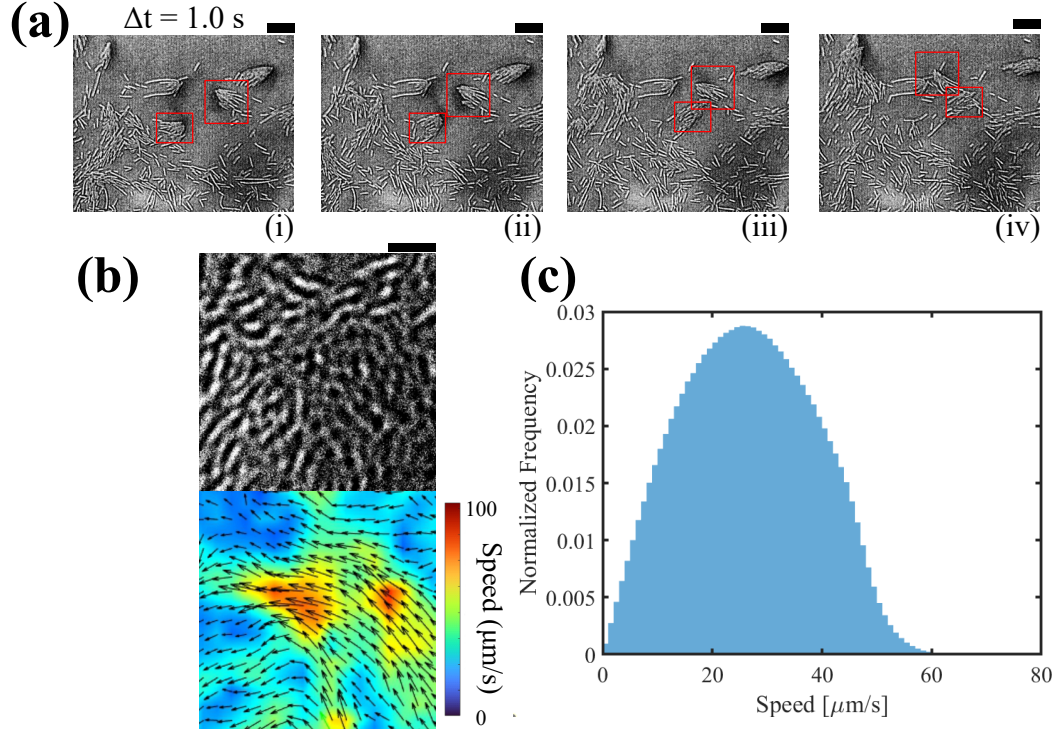
Figure 3.1: Experimental snapshots of swarming *S. marcescens* in dilute systems **(a)** and dense systems **(b)**. **(a)**. Diluted swarm generated with a 1 μL droplet of LB media added ahead of the swarm front. Examples of rafts are indicated by red squares. Scale bars are 20 μm. **(b,top)** Dense suspension of the *S. marcescens*. The area of the image is 50x50 μm where focused snapshots of Particle Image Velocimetry (PIV) analysis is shown in (b, ii-v). **(b, bottom)** PIV snapshots capturing the bacteria speeds (color map) and direction of flow (black arrows). Scale bar shown is 10 μm. **(c)** Velocity distribution taken from PIV analysis over 30 seconds from the dense swarm in **(b)**.

Meanwhile, SPR models are more complex agent based models that appropriately capture the morphology of flagellated bacteria rods. Motivated by monolayers of growing *P. aeruginosa* and presence of topological defects within those colonies, SPR simulations were previously utilized to study and mimic movement, orientation, and flow fields of the colony, all of which are mediated by the movement of $+1/2$ and $-1/2$ topological defects formed by interacting SPRs [19]. Studies of rod-like spheroidal squirmers with hydrodynamic interactions also find that increased aspect ratio increases phase separation and promotes clustering [20, 21]. All of this taken together motivates the exploration of the role of cell aspect ratio and hydrodynamics on swarming systems and is the topic of this chapter.

3.2 Methods

3.2.1 Simulations

The simulations on dilute systems of rod-like swarmers utilize the same code as described in **chapter 2** of this dissertation. Here, I briefly describe the key features of the model and the significant changes to the parameters in this section. To capture the morphology of a swarming bacterium and interactions between cells, I simulate a bacterium as a slender rod with a length L and width λ. I model the rod length as a series of $n = L + 1$ connected

points. Therefore, the aspect ratio, defined as the length-to-width proportion of the rods and is given by $A = L/\lambda$. I model the rods moving in a Newtonian fluid with a shear viscosity μ, and density ρ. The rods can self-propel with a intrinsic self-propulsion speed, μ_0, where for swarms of *S. marcescens*, the mean swarming speed is $\mu_0 \approx 28\frac{\mu m}{s}$ and $V = 1 \equiv 28\frac{\mu m}{s}$. Therefore, the rods move in a water-like low-Reynold's number fluid given by $Re \equiv (L\mu_0\rho)/\mu \ll 1$ and the use of Stokes equation is appropriate. The simulation domain area, A, is 128λx128λ for dilute suspensions and 256λx256λ for dense suspensions as I study both dilute and dense suspensions of rods, I define the density of the simulations as an area fraction, given by $\Psi = n(L+1)\lambda/A$. For dilute simulations, $\Psi \sim 0.33$. For the agent-based model, each rod is indexed to track their positions and orientations over time. The equations of motion of a rod of index γ in the environment are defined as:

$$\frac{dr^\gamma}{dt} = u_h + V\mathbf{p}^\gamma + \mathbf{f_T^{-1}} \cdot \mathbf{F_s} \tag{3.1}$$

$$\omega^\gamma = \omega_h + \mathbf{f_R^{-1}} \cdot \mathbf{T_s} \tag{3.2}$$

where Eqn.3.1 describes the position of the rod with time and Eqn.3.2 describes the orientation of the rod with time. $\mathbf{f}_T$ and $\mathbf{f}_R$ denote the translational and rotational friction tensors. $\mathbf{F}_s$ and $\mathbf{T}_s$ are the force and torque of the rod due to steric interactions with other rods.

Steric Interactions

Steric interactions between rods are modeled with the Yukawa potential as defined in **chapter 2**, which I define again as:

$$U^A = \frac{1}{2} \sum_{B \neq A} H(R_c - r^{AB}) \frac{U_0}{n^2} \sum_{i=1}^{n} \sum_{j=1}^{n} \frac{1}{r_{ij}^{AB}} \exp\left(\frac{-r_{ij}^{AB}}{\lambda}\right) \tag{3.3}$$

Hydrodynamic Interactions

To capture the effects of cell-fluid/hydrodynamic interactions, the self-propelled rods are modeled as a series of rigid points, where the force distribution along n points of the rod, indexed by l_i, is defined as: $F_i = ((2\alpha_h)/n)(l_i/|l_i|)V\mathbf{p}$, where α_h represents the dimensionless stresslet strength of the rods and is the parameter that I tune to affect cell-fluid interactions. In this study $\alpha_h = 1$ is the same stresslet strength used to study active-passive interface systems in **chapter 2**. I vary this stresslet strength from the "dry" limit, $\alpha_h = 0.1$ to an extreme wet limit, $\alpha_h = 160$ where hydrodynamic contributions are expected to complete dominate steric interactions. These parameters are listed in table 3.1.

Simulating dilute and dense systems of rods

As most swarming colonies are dense suspensions of bacteria, it is difficult to observe individual clusters and asses how their dynamics change over time. To study the collective motion of these rafts and clusters, I simulate dilute suspensions of rods ($\Psi \sim 0.33$) and vary two parameters independently (Table 3.1): the rod length (L) and the stresslet strength of the rods (α_h). In the system, $\Psi = N(L+1)\lambda \cdot A^{-1}$. As the rod length affects the area fraction, I adjust the number of rods, N, to maintain the dilute system of rods at $\Psi = 0.33$.

The rods in the system are initialized as evenly space lattices and allowed to develop until the rods are well-mixed. All analysis presented in this text is conducted after the system is well-mixed and is determined when the mean pressure and vorticity reach a quasi-steady-state.

Rod Lengths (L)	Rod Width(λ)	Area Fraction (Ψ)	Velocity (V)	Stresslet Strength (α_h)	Simulation domain area
3, 5, 10	1	0.33	1	0.1, 0.25, 0.5, 1, 10, 160	(128x128)λ
5	1	0.72	1	1	(256x256)λ

Table 3.1: Table of simulation parameters. Here, the rod width $\lambda = 1$ μm (≈ 1 bacteria width). The velocity, V $= 1 = 28$ μm (mean swarm speed)

In this text, histograms are represented as normalized probability density functions and are labeled as *normalized frequency* in text. The equation for the normalized frequency of measured lengths in Figure 3.2(a):

$$P(L) = \frac{L_i}{N} \tag{3.4}$$

where $P(L)$ is the probability of finding a length of a bacteria, L, across a 30 second video. L_i is the length of a bacterium with index i. N is the total number of bacteria measured. Each cell was measured once.

Here, I assess the lifetime/persistence time of clusters via the temporal speed and orientation autocorrelation function. The equation is is given by:

$$C_V(\tau) = \langle \frac{V_\alpha(t_0)V_\alpha(t_0 + \tau)}{|V_\alpha(t_0)|^2} \rangle \tag{3.5}$$

where C_V is the autocorrelation function at delay time τ, and the angle brackets denote an ensemble average of the correlation functions for each rod in the system. The time C_V crosses zero is the correlation time of the cluster, in other words, the average time τ a cluster remains stable before rods begin to leave the cluster is such that $C_V(\tau) = 0$.

Similarly, the orientational autocorrelation function is given by:

$$C_\theta(\tau) = \langle \frac{\theta_\alpha(t_0)\theta_\alpha(t_0 + \tau)}{|\theta_\alpha(t_0)|^2} \rangle \tag{3.6}$$

where C_θ is the autocorrelation function at delay time τ, and where θ is the orientation of the rod in radians, measured from the positive x-axis on a Cartesian coordinate system.

The autocorrelation functions are fit to the expression $y = \exp -t/\tau$ where τ is selected to obtain the best fit to the functions would give the correlation time for the rod velocities and orientations.

The motility of the rods and clusters can be described by calculating the mean squared displacement (MSD) of the rods and the equation is given by:

$$\langle \Delta \mathbf{r}^2(\tau) \rangle = \langle |\mathbf{r}(t + \tau) - \mathbf{r}(t)| \rangle \tag{3.7}$$

where $\mathbf{r}(\tau)$, is the position of rod in the system at time and τ is the delay time from initial observation. Angled brackets ($\langle \Delta \mathbf{r}^2(\tau) \rangle$) denote an ensemble average of the MSDs of all rods in the system. The slope of the MSD versus τ on a logarithmic plot informs us how efficiently the rods explore the space, where a slope of 1 ($MSD(\tau) \propto \tau$) is diffusive behavior and acts like a random Brownian particle, while a slope of 2 ($MSD(\tau) \propto \tau^2$) is ballistic behavior

where the trajectories are straighter and there is significantly less random reorientation of the rods [9, 22].

The two particle MSD is given by:

$$\Delta \mathbf{r}^2_{AB}(\tau) = |\mathbf{r}_{AB}(t+\tau) - \mathbf{r}_{AB}(t)| \tag{3.8}$$

where $\mathbf{r}_{AB} = \mathbf{r}_A - \mathbf{r}_B$.

Rod clusters are identified by binarizing the rods at each time-point. I assume that each rod contains the same amount of pixels to generate the image and take a sum of all white pixels at the beginning of the simulation. An in-house MATLAB code was then used to determine how many white pixels are adjacent and are therefore "connected". Based on the connected pixel count I then estimate how many rods are adjacent and considered a cluster.

Histogram plots of cluster sizes are plotted as normalized PDFs and referred to as normalized frequencies of a particular set of cluster sizes occurring. In the SPR simulations, cluster sizes were measured every $t = 2.5$ simulated seconds and histogram plots reflect cluster sizes being measured over the duration of the simulation.

3.2.2 Experimental Setup and Analysis

The *in-silico* rods are modelled after experiments on swarming *Serratia marcescens* (WT American Type Culture Collection 274). The colonies were cultured in LB broth overnight at 37 °C. The cultures were grown until mid-log phase (OD600 = 0.6) and cell density was measured with a Vernier GoDirect SpectroVis Plus spectrophotometer. 5 μL of inoculum was pipetted onto the center of 0.6% (w/v) agar plates (1% Bacto Tryptone, 0.5% yeast extract, 0.5% NaCl and 0.6% Bacto Agar in deionized water, measured in w/v percents. 100x15 mm petri dish.) with 300 μL of 25% glucose solution. The inoculated plate was then incubated at $37°C$ for 10-15 hours, after which time the colony was swarming. Imaging was conducted on a Nikon Ti-E inverted microscope. All videos/images were recorded with a 20x objective with a 1x or 1.5x camera magnification (effective 30x). Videos were recorded for 30 seconds. The cultures were maintained at 34° C with a Tokai-Hit stage top incubator. Videos were recorded at 100 FPS, 1 ms exposure, 30 seconds per video.

Individual cells are manually tracked using ImageJ for at least 10 seconds and until the cells are no longer trackable/visible. From their positions, their mean squared displacements can be calculated using Eq.3.7. Their speeds are estimated by $V(t) = \mathbf{r}(t) - \mathbf{r}(t - \Delta t)$, where V is the cell speed at time, t, and $\mathbf{r}$ is the position of the cell in Cartesian coordinates.

Cell velocities in the dense swarm are estimated using the MATLAB distribution of PIVLab (Particle Image Velocimetry) [23]. I analyze time-lapse videos of the swarm for at least 30 seconds using 64, 32, and 16 pixel interrogation windows which are equivalent to: 14.4, 7.2, 3.6 μm windows (20x objective) and 10.1, 5.0, 2.5 μm windows (30x objective).

The spatial average of the magnitude of vorticity ($\langle \omega^2 \rangle$) is calculated as:

$$\langle \omega^2(t) \rangle = \frac{1}{A}\Sigma_{i=1}^{N}\omega(t)_i^2 dA = \langle \omega(t)^2 \rangle \tag{3.9}$$

$$= \frac{1}{A}\Sigma_{i=1}^{N}\omega_i^2(t)\Delta A_i \tag{3.10}$$

$$= \frac{1}{N}\Sigma_{i=1}^{N}\omega_i(t) \tag{3.11}$$

Similarly, the spatial mean pressure is calculated as:

$$\langle p(t)\rangle \quad = \quad \frac{1}{A}\Sigma_{i=1}^{N}p(t)_i dA \tag{3.12}$$

$$\langle p(t)\rangle \quad = \quad \frac{1}{A}\Sigma_{i=1}^{N}p(t)_i \Delta A_i \tag{3.13}$$

$$\langle p(t)\rangle \quad = \quad \frac{1}{N}\Sigma_{i=1}^{N}p(t)_i \tag{3.14}$$

where i is a unit area A, N is the total number of unit areas within the simulation domain, and $\langle\rangle$ is an position ensemble average that calculates the vorticity and pressure across grid points in the simulations that contain the values for vorticity and pressure.

The error bars within this chapter are presented as 1 standard deviation, calculated as:

$$S = \sqrt{\frac{1}{N-1}\Sigma_{i=1}^{N}|A_i - \mu|^2} \tag{3.15}$$

where S is the standard deviation, μ is the mean of A, N is total number of grid points in the simulation domain,

3.3 Results

3.3.1 Experimental Observations

The experiments on wild-type, swarming *Serratia marcescens* in dilute suspensions reveal the dynamic and highly cooperative nature of bacteria swarming colonies. I utilized ImageJ to measure cell lengths in figure 3.2(a), confirming a wide length distribution amongst swarmers and increased mean length ($L_{\mathrm{mean}} = 8.71\mu$m) with lengths reaching up to 31 μm in the experiments. I confirm that there is significant elongation when *S. marcescens* transitions from the pre-swarming to the swarming state. Pre-swarming lengths vary from 1-8 μm in length with a mean of approximately 3 μm (N = 774). Comparing this to swarming cell lengths, there is an approximate 2-3 fold increase length, consistent with previous results [24, 25].

I then measured the speeds of cells of different lengths to assess if cell length correlates to any difference in cell speeds. I note that I do not consider interactions between cells when selecting cells, but take this into consideration in the discussion section. I calculated both the mean speed of 4 different bacteria lengths and their mean squared displacements (Figure 3.2(b, c)) finding that for bacterium longer than the mean planktonic length (Table 1.1), their motion is ballistic (MSD $\propto \tau^2$) for the observed time. Bacteria with lengths comparable to swimming bacteria, are diffusive for longer delay times and are slower than longer bacteria. I then assess the orientation autocorrelation function of two cells of lengths 10.7 and 12.6 μm, finding that for the longer cell, $C_\theta(\tau) = 0$ when $\tau = 2.25s$ and for the shorter cell, $\tau = 0.25s$ (Figure 3.2d). What is not clear from these observations alone are the effects of hydrodynamic and steric interactions between cells that may aid in their ability to cooperate and collectively move. To capture these features of bacteria swarmers, as well as to capture cell-cell and cell-fluid interactions, I use the SPR model introduced in **chapter 2** with tunable cell morphology, hydrodynamics, and steric interactions.

In the dilute state, swarming *S. marcescens* can be easily observed rafting and traveling through unoccupied spaces in these aligned groups (Figure 3.1a). I contrast the measured speeds of individual cells to speed measurements dense suspensions where optical flow methods are utilized. Bacteria speeds in dense swarms increase compared to swimmers, reaching mean speeds of $V_{mean} \approx 26.6 \ \mu m \cdot s^{-1}$.
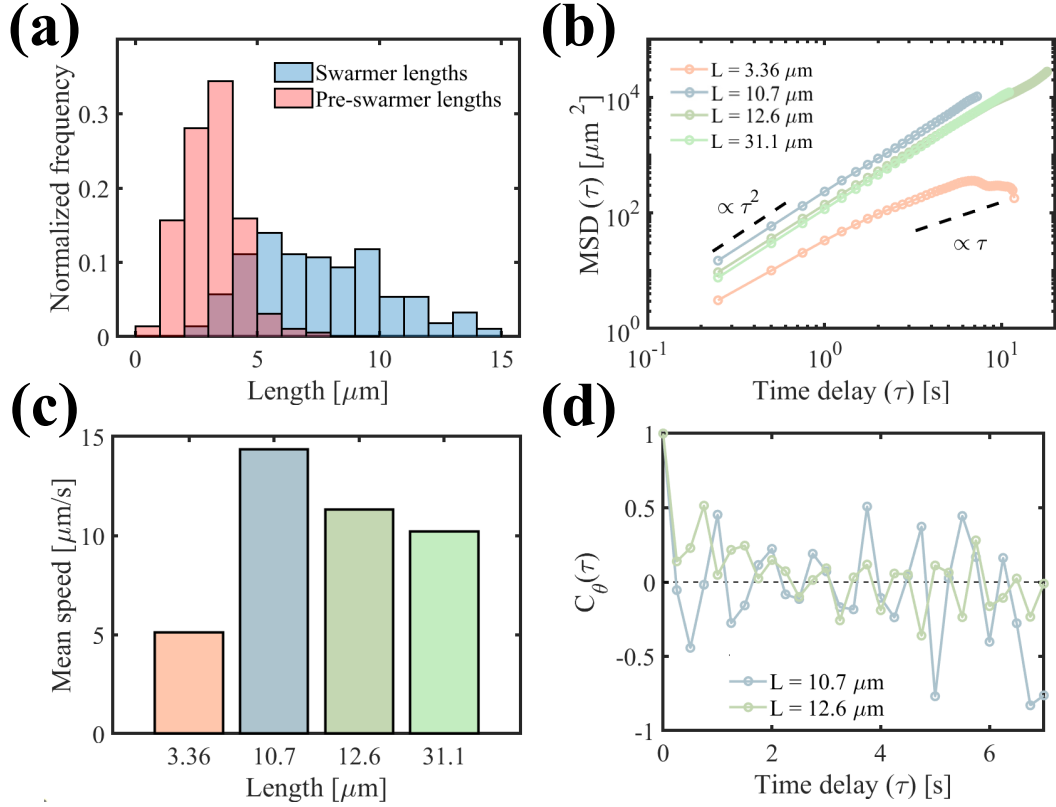
(a) **(b)** **(c)** **(d)**

Figure 3.2: Elongated swarming bacteria show increase in speeds compared to short bacteria with lengths comparable to swimmers. **(a)** Length distributions of measured bacteria lengths taken from two experiments and measured with ImageJ by drawing a straight line end-to-end for each visible and individually distinguishable bacteria. While planktonic bacteria typically have a length of 2-5 μm (Table 1.1), swarming bacteria elongate significantly, doubling or tripling their lengths. The mean length measured amongst N = 280 cells is $L_{mean} = 8.71$ μm. **(b)** Mean squared displacement of single tracked cells from diluted *S. marcescens* swarm. Longer cells (12.6 and 31.1 μm) appear to have more ballistic trajectories compared to shorter cells. Cells were manually tracked using ImageJ for at least 10 seconds and until they were no longer trackable. **(c)** Speeds of each bacterium from **a-d**. The bacterium that has a length (3.36 μm) close to the planktonic length move slower than elongated bacteria ($\geq 10.7\mu$m). Notably, the bacterium with a length of 10.7 μm moves faster than bacteria longer than that length. **(d)** Orientation correlation function for L = 10.7, 12.6 μm cells measured. Time where the function crosses zero is the approximate time, τ, for the cell to orient itself away from an initial orientation at $C_\theta(t)$. For L = 10.7 μm, $\tau \approx 0.25$s. For L = 12.6 μm, $\tau \approx 2.25$s.

Swarming bacteria exhibit a range of lengths typically ranging from 3-15 μm (Figure 3.2a). Here, I track and measure the speeds and MSDs of swarming bacteria spanning these typical lengths and additionally track an outlier length of $31.1\mu m$ (Figure 3.3). Generally, I find that for a cell length comparable to pre-swarming cells, the MSD and measured speeds are lower than elongated lengths. However, increases in length beyond 10.7 μm see slight decreases in MSD and speeds.

Through Particle Image Velocimetry analysis of dense swarms of *S. marcescens*, I confirm previous observations of bacteria increasing their speeds compared to planktonic bacteria [26] (Figure 3.2c). Furthermore, I utilized ImageJ to measure cell lengths in diluted swarms, confirming a wide length distribution amongst swarmers and increased mean length ($L_{mean} = 8.71\mu$m) with lengths reaching up to 31 μm (Figure 3.3d). I further assess from these dilute studies if individual bacteria speeds are dependent on their length. To observe individual
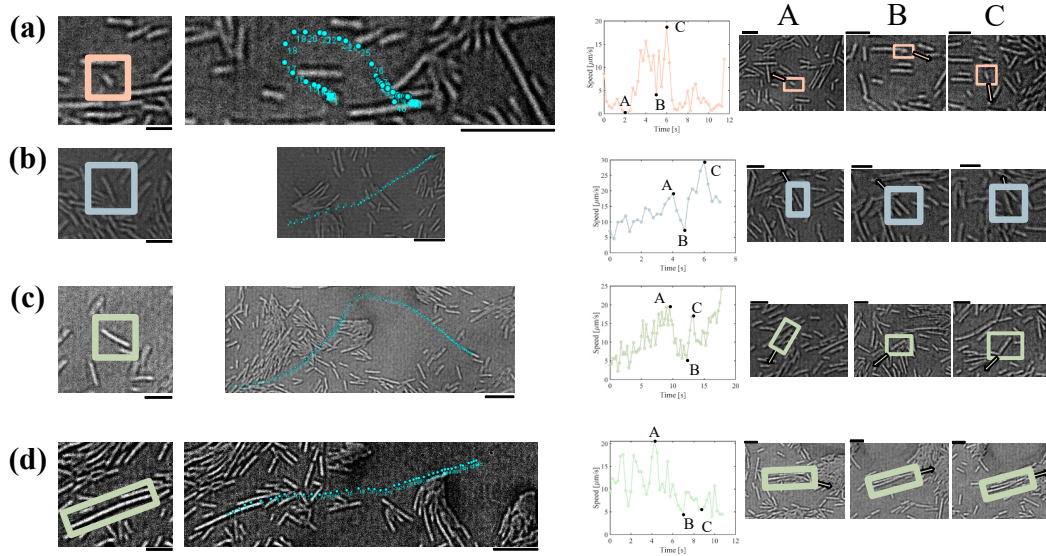
Figure 3.3: Swarming bacteria lengths and speeds increase compared to swimming bacteria. **(a-d)** Snapshots and tracks of *S. marcescens* bacteria with different lengths. Bacteria were manually tracked using ImageJ and marked at the center of the cell along their long axis. Time between each point is $\Delta t = 0.25s$. Scale bars for the bacteria snapshots are 10 μm and the scale bars for the tracks are 20 μm. Points A, B, C are points in time and are indicated by speed versus time plots. As expected, cells move slower they are moving into other cells or moving into groups of cells. Cells appear to move the fastest when their direction of motion is unimpeded, or in case of elongated cells (**c-d**), moving in a raft with other bacteria adjacent to the tracked bacterium. Scale bars in these snapshots are 10 μm.

cells, I diluted dense swarms with LB broth to better image and resolve their morphologies (See Methods). I calculated both the mean speed of 4 different bacteria lengths and their mean squared displacements (Figure 3.2(b, c)) finding that for bacterium longer than the mean planktonic length (Table 1.1), their motion is ballistic (MSD $\propto \tau^2$) for the observed time. Bacteria with lengths comparable to planktonic bacteria, are diffusive for longer delay times and are slower than longer bacteria. What is not clear from these observations alone are the effects of hydrodynamic and steric interactions between cells that may aid in their ability to cooperate and collectively move. To capture these features of bacteria swarmers, as well as to capture cell-cell and cell-fluid interactions, I use the SPR model with tunable cell morphology, hydrodynamics, and steric interactions.

3.3.2 Increased rod aspect ratio benefits motility and promotes clustering and cluster lifetime

In this study, I varied the rods lengths from $L = 3$, 5, 10 to study the effects of cell aspect ratio on swarming dynamics. L = 3 is comparable to single, swimming cells, while L = 5, 10 are comparable to elongated swarming bacteria. I maintain a density of $\Psi = 0.33$ to study how cells may interact with one another and form clusters. At higher densities, it becomes difficult to study cluster formation as there would be persistent cluster-cluster interactions. Trajectories and visualizations of rod lengths comparable to swarming bacteria at L = 5, 10 (Figure 3.4) show cluster formation and ballistic trajectories where the longer length of the rods promote less reorientation compared to L = 3. The enhanced motility of the rods is further supported by calculating the ensemble MSD (Figure 3.5(a)). Rods with lengths similar to the mean length of swarming bacteria (L = 5) show ballistic motility measured over small
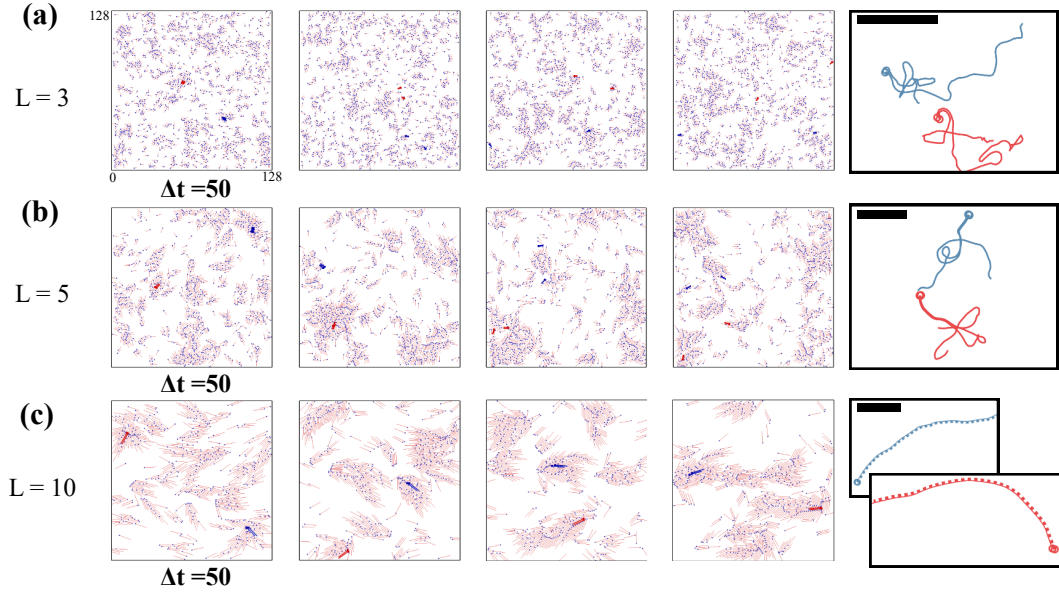
Figure 3.4: Snapshots of systems of rods with different lengths and snapshots of their positions and trajectories. Pairs of rods next to each other were selected for tracking. Large red and blue marks indicate pairs of rods adjacent to each other at the first timepoint in the figure. Their respective trajectories are taken over $t = 200$ (**a-c**). The time between each successive frame is $\Delta t = 50$ and the scale bars in each trajectory plot is 50λ. In (**c**), pairs are close together and made distinct with solid and dashed lines.

times, which at long times, they display diffusive behavior. For even longer rods (L = 10), the motion can be described as purely ballistic across all measured delay times. This is supported qualitatively by observing rod trajectories (Figure 3.4). For L = 10, the trajectories are ballistic, rods are aligned and moving alongside each other. Visualizing the rod dynamics over the course of the simulation revealed that as aspect ratio increases, so does the size Figure 3.6(a-c) and persistence time Figure 3.5(c, e) of the clusters. Rods with a length of 10 form large, aligned clusters compared to other lengths studied. At these long rod lengths, the initially small clusters eventually collide, creating larger clusters as a result. These larger clusters also persist for longer times as shown by the time it takes for $C_\theta(\tau) = 0$.

In figure 3.8(a,b), I plot the time ensemble averaged magnitude of vorticity and ensemble averaged pressure as functions of rod length. As the length of rods increases, so does the magnitude of vorticity. I note that while there are large fluctuations of the vorticity (as shown by the shaded error plots), the mean for all vorticies does not greatly vary across time. Unlike vorticity, the mean pressure fluctuates over time for all rod lengths and does not appear to vary between lengths as shown by the significant overlap between the curves.

To have a better understanding of the effect length has on the vorticity, I compliment figure 3.8(a,b) by providing snapshots of the vorticity field over time for each rod length. Looking at system plots of the vorticity in figure 3.7 as functions of length, I find that for the shortest system length, the size of vorticies appear smaller compared to the longest system length. For L = 10, the elongated rods are able to move together in larger clusters (figure 3.6) that increase the size of the apparent vorticity. This is to be expected as larger clusters are able to swirl and turn as one, increasing the local vorticity at the location of those clusters. Meanwhile, changes in rod length does not appear to significantly affect the size or magnitude of pressure in each of the respective systems (Figure 3.8(b)).

3.3.3 Inclusion of hydrodynamics promote clustering and meso-scale turbulence resembling bacteria swarms

Hydrodynamics have been previously shown to be vital in forming cohesive and persistent structures consisting of multiple active agents [27, 28, 29]. I confirm through the simulations, that hydrodynamics in swarm-like systems assist in forming cohesive and persistent aligned clusters that can move through free-space.

In this study, I vary the stresslet strength from $0.1 \leq \alpha_h \leq 160$ to capture effects near the dry limit for hydrodynamic interactions and regimes where hydrodynamics dominate over self-propulsion and steric interactions.

Low values of α_h decrease the stress on the fluid, allowing steric interactions to dominate. At $\alpha_h = 0.1$, I observe the largest clusters among the stresslet strengths used in this study (Figure 3.6(d-f)). While this may imply that dry systems cluster better compared wet systems, these clusters have very long lifetimes and are not as turbulent as higher stresslet strengths. Figure 3.5(d) shows that while the spatial velocity correlation function, C_V for $\alpha_h = 0.1$ decays, the velocities do not appear to un-correlate for the duration of the simulations. When $\alpha_h \gg 1$, the stress on the fluid is higher than lower values and the rods are pushed around by the flow in such a way that destabilizes rafting and clustering as shown in figure 3.5(b,d,f). However, looking at velocity correlation functions, there is a large decrease in lifetime from $\tau = 237s$ for $\alpha_h = 1$ to $\tau = 200s$ for $\alpha_h = 160$. Therefore, while high hydrodynamics may allow for some cell-cell interaction, the rods do not prefer to stay close or aligned with each other. In the dry limit ($\alpha_h = 0.1$), very large clusters can form (Figure 3.6(c,e,f)) and are stable.

Similar to the previous MSD analysis on the length of rods, I find that the rods at short time-scales are ballistic across the tested stresslet strengths, eventually becoming diffusive at long time-scales (Figure 3.5(b)). However, I also find that as I increase the stresslet strength, the MSD becomes increasingly diffusive at all time-scales. Furthermore, it appears that in the dry limit, the rods are more motile compared to higher values of α_h as seen by the higher magnitude of the MSD when compared. The variety in which rods can exhibit different lifetimes and sizes of clustering and motility leads us to the idea that while hydrodynamic inclusion is a powerful tool that can qualitatively and quantitatively match experimentally observed phenomena, careful tuning must be implemented in order to avoid erroneous or nonsensical results.

3.3.4 Two-particle MSD

In figure 3.9, I calculate the two-particle mean squared displacement (2P-MSD) of single pairs of rods within the L = 5, 10 systems at fixed stresslet strength and velocity ($\alpha_h = 1$, V = 1). Two-particle tracking has been previously utilized as a way to determine the bulk properties of a viscoelastic material based on tracking of tracers on length scales much smaller than the sample itself [30]. Single- or one-particle MSDs assume that the environment is homogeneous, isotropic, and incompressible such that the motion of a tracked particle will not be influenced by other tracked particles in the system. In other words, the 2P-MSD and signal-particle MSD are equivalent in these systems. However, swarming bacteria colonies are neither homogeneous or isotropic: they have heterogeneous length and the arrangement of the cells are non-isotropic, prompting the analysis of these systems with 2P-MSD. I look at two cases: 1) when the pair of rods start apart at the beginning of analysis (Figure 3.9a) and when they start together (Figure 3.9b). Diffusive behavior in 2P-MSD can be interpreted as the pair of rods staying close to one another, while ballistic behavior is indicative of the rods moving away from each other and separating further in the case where they begin apart. For rods that start apart, the 2P-MSD is diffusive at short times for L = 10 while becoming ballistic only for very long times. This indicates that the rods continue to stay away from each other. For L = 5, the 2P-MSD is ballistic for short and intermediate times, only becoming sub-diffusive at very long delay times, which indicates that the rods may have come close into a cluster only at very

long delay times. In contrast, when the pair of rods are tracked starting together, the 2P-MSD for L = 5 is only slightly super-diffusive as the rods slowly move away from one another. For L = 10, the motion is sub-diffusive for most delay times as the longer lengths allow the rods to maintain distance and stay in the same cluster for very long times.

3.3.5 Dense rod simulations

In the previous section, I utilized SPR simulations at dilute area fractions where cell-cell interactions and be easily resolved. However, in nature, bacteria swarms are highly dense populations where they can form multilayers extending into 3D. To better capture details of cluster-cluster interaction, I analyze dense simulations with $\Psi = 0.73$. In these dense simulations, I model one set of parameters: L = 5, $\alpha_h = 1$, and V = 1 to determine how this . The MSD of the dense suspension is similar to the dilute case. At short time delays, the motion of the rods are ballistic and at long time delays, the motion of the rods are diffusive (figure 3.10(b)). Unlike the dilute case, the temporal orientation autocorrelations remain loosely correlated (remaining close to, but not equal to zero) over long periods of time, $C_\theta(\tau = 455) = 0$ (figure 3.10(c)). For the velocity autocorrelation function, the time for the velocities to become uncorrelated is the same as the dilute system, $C_V(\tau = 272.5) = 0$ (figure 3.10(d)). For the orientation correlation function, the long, but weak correlation time indicates strong stability of clusters that consistently run into and merge with other clusters.

3.4 Discussion

Bacteria swarming species are capable of rapid surface translocation and while research has identified several key features of the cells (elongation, hyperflagellation, collective motion, etc.) [24, 31], the precise mechanisms to which these features affect swarming remain unclear. In this work, I explore how elongation, cell-cell interactions, and hydrodynamics affect swarming through an *in silico* tunable self-propelled rod model.

3.4.1 Rod Morphology

In these systems, I simulate homogeneous systems of dilute, self-propelled rods to study the role bacteria cell length has on the motility, cluster size, and cluster stability. The experimental work on studying *S. marcescens* swarms reiterates the wide range of observable cell lengths and cell speeds in swarms (Figure 3.3,3.1). While I do not explore cell-cell and cluster dynamics in live experiments on *S. marcescens*, other groups that have studied the effects of cell elongation on the motility of bacteria swarms suggest that higher cell aspect ratios confers increased motility and cluster stability in the swarm. Notably, groups have found that increased bacteria cell lengths have increased speeds [8, 25, 5] which would provide a benefit to the propagation of the swarming colony. In the simulations, I model all rods in each system studied with a uniform velocity set to the mean swarming speed of *S. marcescens* ($V = 1 \equiv 28\mu m \cdot s^{-1}$) [32], so there are no speed variations between individual agents and vary the length of rods in each system from L = 3, 5, and 10.

I find that longer rod lengths provide several benefits to swarming dynamics. Longer rods increase both motility of rods and correlation times (Figure 3.5). Analysis of the trajectories (Figure 3.4) and their respective mean squared displacements indicate that longer rods tend to stay close to one another for long periods of time. Elongated rods have a tendency to collide more often, reorienting themselves parallel to one another, and stick together via steric interactions, resulting in larger, persistent clusters and ballistic behavior consistent with the previous findings [27, 33, 34]. Short rods on the other hand, are subject to turbulent

flows caused by hydrodynamics. Consequently, short rods may be pushed around easily and reoriented randomly [8], and ultimately result in rods at the edge of a cluster to orient themselves away from its cluster. Clusters are consequentially smaller and less persistent, suggesting that elongation is an essential feature of swarming bacteria that enables their increased cooperation and motility. At higher densities of homogeneous systems of short rods, this effect may be less pronounced due to increased collisions and interactions between rods which can bound cells into a cluster.

In the model, rod density is dilute ($\Phi = 0.33$) and the rods are homogeneous in length for each length systematically studied. Naturally, swarms are dense and range in lengths, so how does length heterogeneity affect swarming dynamics? By systematically adjusting ratios of elongated mutants of *B. subtilis* and shorter, wild-type cells, Peled *et al.* find that elongated bacteria can act to enhance or reduce enhanced features of a swarm [34]. At low ratios of long-to-WT cells, short WT cells collide often with elongated cells, aligning themselves parallel into a cluster. This in turn, increases the mean speed of all cells. However, higher long-to-WT ratios decrease speeds, possibly due to increase rates of collision and jamming. Taking this into consideration with the results, this suggests that long cells aid in the formation of clusters, taking in cells of varying lengths that are typically shorter and remain in a cluster due to steric interactions. While I do not look at heterogeneous cell lengths, this prompts future work that studies how both variations in length and hydrodynamics have an effect on motility and clustering ability.

3.4.2 Rod Hydrodynamics

The role of hydrodynamics in active matter systems have been explored in various contexts, including studying vortex formation in particle suspensions and dynamics of microswimmers [35, 21, 29]. In active matter systems and bacteria swarms, assessing the effects of hydrodynamics and steric interactions on collective features is difficult due to coupled effects from both. The self-propelled rod model allows independent tuning of hydrodynamics to describe its role in the formation of clusters and vortices in bacterial swarming systems. However, delicate tuning of the stresslet strength is necessary to appropriately encapsulate the collective features described in literature and experiments.

I test large values of stresslet strengths ($\alpha_h = 10, 160$) as well as stresslet strengths close to the previously studied values that appear to form vorticies as seen in swarming species [29], $\alpha_h = 0.1, 0.25, 0.5, 1$, to determine the effects to collective behavior with small changes to stresslet strength. Large values stated here are considered large, due to heavy flows that greatly disturb the collective motion of the system, resembling active particles in low-viscosity systems.

Flagellated bacteria generate dipolar fluid flows through thrust produced by their flagella and cell body, which are defined in literature as "pusher" type hydrodynamic effects [36, 37, 6, 38, 29, 39]. Pushers move fluid away along their long-axis and draw in fluid centered at their short axis', which may be a contributing factor to the alignment of rod-shaped swarmers. In the dry limit of the system ($\alpha_h = 0.1$), cluster size appears to be significantly higher than $\alpha_h = 1$ (Figure 3.6). However, the persistence of these clusters are decreased (Figure 3.5). The large increase in cluster size at the dry limit may be due to steric interactions dominating over hydrodynamics: rods that move close together align due to steric interactions, but there may not be large enough hydrodynamic contributions from the pushers to hold the alignment between rods. Consequentially, this would lead to decreased persistence time of clusters as they can break away easily. With extremely high hydrodynamic contributions ($\alpha_h = 160$), persistence time is significantly reduced as rods may come close to one another, but are soon pushed away by the large hydrodynamic forces exerted (Figure 3.6). Recent models that incorporate hydrodynamic forces for spheroidal squirmers in semi-periodic conditions find similar results at the same packing fraction [40]. At low packing fractions ($\Phi \leq 0.33$), clusters form at small

hydrodynamic contributions, whereas only small clusters form at higher hydrodynamic values. I note that swarm systems are dense, with very high packing fractions and dynamics/features can differ from what can be interpreted from this work. At higher densities, there is possibility of motility induced phase separation (MIPS) where clusters tend to consist of agents moving with similar velocities [20, 41, 40]. The addition of hydrodynamics to these systems exacerbates this effect, with multiple, smaller phase separated clusters. This latter effect may be seen in live swarms, as there is a wide speed distribution amongst densely packed swarming cells. These MIPS clusters move independently, but the density forces interactions between clusters that lead to mesoscale turbulence and vortex formation observed in dense swarms [16, 40].

For many bacteria species, surfactants are produced in order to reduce the surface tension and aid in fluid-mediated surface swarming which are unaccounted for in most studies [42, 43, 44]. The addition of exogenous fluid to the system generated by these species, as well as reduced surface tension, may have significant effect on the hydrodynamic forces. What also has not been addressed in relation to hydrodynamic forces and surfactants is that certain species of surfactant producing swarmers form multi-layer colonies [45, 6]. At the upper surface of these swarming colonies, there is increased diffusivity as a result, which aids in material collection and transport. While I do not explicitly explore these effects in this work, the model is capable of tuning the viscosity of the simulated fluid to replicate the effect of surface-tension reducing surfactants. This would warrant additional studies of these factors with the aim of a holistic interpretation of the different factors that affect swarming.

While the dilute simulations can capture cell-cell interactions and cluster formation, swarms are dense suspensions where multiple clusters interact with one another. I extend the scope of the simulations by modeling rods in a dense system ($\Psi = 0.73$). Unsurprisingly, the temporal correlation functions, $C_\theta(\tau)$ and $C_V(\tau)$, decay at slower rates compared to the dilute case due to to the increased rate of rod interactions. In dilute suspensions, cell reorientation is made easier by reduced frequency of steric interactions, allowing cells to reorient and move away from an aligned cluster. This results is the shorter correlation times calculated previously (Figure 3.5). For dense suspensions where cells are tightly packed, cells cannot easily move away from the general direction of cluster due to the high degree of steric interactions and proximity to other cells. Therefore, velocities and orientations can remain loosely correlated for longer periods of time.

3.4.3 Phenotype effects on motility and collective features

Collective behaviors are ubiquitous in nature, commonly found in social animals such as flocks of birds or fish and in colonies of microorganisms. These large scale dynamics that may consist of hundreds of agents, are brought upon by local interactions and alignment amongst individuals within a relatively short proximity of only several body-lengths away. Such behavior acting on a large scale is key to foraging and territory acquisition, leading to the prolonged survival of the group.

In Mexican tetra fish, *A. mexicanus*, distinct collective behaviors emerge depending on age of development and whether the groups of fish reside near the surface of open water, or inside cave systems [46]. At later stages of development, around the sub-adult stage, groups of surface fish modulate their swimming and turning speeds in order to remain closer in proximity to their nearest neighbors, while cavefish at similar development stages do not exhibit any form of collective behavior. Similar behavior can be exhibited in the clustering ability of swarming versus swimming bacteria. Morphological differences aside, swimming bacteria move individually and possess no preference for proximity or alignment with nearest neighbors. The homogeneous system of SPRs with short lengths comparable to swimming bacteria display similar dynamics to cavefish: these shorter length rods tend to scatter and have shorter cluster lifetimes compared to longer rods (Figure 3.4, 3.6) which can be compared to the lack of schooling/shoaling amongst cavefish.

In addition to swarming, other types of bacteria motility exhibit collective motion and large scale features. Gliding *Oscillatoria lutea* for example, a strain of filamentous cyanobacteria spanning up to 1500 μm in length, transition from being isotropicly spaced and oriented at low densities, to bundling together beyond a critical density forming order states of aligned filaments and distinct patterning at length scales larger than individual filaments [47]. Furthermore, this ordering a large densities typically occur for a filament interacting with another at a small angles of attack. This behavior is seen similarly in swarming cells, where low densities can form short-range order at scales of only a few bacteria cell lengths (Fig 3.1(a)), but higher densities form vortexes that can span 20 μm in diameter for a single vortex [32, 48].

However, compared to fish, swarming bacteria possess no innate knowledge or instincts that promote beneficial collective behavior. So then, what factors may contribute to promoted clustering and collective motion of swarming bacteria? The results suggest that length plays a critical role in cluster formation. Long cells naturally encounter more cells due to their length, meanwhile steric and hydrodynamic interactions are able to maintain proximity and alignment for these longer cells. In contrast, swimming bacteria are shorter and possess less flagella. The latter difference may also play an important role in the rafting ability of swarming cells. Swimming bacteria undergo run-and-tumble motion, where the cell randomly reorients (tumbles) at a frequency of approximately 1 Hz and is caused by sudden counter-rotation of flagella [3] while swarming bacteria suppress tumbling [49]. While this has the direct result of increasing swarming speeds, the reduction in tumbling rate may benefit clustering as cells at the periphery of a cluster may find it more difficult to reorient themselves away from the group if they cannot tumble.

Swarming bacteria are highly active systems that form ordered microdomains similar to nematic liquid crystals [19, 50]. In these systems, defects are able to form and comparisons can be drawn to elucidate the role of alignement and defect formation in these highly active systems. Within these bacteria colonies are motile, topological +1/2 and -1/2 point defects, similar to non-equilibrium nematic systems. These topological defects are hypothesized to aid in the expansion of an initially 2D colony into multi-layer, 3D colonies. This growth in dimension aids in continued proliferation of the colony, transition from swarming to biofilms, and protection from exogenous factors that can harm the its development, such as antibiotics [31, 51]. Initially, an inoculated colony of rod-shaped bacteria begins as a single layer of cells. As the colony continues to grow and the density increases, the rod-shaped cells begin to locally align and cluster together. Interactions between local clusters generate topological +1/2 and -1/2 point defects [52, 19]. Collision of two +1/2 defects can create a +1 defect and can cause vertical orientation of these cells therefore creating an upward protrusion of cells to create a second layer. The 2D SPR system, while does not extend into 3D, could potentially be utilized to study growing bacteria colonies in the context of active nematic systems. These nematic structures and their defects can drive three dimensional growth of bacterial colonies. -1/2 defects in rod-like/filamentous systems are subdiffusive, due to collisions between rods when oriented in such a manner. Similar to the system, rods moving in opposite directions or are oriented anti-parallel can become jammed or have their movement temporally impeded. However, the dilute density of the system allows reorientation away from other rods, restoring their mobility. As clusters begin to form, the rods are aligned parallel to one another, orienting themselves in similar directions. The simulations can be readily expanded into dense systems resembling these studies where these point defects are abundant enough that they readily interact with one other. Similar systematic studies of aspect ratio and hydrodynamics can be conducted in order to asses their roles in the formation and dynamics of these defects, and how they may contribute positively or negatively to the collective features of bacterial colonies.

3.5   Conclusions

My study of in-silico, dilute suspensions of self-propelling dipolar rods enables analysis of cell-cell interactions that are difficult to elucidate in dense swarming suspensions where large collectives of cells interact. Aspect ratio plays a crucial role in cluster formation of rod-shaped agents, implying that rod-like, flagellated swarming bacteria obtain some of their fast-moving qualities and collective features due the elongation of bacteria when initiating the swarming phase. Hydrodynamic interactions also appear to benefit cluster formation and cluster persistence with assumed interactions, but appropriate tuning is required to capture as many qualitative swarm features as possible. In the dilute limit, the analysis is limited to only these cell-cell interactions and mesoscale vorticies typically formed in denser systems are not observable. Therefore, I complimented the analysis of dilute systems by analyzing a dense system that captures the aforementioned vorticies and cluster-cluster interactions. Overall, these cell-cell interactions are key to understanding what collective features emerge and the mechanisms which form these in dense systems.

The homogeneous systems of study are inclusive of conditions and parameters in naturally occurring swarms: wide length variation, varying speeds, chemotaxis, etc. The results that found through the model and experimental observations support the hypothesis that elongation in bacteria swarming species is key to their enhanced motility and ability to perform collective motion. Hydrodynamics are shown here to be effective in not only aiding in the formation of clusters and collective features, but also introducing active mixing into the system which facilitates rapid transport seen in dense swarming suspensions. Future research regarding bacteria swarms may involve studies on systems consisting of a range of lengths as opposed to fixed length systems. The fraction of high aspect ratio swarming cells to lower aspect ratio cells determines whether swarming motility and clustering ability benefits or is suppressed, prompting the necessity to study heterogeneous systems of rod aspect ratios further [34]. The work also does not simulate the rods in three-dimensions, which are more typical of entire swarming colonies, but can capture features observed in monolayers and monolayer regions of swarms [53, 54]. Other future work involving the self-propelled rod model can be used to study heterogeneous systems with two sets of aspect ratio to determine how much of an effect length variation plays into swarming features and collective motion. Furthermore, this work can be generalized to study active nematic systems such as liquid crystals that resemble swarm-like structures and other active matter systems.
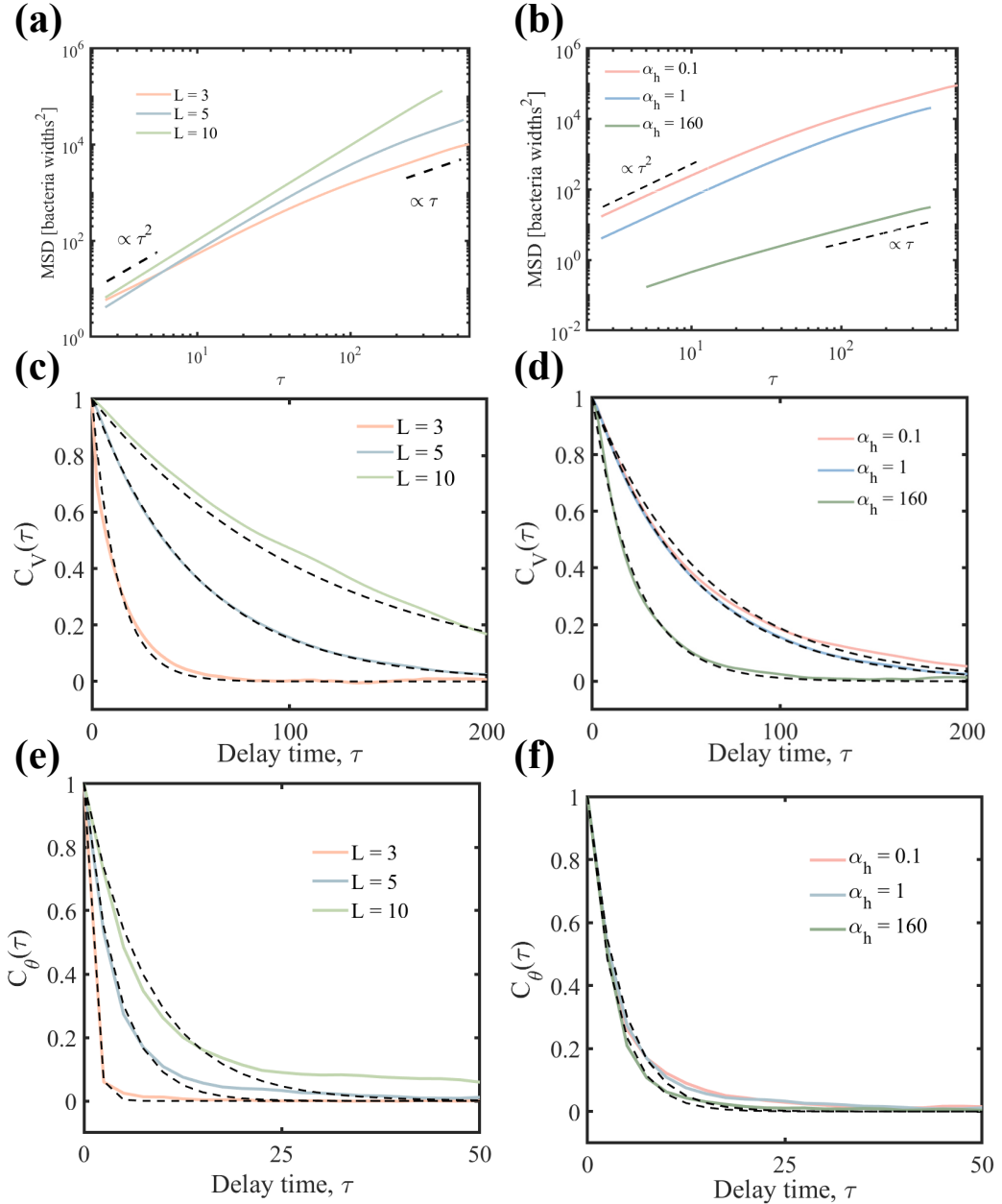
Figure 3.5: Increasing rod stresslet strength decreases cluster persistence and rod motility. **(a)** Mean squared displacement for varying aspect ratios of self-propelled rods. **(b)** Mean squared displacement of rods with varying stresslet strength, α_h. For early delay times (τ) and for stresslet strengths ≤ 1, the rod motion is ballistic ($\langle r^2(\tau) \rangle \propto \tau^2$). For longer delay times, the rod motion is diffusive ($\langle r^2(\tau) \rangle \propto \tau$). **(c)** Temporal velocity autocorrelation function for various rod lengths, L. Dashed lines are exponential fits to the correlation functions and are as follows: For $L = 3$, $\tau = 12$, $L = 5$, $\tau = 55$, and $L = 10$, $\tau = 108$. **(d)** Temporal velocity autocorrelation function for various stresslet strengths, α_h. Dashed lines are exponential fits to the correlation functions and are as follows: For $\alpha_h = 0.1$, $\tau = 59$, $\alpha_h = 1$, $\tau = 55$, and $\alpha_h = 160$, $\tau = 25$. **(e)** Orientation autocorrelations as functions of rod length. Dashed lines are exponential fits to the correlation functions and are as follows: For $L = 3$, $\tau = 12$, $L = 5$, $\tau = 55$, and $L = 10$, $\tau = 108$. **(f)** Orientation autocorrelations as functions of stresslet strength, α_h. Dashed lines are exponential fits to the correlation functions and are as follows: For $\alpha_h = 0.1$, $\tau = 4$, $\alpha_h = 1$, $\tau = 4$, and $\alpha_h = 160$, $\tau = 3.5$.
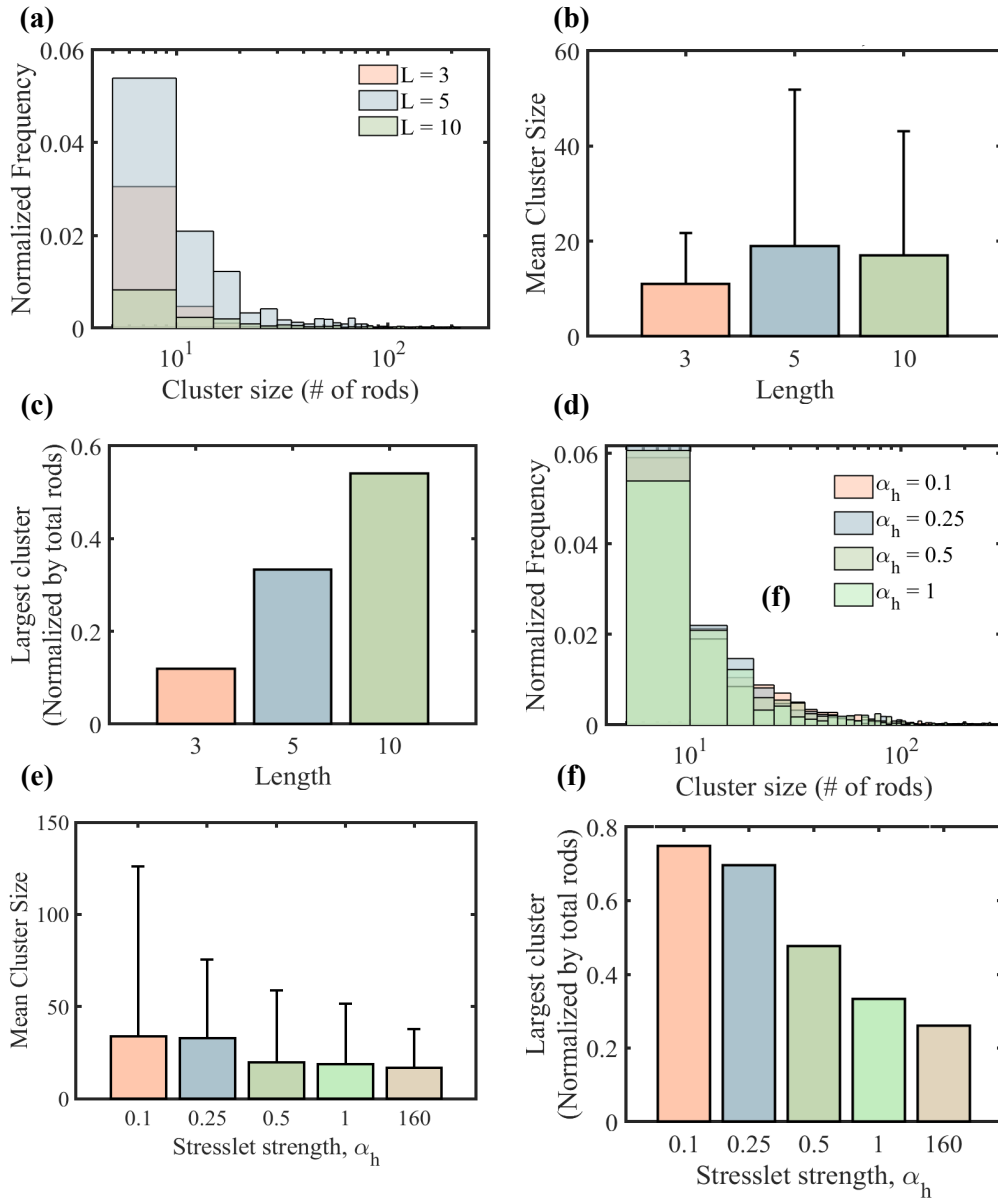
Figure 3.6: Statistics of cluster sizes of rods as a function of length **(a-c)** and stresslet strength, α_h **(d-f)**. Histograms bins in **(a)** and **(d)** are 5 rods and taken over a time frame of $\Delta t = 100s$. **(a)** Histogram of cluster sizes for rods of different lengths. Short rods (L = 3) typically do not exceed cluster sizes beyond 20 rods in single cluster and is evident in the mean cluster size in **(b)**. **(b)** Bar chart showing mean cluster sizes for each rod length. Error bars are 1 standard deviation. Cluster sizes were calculated by determining the number of rods are connected to each other (see Methods). **(c)** Bar chart of maximum cluster sizes observed (normalized by the total number rods for each system) for each rod length. The maximum cluster size increases with rod length. For each length, the total number of rods in the max observed cluster size is 143, 300, 265 rods for L = 3, 5, 10, respectively. **(d)** Histogram of cluster sizes for rods of different stresslet strengths. **(e)** Mean cluster size across the three different stresslet strengths. The "dry" limit is where there are minimal hydrodynamic effects ($\alpha_h = 0.1$). **(f)** Bar chart of maximum cluster sizes observed (normalized by the total number rods for each system, maintaining $\Phi = 0.33$) for each value of α_h tested. The total number of rods in **(f)** for each value of α_h corresponds to 697, 513, 429, 300, 234 rods for $\alpha_h = 0.1, 0.25, 0.5, 1, 160$.

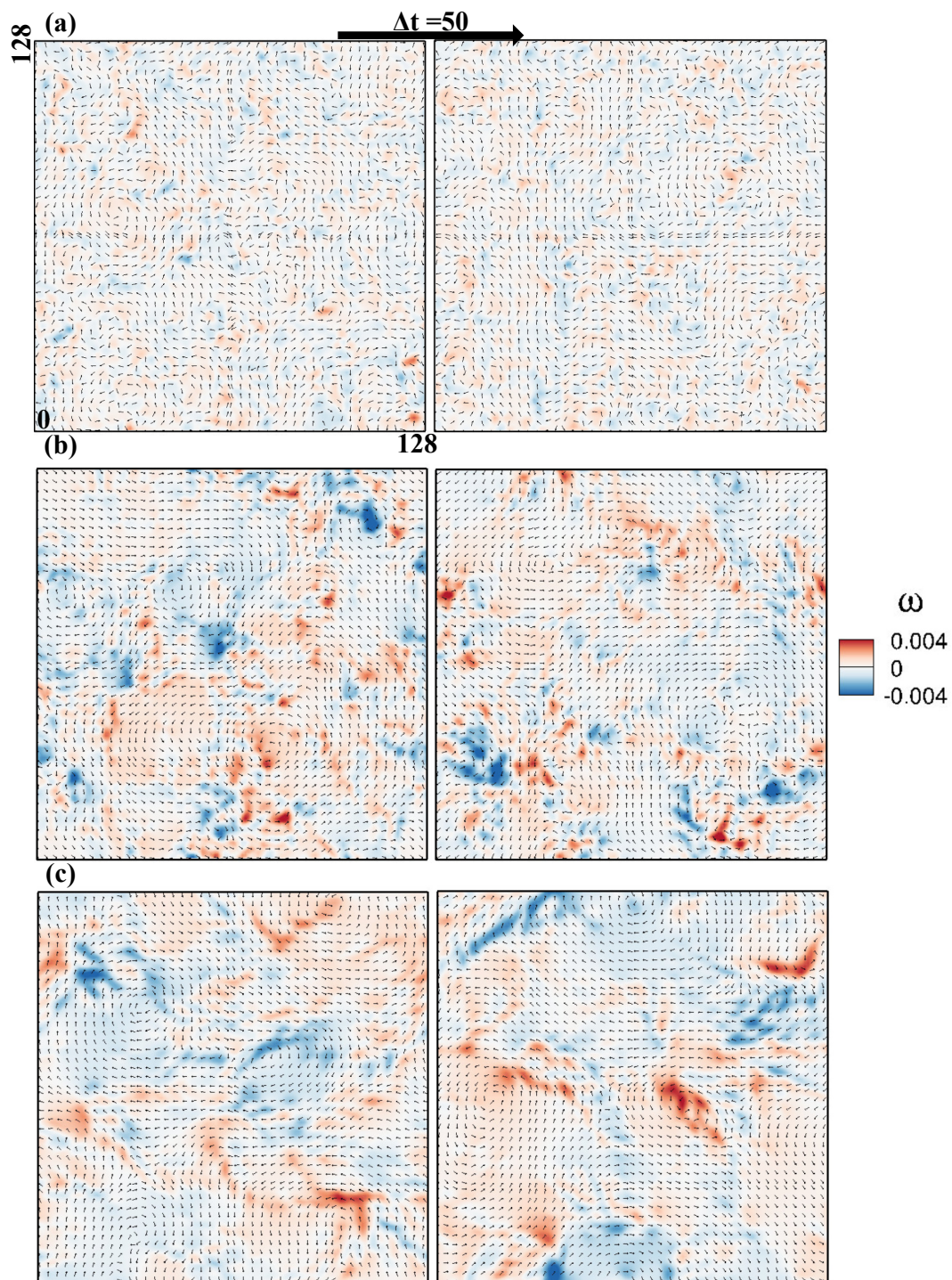Figure 3.7: Vorticity plots over time for three different rod lengths: **(a)** L = 3. **(b)** L = 5. **(c)** L = 10. In each system, $\alpha_h = 1$, $V = 1$, and snapshots are separated by 50 simulated seconds. The domains in each snapshot are 128x128λ.
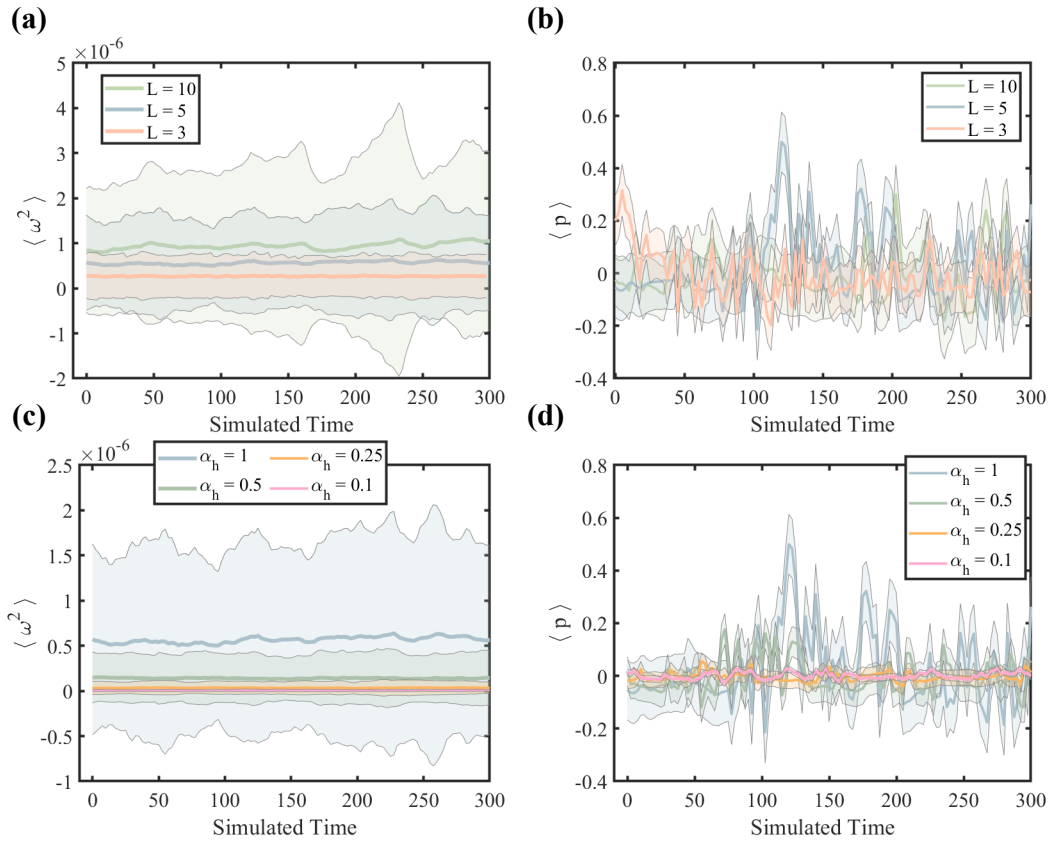
Figure 3.8: Time evolution of the spatial mean magnitude of vorticity **(a,c)**, $\langle \omega^2 \rangle$, and pressure **(b,d)** mean pressure $\langle p \rangle$ for simulations with different rod lengths and stresslet strengths. α_h = 160 is excluded for readability reasons due to the large magnitude generated, relative to the other values. Shaded areas are 1 standard deviation.

Figure 3.9: Two particle MSD (2P-MSD) given by Eqn. 3.8 shown for rods L = 5, 10 for when rods start apart **(a)** and when rods start together **(b)**. At short delay times for when paired rods start apart, the 2P-MSD for L = 5 rods are diffusive while for L = 10, the 2P-MSD is ballistic. Similar is seen for L = 5 rods when the paired rods start together.

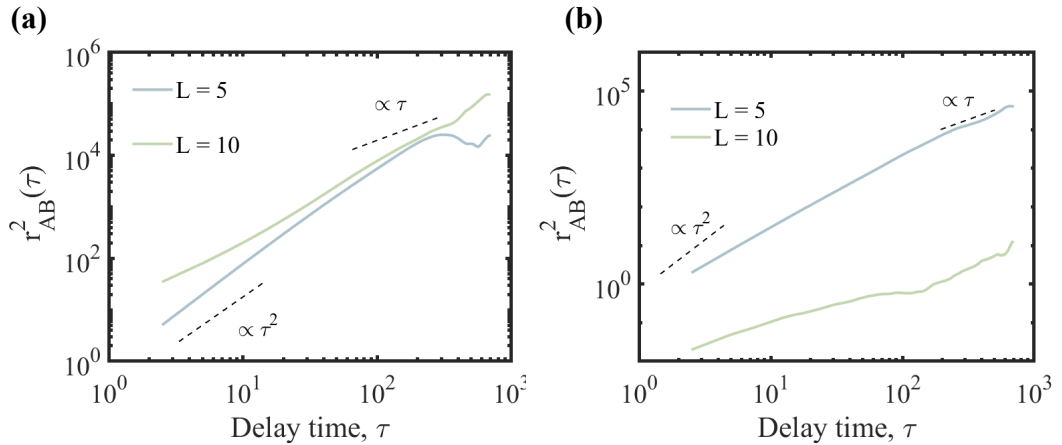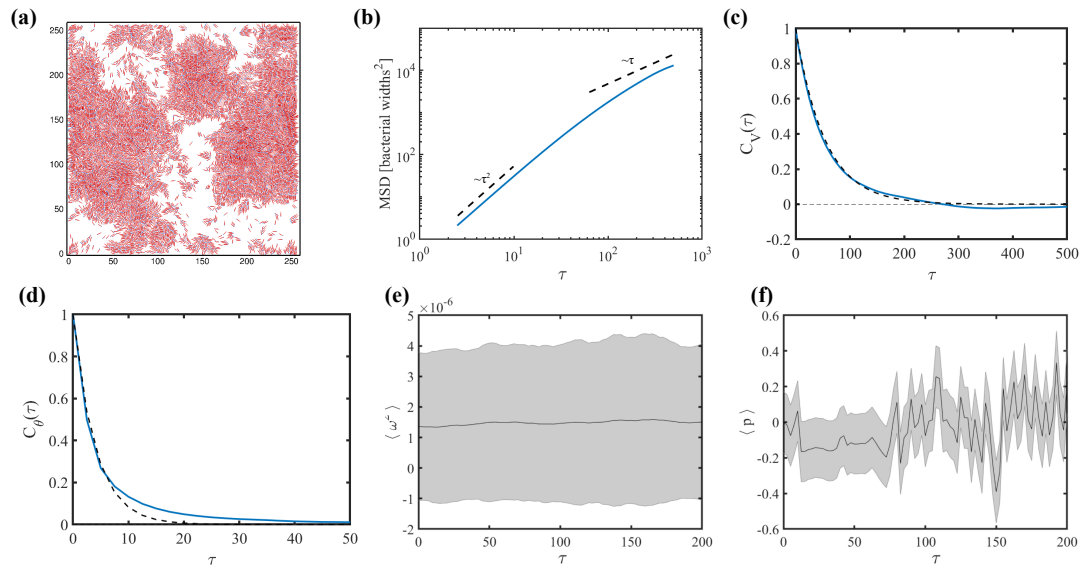Figure 3.10: Statistics on dense system of rods. In the data presented, $L = 5$, $\alpha_h = 1$, $V = 1$, $\Psi \approx 0.82$ with 8000 rods in the system. To accommodate this many rods, the domain was increased to $(256 \times 256)\lambda$. **(a)** Snap of a simulation with the dense system of rods. Rods have high degrees of interaction with each other, much like bacteria in dense swarms. **(b)** Ensemble MSD of the dense system. Similar to the dilute case, the MSD shows that the rods motion is ballistic for at short times while over long times the motion is diffusive. **(c)** Velocity correlation function, C_V, shows that the velocities are loosely correlated for long delay times. Fit shows a correlation time of $\tau = 54$. **(d)** Orientation correlation function, C_θ shows that the orientations are loosely correlated for long delay times. Fit shows a correlation time of $\tau = 4$. **(e)** Mean vorticity magnitude, as a function of time. **(f)** Mean pressure as a function of time.

Bibliography

[1] L. Alberti and R. M. Harshey, "Differentiation of Serratia marcescens 274 into swimmer and swarmer cells.," *Journal of Bacteriology*, vol. 172, no. 8, pp. 4322–4328, 1990.

[2] R. C. Maloney and C. K. Hall, "Clustering and Phase Separation in Mixtures of Dipolar and Active Particles in an External Field," *Langmuir*, vol. 36, no. 23, pp. 6378–6387, 2020.

[3] R. M. Harshey, "Bacterial motility on a surface: Many ways to a common goal," *Annual Review of Microbiology*, vol. 57, no. 1, p. 249–273, 2003.

[4] M. T. Butler, Q. Wang, and R. M. Harshey, "Cell density and mobility protect swarming bacteria against antibiotics," *Proceedings of the National Academy of Sciences*, vol. 107, no. 8, pp. 3776–3781, 2010.

[5] P. Bera, A. Wasim, J. Mondal, and P. Ghosh, "Mechanistic underpinning of cell aspect ratio-dependent emergent collective motions in swarming bacteria," *Soft Matter*, vol. 17, no. 31, pp. 7322–7331, 2021.

[6] N. C. Darnton, L. Turner, S. Rojevsky, and H. C. Berg, "Dynamics of bacterial swarming.," *Biophysical journal*, vol. 98, no. 10, pp. 2082–90, 2010.

[7] A. Be'er, B. Ilkanaiv, R. Gross, D. B. Kearns, S. Heidenreich, M. Bär, and G. Ariel, "A phase diagram for bacterial swarming," *Communications Physics*, vol. 3, no. 1, p. 66, 2020.

[8] B. Ilkanaiv, D. B. Kearns, G. Ariel, and A. Be'er, "Effect of Cell Aspect Ratio on Swarming Bacteria," *Physical Review Letters*, vol. 118, no. 15, p. 158002, 2017.

[9] H. Berg, *Random Walks in Biology*. Princeton paperbacks, Princeton University Press, 1993.

[10] L. Caprini and U. M. B. Marconi, "Spatial velocity correlations in inertial systems of active Brownian particles," *Soft Matter*, vol. 17, no. 15, pp. 4109–4121, 2021.

[11] T. Vicsek, A. Czirók, E. Ben-Jacob, I. Cohen, and O. Shochet, "Novel type of phase transition in a system of self-driven particles," *Phys. Rev. Lett.*, vol. 75, pp. 1226–1229, Aug 1995.

[12] G. Volpe, S. Gigan, and G. Volpe, "Simulation of the active Brownian motion of a microswimmer," *American Journal of Physics*, vol. 82, no. 7, pp. 659–664, 2014.

[13] G. Gompper, R. G. Winkler, T. Speck, A. Solon, C. Nardini, F. Peruani, H. Lwen, R. Golestanian, U. B. Kaupp, L. Alvarez, T. Kirboe, E. Lauga, W. C. K. Poon, A. DeSimone, S. Muios-Landin, A. Fischer, N. A. Sker, F. Cichos, R. Kapral, P. Gaspard, M. Ripoll, F. Sagues, A. Doostmohammadi, J. M. Yeomans, I. S. Aranson, C. Bechinger, H. Stark, C. K. Hemelrijk, F. J. Nedelec, T. Sarkar, T. Aryaksama, M. Lacroix, G. Duclos, V. Yashunsky, P. Silberzan, M. Arroyo, and S. Kale, "The 2020 motile active matter roadmap," *Journal of Physics: Condensed Matter*, vol. 32, no. 19, p. 193001, 2020.

[14] S. Bose, K. Dasbiswas, and A. Gopinath, "Matrix stiffness modulates mechanical interactions and promotes contact between motile cells," *Biomedicines*, vol. 9, no. 4, p. 428, 2021.

[15] S. Bose, P. S. Noerr, A. Gopinathan, A. Gopinath, and K. Dasbiswas, "Collective states of active particles with elastic dipolar interactions," *Frontiers in Physics*, vol. 10, p. 876126, 2022.

[16] R. Großmann, P. Romanczuk, M. Bär, and L. Schimansky-Geier, "Vortex Arrays and Mesoscale Turbulence of Self-Propelled Particles," *Physical Review Letters*, vol. 113, no. 25, p. 258104, 2014.

[17] W. Zuo and Y. Wu, "Dynamic motility selection drives population segregation in a bacterial swarm," *Proceedings of the National Academy of Sciences*, vol. 117, no. 9, pp. 4693–4700, 2020.

[18] M. Bär, R. Großmann, S. Heidenreich, and F. Peruani, "Self-Propelled Rods: Insights and Perspectives for Active Matter," *Annual Review of Condensed Matter Physics*, vol. 11, no. 1, pp. 1–26, 2019.

[19] O. J. Meacock, A. Doostmohammadi, K. R. Foster, J. M. Yeomans, and W. M. Durham, "Bacteria solve the problem of crowding by moving slowly," *Nature Physics*, vol. 17, no. 2, pp. 205–210, 2021.

[20] M. Theers, E. Westphal, K. Qi, R. G. Winkler, and G. Gompper, "Clustering of microswimmers: interplay of shape and hydrodynamics," *Soft Matter*, vol. 14, no. 42, pp. 8590–8603, 2018.

[21] F. Ginelli, F. Peruani, M. Bär, and H. Chaté, "Large-Scale Collective Properties of Self-Propelled Rods," *Physical Review Letters*, vol. 104, no. 18, p. 184502, 2010.

[22] J. E. Sosa-Hernández, M. Santillán, and J. Santana-Solano, "Motility of Escherichia coli in a quasi-two-dimensional porous medium," *Physical Review E*, vol. 95, no. 3, p. 032404, 2017.

[23] W. Thielicke and R. Sonntag, "Particle image velocimetry for MATLAB: Accuracy and enhanced algorithms in PIVlab," *Journal of Open Research Software*, vol. 9, 2021.

[24] D. B. Kearns, "A field guide to bacterial swarming motility," *Nature Reviews Microbiology*, vol. 8, no. 9, p. 634–644, 2010.

[25] A. Be'er and G. Ariel, "A statistical physics view of swarming bacteria," *Movement Ecology*, vol. 7, no. 1, p. 9, 2019.

[26] A. E. Patteson, A. Gopinath, P. K. Purohit, and P. E. Arratia, "Particle diffusion in active fluids is non-monotonic in size," *Soft Matter*, vol. 12, pp. 2365–2372, 2016.

[27] F. Peruani, A. Deutsch, and M. Bär, "Nonequilibrium clustering of self-propelled rods," *Physical Review E*, vol. 74, no. 3, p. 030904, 2006.

[28] H. H. Wensink, J. Dunkel, S. Heidenreich, K. Drescher, R. E. Goldstein, H. Löwen, and J. M. Yeomans, "Meso-scale turbulence in living fluids," *Proceedings of the National Academy of Sciences*, vol. 109, no. 36, pp. 14308–14313, 2012.

[29] E. Lushi, H. Wioland, and R. E. Goldstein, "Fluid flows created by swimming bacteria drive self-organization in confined suspensions," *Proceedings of the National Academy of Sciences*, vol. 111, no. 27, pp. 9733–9738, 2014.

[30] J. C. Crocker and B. D. Hoffman, "Multiple-particle tracking and two-point microrheology in cells," *Methods in Cell Biology*, vol. 83, p. 141–178, 2007.

[31] I. Grobas, M. Polin, and M. Asally, "Swarming bacteria undergo localized dynamic phase transition to form stress-induced biofilms," *eLife*, vol. 10, p. e62632, 2021.

[32] A. E. Patteson, A. Gopinath, and P. E. Arratia, "The propagation of active-passive interfaces in bacterial swarms," *Nature Communications*, vol. 9, no. 1, p. 5373, 2018.

[33] S. Weitz, A. Deutsch, and F. Peruani, "Self-propelled rods exhibit a phase-separated state characterized by the presence of active stresses and the ejection of polar clusters," *Physical Review E*, vol. 92, no. 1, p. 012322, 2015.

[34] S. Peled, S. D. Ryan, S. Heidenreich, M. Bär, G. Ariel, and A. Be'er, "Heterogeneous bacterial swarms with mixed lengths," *Physical Review E*, vol. 103, no. 3, p. 032413, 2021.

[35] H. Merlitz, H. D. Vuijk, J. Brader, A. Sharma, and J.-U. Sommer, "Linear response approach to active Brownian particles in time-varying activity fields," *The Journal of Chemical Physics*, vol. 148, no. 19, p. 194116, 2018.

[36] J. P. Hernandez-Ortiz, C. G. Stoltz, and M. D. Graham, "Transport and collective dynamics in suspensions of confined swimming particles," *Physical Review Letters*, vol. 95, p. 204501, 2005.

[37] A. Baskaran and M. C. Marchetti, "Statistical mechanics and hydrodynamics of bacterial suspensions," *Proceedings of the National Academy of Sciences*, vol. 106, no. 37, p. 15567–15572, 2009.

[38] K. Drescher, R. E. Goldstein, N. Michel, M. Polin, and I. Tuval, "Direct measurement of the flow field around swimming microorganisms," *Phys. Rev. Lett.*, vol. 105, p. 168101, Oct 2010.

[39] S. D. Ryan, G. Ariel, and A. Be'er, "Anomalous fluctuations in the orientation and velocity of swarming bacteria," *Biophysical Journal*, vol. 111, no. 1, p. 247–255, 2016.

[40] K. Qi, E. Westphal, G. Gompper, and R. G. Winkler, "Emergence of active turbulence in microswimmer suspensions due to active hydrodynamic stress and volume exclusion," *Communications Physics*, vol. 5, no. 1, p. 49, 2022.

[41] J. Blaschke, M. Maurer, K. Menon, A. Zöttl, and H. Stark, "Phase separation and coexistence of hydrodynamically interacting microswimmers," *Soft Matter*, vol. 12, no. 48, p. 9821–9831, 2016.

[42] J. Q. Yang, J. E. Sanfilippo, N. Abbasi, Z. Gitai, B. L. Bassler, and H. A. Stone, "Evidence for biosurfactant-induced flow in corners and bacterial spreading in unsaturated porous media," *Proceedings of the National Academy of Sciences*, vol. 118, no. 38, p. e2111060118, 2021.

[43] Y. Wu, B. G. Hosu, and H. C. Berg, "Microbubbles reveal chiral fluid flows in bacterial swarms," *Proceedings of the National Academy of Sciences*, vol. 108, no. 10, pp. 4147–4151, 2011.

[44] A. Yang, W. S. Tang, T. Si, and J. X. Tang, "Influence of Physical Effects on the Swarming Motility of Pseudomonas aeruginosa," *Biophysical Journal*, vol. 112, no. 7, pp. 1462–1471, 2017. This paper is of interest because it tells us different factors of the substrate that affect swarming.

[45] A. Be'er and R. M. Harshey, "Collective Motion of Surfactant-Producing Bacteria Imparts Superdiffusivity to Their Upper Surface," *Biophysical Journal*, vol. 101, no. 5, pp. 1017–1024, 2011.

[46] A. Paz, K. J. Holt, A. Clarke, A. Aviles, B. Abraham, A. C. Keene, E. R. Duboué, Y. Fily, and J. E. Kowalko, "Changes in local interaction rules during ontogeny underlie the evolution of collective behavior," *bioRxiv*, p. 2023.03.28.534467, 2023.

[47] M. K. Faluweki, J. Cammann, M. G. Mazza, and L. Goehring, "Active spaghetti: Collective organization in cyanobacteria," *arXiv*, 2023.

[48] J. Yang, P. E. Arratia, A. E. Patteson, and A. Gopinath, "Quenching active swarms: effects of light exposure on collective motility in swarming Serratia marcescens," *Journal of The Royal Society Interface*, vol. 16, no. 156, p. 20180960, 2019.

[49] J. D. Partridge, N. T. Q. Nhu, Y. S. Dufour, and R. M. Harshey, "Tumble Suppression Is a Conserved Feature of Swarming Motility," *mBio*, vol. 11, no. 3, 2020.

[50] G. A. Vliegenthart, A. Ravichandran, M. Ripoll, T. Auth, and G. Gompper, "Filamentous active matter: Band formation, bending, buckling, and defects," *Science Advances*, vol. 6, no. 30, p. eaaw9975, 2020.

[51] J. D. Partridge, G. Ariel, O. Schvartz, R. M. Harshey, and A. Be'er, "The 3D architecture of a bacterial swarm has implications for antibiotic tolerance," *Scientific Reports*, vol. 8, no. 1, p. 15823, 2018.

[52] D. Dell'Arciprete, M. L. Blow, A. T. Brown, F. D. C. Farrell, J. S. Lintuvuori, A. F. McVey, D. Marenduzzo, and W. C. K. Poon, "A growing bacterial colony in two dimensions as an active nematic," *Nature Communications*, vol. 9, no. 1, p. 4190, 2018.

[53] W. Chen, N. Mani, H. Karani, H. Li, S. Mani, and J. X. Tang, "Confinement discerns swarmers from planktonic bacteria," *eLife*, vol. 10, p. e64176, 2021.

[54] Y. Liu, B. Li, and X.-Q. Feng, "Buckling of growing bacterial chains," *Journal of the Mechanics and Physics of Solids*, vol. 145, p. 104146, 2020.

Chapter 4

A methodology to study the pre-swarming phase and swarm mechanical properties

4.1 Introduction

The results presented in section 4.2 are a reprint in part of Kumar et al. [1]. In this chapter, I describe not very well understood regimes of swarming colonies: the pre-swarming/lag period and the mechanical properties of the swarm. I present methodologies to both track tracer particles within a swarm to assess the mechanical properties of a swarm and a methodology to study the pre-swarming/lag period.

4.1.1 Limited research in the pre-swarming lag time in swarming colonies

Most research on swarming colonies and species only do so once the colony has begun to swarm in order to capture movement, dynamics, and features at various spatiotemporal levels ranging from the morphology of the colony to dynamics of single swarming cells. However, almost no research has looked into the lag time in swarms where after inoculation, it is speculated that cells in the inoculum extract fluid from the substrate to replicate either until a quorum is reached or a chemical signal initiates collective motility [2]. Typically, this lag time ranges from 1-3 hours depending on growing conditions and initial density.

Primarily, researchers have only quantified the lag time and studied what factors can abolish the lag time in *B. subtilis*. Kearns *et al.* has looked into density dependence and speculates that swarmer density is required to produce enough surfactant to reduce surface tension [3]. Secondly, it is likely that hyperflagellation is required as *B. subtilis* mutants with upregulated flagella production eliminates the lag time [4]. Finally, the lag time is abolished when swarming cells are taken from an active swarm and re-inoculated onto fresh agar [2]. However, it must be taken into account that all research for this particular phenomena has been limited to *B. subtilis*. While some of these lag abolishing phenomena may work for others, the complexity of each swarming species makes it difficult to make correlations from one species to another.

Furthermore, little has been done on observing the transition from a small, low density colony to the initiation of swarming. This regime may be important to understanding how small populations survive and proliferate, even when there is no quorum. As mentioned previously, swarming initiates based on density, surface tension, hyperflagellation, and substrate properties but these properties have only been correlated to already swarming colonies or single cell, static images that can only capture a few of these properties [5]. It is unknown if single cells initiate swarming based on one or multiple of these factors. Therefore, it is of importance to properly study the full temporal features of a swarm from single cells to a full colony at high-spatiotemporal resolution.

In this chapter, I describe a method/workflow to culture and image growing bacteria cells in small, polydimethylsiloxane (PDMS) chambers. Section 4.2 describes the protocols to create chambers, bacteria cultures, how to set up the imaging platform, and relevant equations for analysis of our desired cell features. Section 4.4 details how I post-process images in preparation for feature extraction. This entails contrasting, region of interest (ROI) selection, and background subtraction. Section 4.5 goes into the Feature Assisted Segmenter/Track (FAST) designed by the Durham group that allows for a user-friendly way to segment cells in a cluster from one another [6]. This program allows us to extract data about cell morphology such as cell lengths, cell widths, and cell orientations. This chapter concludes with section 4.6, where I go into how to utilize the data to extract individual cell data that was obtained from FAST in section 4.5, process the data for any erroneously recorded data, and use that data to obtain length, width, and aspect ratio distributions, as well as calculate a scalar order parameter.

4.1.2 Material properties of bacteria colonies affect strategy and dynamics

As described in **chapter 1**, swarming colonies exhibit many aspects of out-of-equilibrium, active matter systems that behave as non-Newtownian fluids. Swarmers move on to of a fluid layer, and their multi-layered activity may be described as a non-Newtonian fluid. One key aspect of swarming colonies that has been difficult to explore is understanding the mechanical properties of the swarm as the mechanical properties have implications colony response mechanisms, cell motility, and bacteria patheogenesis [7, 8]. Recently, it has been shown that bacteria swarms are non-Newtonian and show properties that can be measured via rheology [9] Various methods are available, ranging from "top-down" studies (bulk rheology, microrheology, atomic force microscopy), where colonies are probed by external means, and "bottom-up" studies (altering substrates and imaging cell behavior or probing the substrate via traction force microscopy), where the behavior of the colony or the effect of the colony is measured against the properties of their environment [10, 11, 12, 13]. What is currently clear is that the macroscopic colony shape and spreading rate is affected by substrate stiffness, but the exact mechanisms or how known mechanical properties impact bacteria on a single cell level is largely unknown [14, 15]. With this prior knowledge we want to understand how does the mechanical properties of the swarm dictate dynamics, expansion, and cell morphology? Particle and cell tracking have been previously used to understand local fluid flows and the rheological environment of active and biological materials including bacterial suspensions [16, 17], bacteria swarms [18], algal suspensions [19]. Particle tracking combined with traction force microscopy has also been used to extract viscoelastic and elastic material properties that are needed in computational and theoretical studies of biological matter [20].

To validate future use in bacteria swarms and swarms of *S. marcescens*, I use brightfield and florescence microscopy, high speed particle-tracking, and passive microrheology, to study the diffusion, transport and trapping of spherical tracer particles in a viscoelastic material: mucin, mucin-laden with various types of commonly used rock dust, and carboxylmethylcellulose (CMC). Having validated the methods and analysis, I present my analysis of tracer transport in reconstituted bare and dust-laden 10%mucin and discuss how these techniques may apply to bacteria swarms.

4.2 Validation of particle tracking methods to study non-Newtonian matter

4.2.1 Preparation of viscoelastic mucin and mucin loaded with anti-caking agent

The rock dust types used our study were: (1) unmodified limestone rock dust (MineBriteTM G; UCRD with mean particle size ≤ 74 μm), (2) modified limestone which is a moisture-tolerant rock dust, MTRD and has mean particle size 19.5 μm), and (3) crystalline silica (Min-U-Sil®10, SiO_2 with mean particle size 3.4 μm). Mucin samples (Sigma-Aldrich, Type III Mucin from porcine stomach, M1778) were prepared by mixing mucin granules with PBS to a final 10 wt% concentration (at pH = 7.3). This was set as our control system. Rock dust solutions were prepared by dissolving particles in Hank's buffer for 24 hours to a concentration of 1 mg/mL. The final formulations were: (a) (Mucin-CD) mucin with UCRD in solution, constituted by mixing 1 mg/ml of UCRD and 10 wt% mucin in DI water; (b) (Mucin-CD) mucin with MTRD in solution, constituted by mixing 1 mg/ml of MCRD and 10 wt% mucin in DI water; (Mucin-S) mucin with SiO_2 in solution, constituted by mixing 1 mg/ml of SiO_2 with 10 wt% mucin in DI water. In these experiments, pH was not varied and crosslinkers were not added to the mucin solutions.
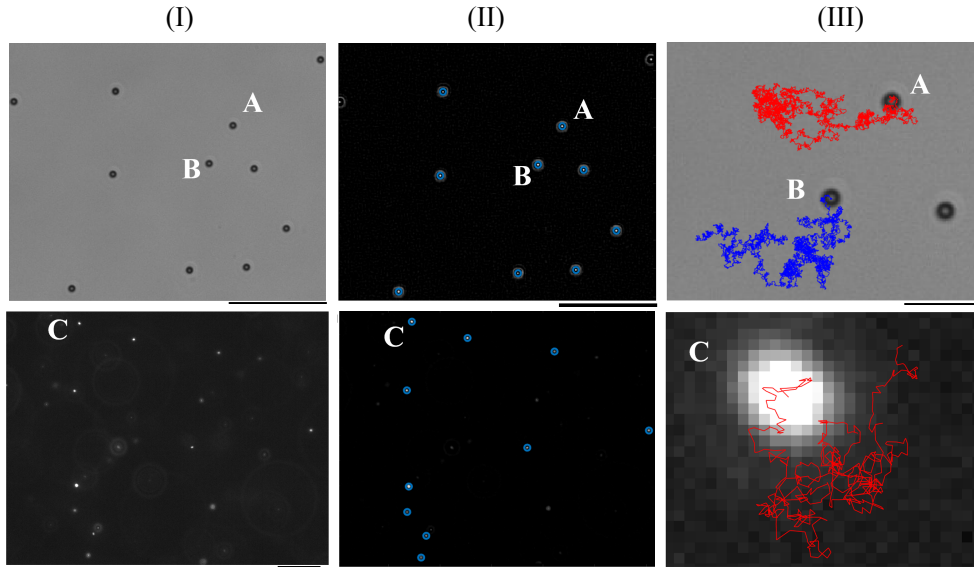
Figure 4.1: Spatiotemporally resolved particle tracking using brightfield microscopy for larger tracers, and florescence microscopy for sub-micron tracers. I show the three main steps in stitching and composing particle trajectory videos and image stacks from raw data. Trajectories are computed in the $x - y$ plane corresponding to the imaging focal plane. The top row illustrates the method for brightfield images, and the bottom row for images obtained using florescence. For each case, columns depict (I) tracer particle detection, (II) image filtering, and contrasting, and (III) trajectory construction. **(I, top)** The original image of 2.29 μm Spherotech polystyrene tracer particles in DI water (Zeiss 200M Axiovert microscope, 40x/NA 0.75 objective, 30 fps, 30 ms exposure time. The total observation time = 600 s and temperature = 21°C). **(II, top)** Filtered image of (I, top) with automatically identified particles, following the Crocker-Grier algorithm. Bandpass filters ensure that particles are shown as bright spots against a dark background. **(III, top)** Two representative tracks from the particle tracking routine. **(I, bottom)** Original florescence microscopy image of 0.53 μm Spherotech fluorescent tracer particles in 90 kDa (CMC) solution (Zeiss 200M Axiovert microscope, 40x/NA 0.75 objective, 90 fps, 11 ms exposure time. Total observation time = 60 s). **(II, bottom)** Filtered image of (I, bottom). **(III, bottom)** Magnified image showing only trajectories of the particle identified as C.

4.2.2   CMC Sample Preparation

I used carboxymethylcellulose (CMC) from Sigma-Aldrich (MW = 250 kDa and DS = 0.7), although solutions with MW = 90 kDa were also tested. Homogeneous solutions with 0.5%, 1%, and 2% (in weight %) concentrations of CMC were formulated. CMC samples were prepared at 40°C and spun on a magnetic stir plate at 100 RPM for 48 hours. Samples were then allowed to rest for 1 hour prior to measurements to allow the network to relax.

4.2.3   Slide Preparation for particle tracking and microrheology

Imaging channels were designed with McMaster-Carr polyester plastic mounting tape (Product No. 75955A673) by folding the tape onto itself, and subsequent smoothing. This resulted in a well geometry that was ≈ 200 μm in depth. The imaging well was punched out from the folded tape with a 0.5 inch in diameter hole-punch and then affixed to a glass slide of dimensions, 25 × 75 ×1 mm (Fisher Scientific). For imaging experiments, 16μL of

sample solution was first pipetted into the well, then a cover glass slip (18×18 mm, 0.13 mm thickness, VWR) was placed over the sample and fixed by double-sided mounting tape. The tracer particles were diluted to 1:100 concentration in DI water and injected into the samples. The injected volume was small, relative to the inital volume of mucin solution such that local water content remained approximately the same.

4.2.4   Optical Setup for microrheology

For particle tracking and microrheology measurements, I used spherical florescent particles of diameter $a = 0.5 - 5$ μm (Spherotech, Nile Red, Excitation wavelength, $\lambda = 510$ nm), and also non-florescent Spherotech polystyrene particles of diameter $a = 0.5 - 5$ μm as tracers. A Zeiss 200m Axiovert microscope in brightfield mode (for larger tracers), and sometimes in fluorescence mode (for smaller sub-micron particles) was used to deliver high contrast images. Post loading, samples were allowed to equilibrate and data was recorded after 10 minutes. The motion of the tracer particles are subsequently captured for 1 to 10 minutes and are saved as AVI videos.

All images presented were taken with a Zeiss EC Plan-Neofluar 40x/NA 0.75 M27 (Working distance = 0.71 mm, Depth of Field = 1.09 μm) objective. Video was recorded using a Mako G-158B monochrome camera. Particles in mucin samples were imaged at 30 fps with 30 ms exposure time. Particles in CMC were imaged at 90 fps with 11 ms exposure. Video recordings were done with the imaging plane focused on the center plane of the rectangular channel ($\approx 100\mu$m away) to minimize hydrodynamic, surface, and capillary effects from the channel edge walls. The experiments were conducted at room temperature (21°C) measured with a Neulog temperature sensor (NUL-203).

4.2.5   Image filtering and pre-tracking processing

The particle tracking and filtering of images are based of Crocker and Grier's particle tracking algorithm adapted to MATLAB [21]. Accurate reconstruction of trajectories and particle tracking rely on particles being clearly distinguishable from the background such that the program can easily detect those particles. Images were pre-processed such that consistent contrast within each video was maintained.

Figure 4.1 illustrates the raw images of particles from experiments conducted using brightfield mode (Figure 4.1(I-III), top three tiles from left to right), and for experiments using florescent tracers (Figure 4.1(I-III), bottom three tiles from left to right). Images of individual tracer particles display concentric rings around them with decaying intensity (see the closeup in Figure 4.1(III), bottom). The central ring of this diffraction pattern, i.e., the Airy ring, has the highest intensity and was used to fit and calculate particle locations. The intensity profile of the Airy ring is approximated by the form [21, 22],

$$I(x,y) \approx I_0 \, \exp(-\frac{(x - x_0)^2}{2w^2}) \, \exp(-\frac{(y - y_0)^2}{2w^2}) \tag{4.1}$$

where I_0 is the peak intensity (amplitude) at the center, x_0 and y_0 are the coordinates of the intensity center, and w is the root mean square width. The resolution of the images and particles are limited by the Rayleigh criterion where if the center-to-center distance of the Airy rings is less than the diffraction limit, the particles cannot be considered as two separate, trackable particles.

Recorded images were processed such that background and undesirable artifacts were removed. The contrast was adjusted so that the particles are as bright as possible against the background and the image was converted to greyscale. Spatial bandpass filtering was used to
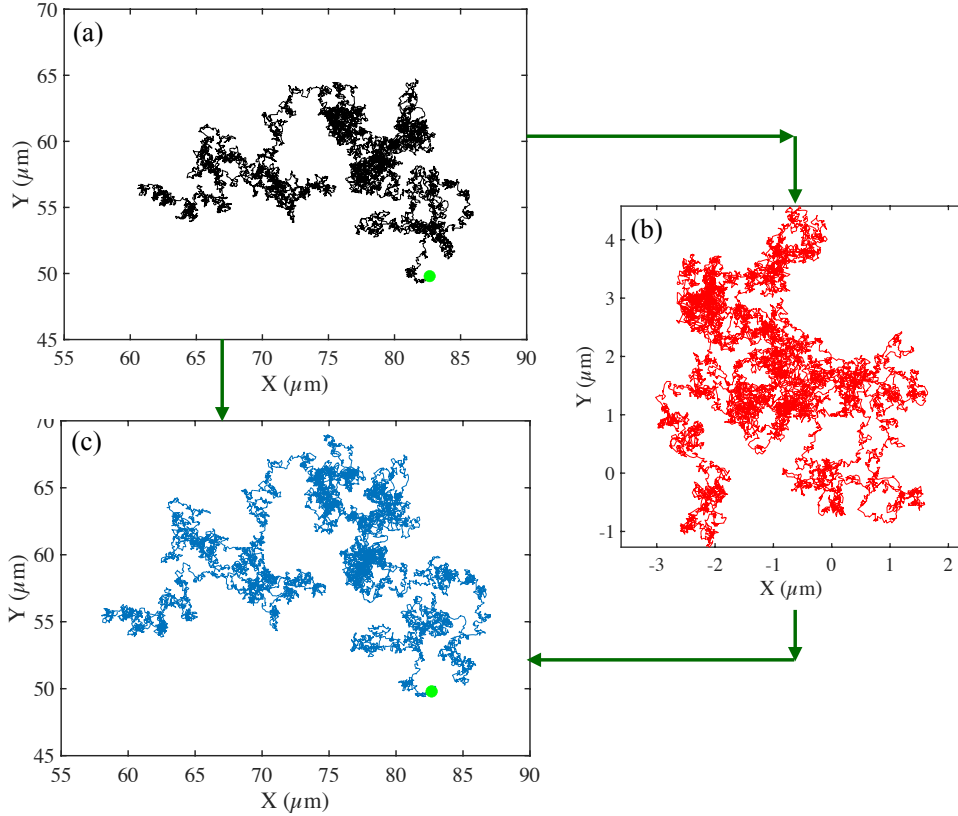
Figure 4.2: Example raw trajectory corrected for drift to obtain the final reconstructed trajectory. Trajectories are computed in the $x - y$ plane corresponding to the imaging plane. I show trajectory construction, and drift correction for the motion of a 2.29 μm tracer particle in DI water (from Figure 4.1, top) is shown. In **(a)**, I show the uncorrected particle trajectory, with the start of track indicated by the green circle. In **(b)**, the drift vectors are plotted for the full observation time (600 s). Here, drift acts as undesired translation of the particle, affecting its natural trajectory through a medium. In **(c)**, we plot the corrected track (trajectory) with drift subtracted out from the original trajectory. The start of track is indicated with the green circle. Images were taken on Zeiss 200M Axiovert microscope with 40x/NA 0.75 objective at 30 fps, 30 ms exposure time, and temperature = 21^oC.

remove bright spots present which did not fall within the particle size limits and any other features such as single, bright pixels, that are not particles. The centroids of the remaining bright features were then determined and particles below the diffraction limit were rejected. Some artifacts (non-tracers) remained as faint spots that were detected as real tracers by the algorithm. To remove these artifacts, images were filtered so that only particles above a brightness threshold remain were identified as real tracers. An example of this is illustrated in Figure in Figure 4.1(II)top and bottom: we see real tracers particles identified (in one frame) and marked with a blue circle.

Tracer trajectories are re-constructed by connecting a particle to the most likely corresponding particle at the next timepoint, taking into consideration the Brownian motion of non-interacting particles. For interacting particles in a particular frame, a time threshold is applied, where two particles are allowed to be un-resolved for a defined amount of frames (typically 2-5 frames, depending on particle size and when particles are stuck temporally as doublets) before they are discarded. A minimum squared displacement threshold is defined such as particles below that threshold are removed from the analysis (when particles stuck temporally as doublets). Finally, a memory function is defined to account for particles moving
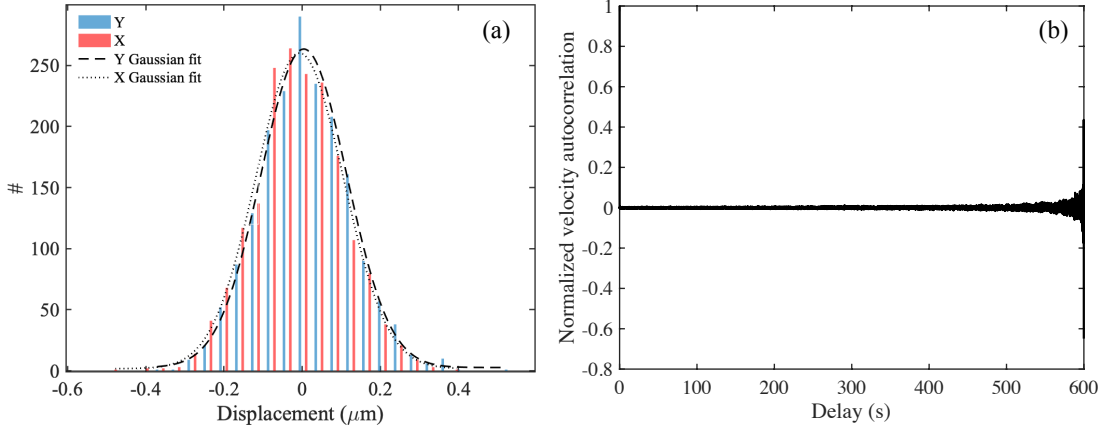
Figure 4.3: Analysis of tracer particle trajectories of the 2.29 μm tracer particles in DI water, a Newtonian fluid. **(a)** Histogram of (particle averaged, over single particle trajectories) translational displacements in x and y Cartesian coordinates as tracked from Figure 4.1, displaying a Gaussian distribution with zero mean and finite variance (equal for both x and y components) for the probability distribution of tracer displacements. Since particles undergo free Brownian motion, the variance is related to the diffusivity and the delay time over which the displacements are evaluated [23]). **(b)** The normalized velocity autocorrelation function as a function of delay time (in seconds) for trajectories recorded. The velocity autocorrelation is nearly zero, confirming the Brownian motion of the tracers in DI water. Large fluctuations for large delay times are due to a decreasing number of sample trajectories.

in-and-out of the focal plane. The memory function defines a maximum amount of frames an already detected particle may lose detection and re-gain detection. For example, a detected particle may leave the focal plane at time t_0 for 2 frames due to thermal noise and will not be detected for those 2 frames, but be detected in the subsequent frame (t_3); the memory function will declare that the particle at t_0 and at t_3 must be the same particle and will link the two detection spots together to generate a single track. Stitching together the positions of such identified particles provides the coordinates of the tracers in time and allows us to reconstruct the raw trajectories (the blue and the red curves) as shown in Figure 4.1(III).

Finally the raw trajectories were corrected for drift using a statistical model included in the particle tracking algorithm that employs velocity drift corrections (see Figure 4.2). Drift arises from various sources including small amplitude stage movement, sample leakage, building vibration, and thermal noise due to heating. A vibration-free stage was used with the microscope to minimize vibrations and bias.

4.2.6 Statistical Analysis

The ensemble averaged mean square displacement of tracers, averaged over a population of isolated tracer particles, as a function of delay time, τ (i.e., $\langle \mathrm{MSD}(\tau) \rangle$ is defined by:

$$\langle \mathrm{MSD}(\tau) \rangle = \frac{1}{N_\tau} \sum_{\alpha=1}^{N_\tau} [\mathbf{R}_\alpha(t+\tau) - \mathbf{R}_\alpha(t)]^2. \tag{4.2}$$

Here, $\mathbf{R}_\alpha(t)$ is the reference position (in $x-y$ coordinates) of tracer with index α at some time t along its trajectory, $\mathbf{R}_\alpha(t+\tau)$ is position of the same tracer at time $t+\tau$, and N_τ is the total number of particles (individual trajectories). Not all particles have the same value of the maximum delay time as some particles may leave the plane for the duration of imaging.

It is important to clarify that there are two types of averaging employed in Equation 4.2 to obtain the MSD. First is at the level of each tracer trajectory generated over an observation time t_F. Fixing a time delay τ, we calculate the square displacement for all possible pairs of time instances separated by τ and calculate an average MSD from these values. This MSD is then generated for all possible delay times along the full single trajectory to generate MSD(τ). The next part of averaging comes from taking an ensemble average of multiple tracer particles at delay time τ to then generate $\langle$MSD(τ)$\rangle$. Note that small delay times will have a larger number of trajectories while fewer trajectories are associated with large delay times and statistical error is expected to be larger for larger delay times.

Ensemble averaging hides possible spatiotemporal inhomogeneities that are associated with the ambient environment, in this case the mucin and CMC formulations. We analyze discrete probability distributions (histograms) of tracer displacements to better understand local transport properties (see Appendix). These histograms are obtained on a particle (or trajectory basis) and are averaged over the trajectory of a tracer *but are not averaged over particles/tracers.*

4.2.7 Velocity correlation, diffusion, and dispersion of tracers

To validate the tracking algorithm accurately tracks and reconstructs trajectories, I obtained displacement histograms at fixed delay times. For freely moving, and non-interacting Brownian particles, the ensemble average of displacement of is expected to be zero, and Gaussian with width determined by the tracer diffusivity and the delay time. Figure 4.3(a) shows one such histogram for 2.29 μm particles moving in DI water at 21°C. Here the x and y coordinates are measured in a fixed lab-frame and span the focal plane. As expected, the x and y displacement histograms of particles are similar since there is no directional bias to the motion that breaks $x - y$ symmetry. Both distributions are Gaussian with zero mean and identical width, confirm accurate trajectory reconstruction from detected particles.

The velocity of a Brownian tracer becomes uncorrelated with prior values as the moving particle moves along its trajectory in time and loses memory of its prior spatiotemporal position. The velocity autocorrelation function applied to a single tracer particle quantifies this:

$$v_{\text{corr}}(t) = \langle \frac{\mathbf{v}(t_0) \cdot \mathbf{v}(t_0 + t)}{|\mathbf{v}(t_0)|^2} \rangle \tag{4.3}$$

where t_0 is a suitable chosen initial reference time. The velocity correlation for 2.29μm polystyrene particles in water is shown Figure 4.3(b). A value of zero shows that the particle motion is uncorrelated and confirms a random walk motion where. The curve is normalized so that we get value of 1 for $dt = 0$.

The trajectory-averaged MSD of Brownian tracers are valid in the long time limit, and the ensemble averaged MSD are statistically identical with the same mean. This mean MSD is related to the particle diffusivity D and time t by the relationship [23]:

$$\text{MSD} = \langle\text{MSD}\rangle = 4Dt^{\gamma} \tag{4.4}$$

with $\gamma = 1$. Sub-diffusion is characterized by $\gamma < 1$ while superdiffusion corresponds to motion with $\gamma > 1$. The diffusivity D, for spherical tracers of diameter a moving in a Newtonian fluid at viscosity μ and temperature T is given by the Stokes-Einstein relationship

$$D = \frac{K_B T}{3n\pi\mu a} \tag{4.5}$$

where k_B is the Boltzmann constant and n is the dimension (this this case $n = 2$). Figure 4.4(a) shows individual tracer mean square displacement values calculated for each independent trajectory/track for 2.29 μm tracers in DI water. Ensemble averaging the values we obtain a
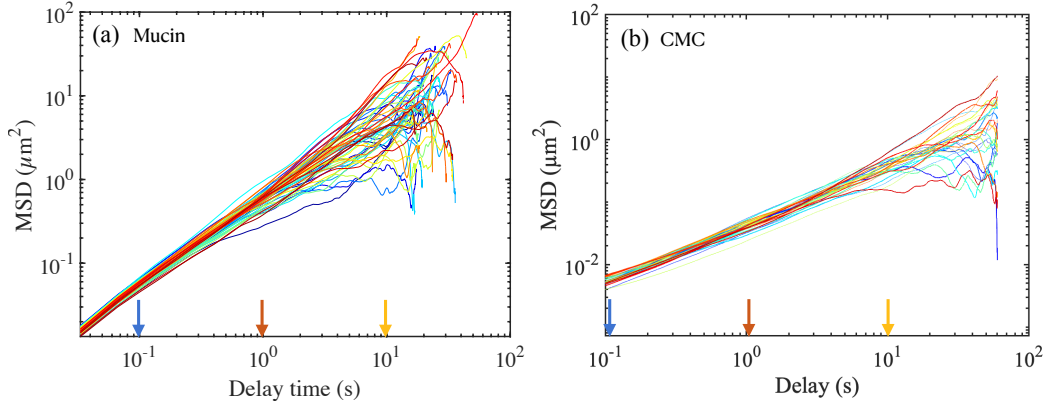
Figure 4.4: Single particle Mean Square Displacement (MSD) of tracers as a function of delay time for (a) unloaded 10 wt% mucin solution, and (b) a solution of CMC (concentration 1 wt%, MW 250 kDa). Tracer sizes are (a) 1 μm, and (b) 0.87 μm, and the number of tracks are (a) 157 and (b) 37, and for each the ensemble averaged value $\langle$MSD$\rangle(\tau)$ is calculated by averaging over the values at each τ. The power law exponent γ in the relationship MSD $\propto \tau^\gamma$ is 2 for a ballistically moving tracer, $\gamma = 1$ for freely diffusing tracer and $\gamma < 1$ for a sub-diffusing tracer. Also indicated are the three values of the delay time $\tau = 0.1$s, 1s and 10. Temperature = 21°C. The inset in (b) shows typical MSD's for a more concentrated 2% CMC solution obtained for a larger 2.11 μm tracer.

linear relationship between $\langle$MSD$\rangle$ and t confirming the freely diffusing motion of the particles. Note that the slope of the curve (or equivalently the value of the ensemble averaged MSD evaluated at some time $t = \tau$ can be used to estimate D for this particular tracer size. Alternately, knowing the temperature T and tracer diameter a, one can use Equation 6 to calculate the effective viscosity of the ambient medium.

4.2.8 Diffusion of tracers in viscoelastic CMC

The frequency dependent linear viscoelastic moduli can be calculated from the mean square displacements of the tracks to determine the surrounding material's elasticity and quantify rheological properties. Figure 4.4(b) shows sample MSD curves evaluated from trajectories of individual tracers in CMC solution at concentrations yielding properties consistent with viscoelastic materials. The CMC formulations correspond to solutions that are 0.5, 1, and 2% (weight/volume) and are expected to be increasingly viscoelastic. Tracers used were 0.87μm, and 2.11 μm diameter particles. The difference may be attributed to the viscoelastic behavior of the CMC at the higher concentration and to the sampling of larger network pore sizes and interaction with the entangled polymer network by the larger tracer particle.

The generalized Stokes-Einstein relationship (GSER) can be used to convert the MSD of the tracked tracer particles to provide the complex moduli in the frequency domain [24, 25, 26]. MSD(τ), can be converted to the Laplace (Fourier) frequency domains ($1/\tau$ where τ is the lag time, can be interpreted as frequency). The GSER is built on the principle of average motion of tracer particles in a continuum complex fluid, and is therefore valid provided macrostructural features are smaller than the tracer sizes. The frequency dependent version of the Stokes relationship effectively provides a measure of the viscoelastic drag on the tracer particles. Assuming local homogeneity and isotropy of the medium, this may be analyzed to obtain the complex shear modulus.

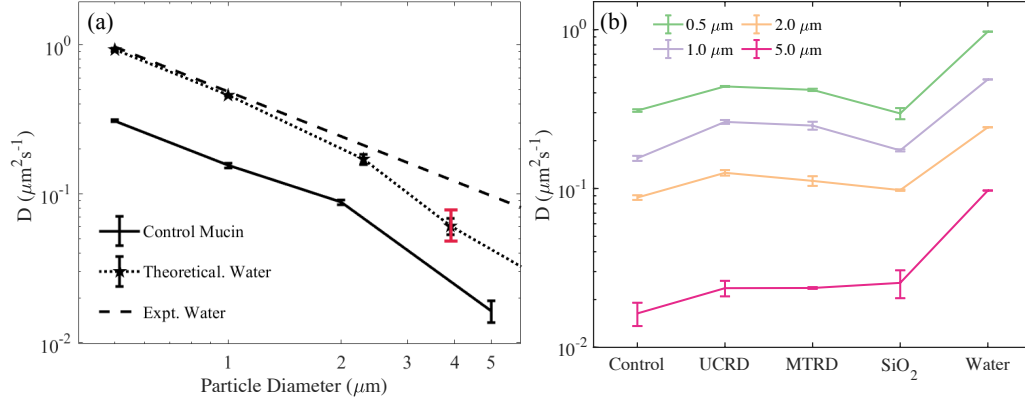The viscoelastic modulus $\tilde{G}(s)$ calculated from the unilateral Laplace transform of

Figure 4.5: Values of the effective tracer diffusivity estimated from particle tracking and trajectory analysis. **(a)** Experimentally estimated diffusivity of tracers in DI water (data connected by the dotted line) at a temperature of 25 °C. The theoretical result predicted by the Stokes-Einstein relationship is shown as the dashed line. There is excellent agreement for small to micron sized tracers. For the largest tracer $4-5$ μm, we observed a decrease in frequency deu to increased sedimentation effects that resulted in fewer trajectories and a concomitant larger statistical error. Error bars (black) correspond to 1 standard deviation. The red bar indicates the variation in results when the channel size was reduced by 15 % with tracers interacting more strongly with the walls of the channel. The control mucin solution behaves primarily as a viscous fluid for small tracer particles with an effective viscosity that is larger than DI water. Visual observations suggest that the largest tracers in these cases typically remained in the field of view but manifested a pronounced reduction in random motion **(b)** Estimated diffusivities of tracer particles 0.5-5 μm in diameter for the 10 wt% control mucin solution and 10 wt% mucin solution with dust and anti-caking additives. $\langle$MSD$\rangle$ for short to moderate delay times ($\tau < 3$s) was used to obtain a linear fit. Diffusivity were confirmed by estimating at $\tau = 1$s.

ensemble averaged MSD $= \langle \Delta \tilde{r}^2(s) \rangle$ is given by

$$\tilde{G}(s) = \frac{k_B T}{\pi R s \langle \Delta \tilde{r}^2(s) \rangle} \tag{4.6}$$

where k_B is the Boltzmann's constant, T is temperature, R is tracer particle radius, and $s = i\omega$ is Laplace frequency [27, 26, 28]. Following previously established theory, $\langle \Delta r^2(t) \rangle$ is expanded algebraically in a power law, and leading terms are retained to calculate the viscoelastic moduli. We use:

$$\tilde{G}(s) = \left. \frac{k_B T}{\pi R \langle \Delta r^2(s) \rangle \Gamma[1 + \alpha(s)]} \right|_{t=1/s} \tag{4.7}$$

$$\alpha(s) = \left. \frac{d\ln(\langle \Delta r^2(t) \rangle)}{d\ln(t)} \right|_{t=1/s} \tag{4.8}$$

$$\Gamma[1 + \alpha] \approx 0.457(1 + \alpha)^2 - 1.36(1 + \alpha) + 1.90. \tag{4.9}$$

The storage (elastic) modulus G', and the loss (viscous) modulus G'' may are obtained from Equation 4.8 by extracting the real and imaginary components, respectively. If $\alpha \approx 1$, we expect the tracer particle to be diffusive in isotropic Newtonian fluids. For tracer particles surrounded in a purely elastic medium that severely restricts their thermal motion, $\alpha \approx 0$ and the storage modulus G' is the leading term in the complex modulus.

Here, I validate the tracking algorithm and calculation of the MSD and complex moduli in viscoelastic mucin and CMC solutions. Swarming colonies and other active matter systems are suggested to behave as non-Newtonian fluids and their rheological properties are of interest as those properties may inform swarm strategy and have implications for patheogensis.
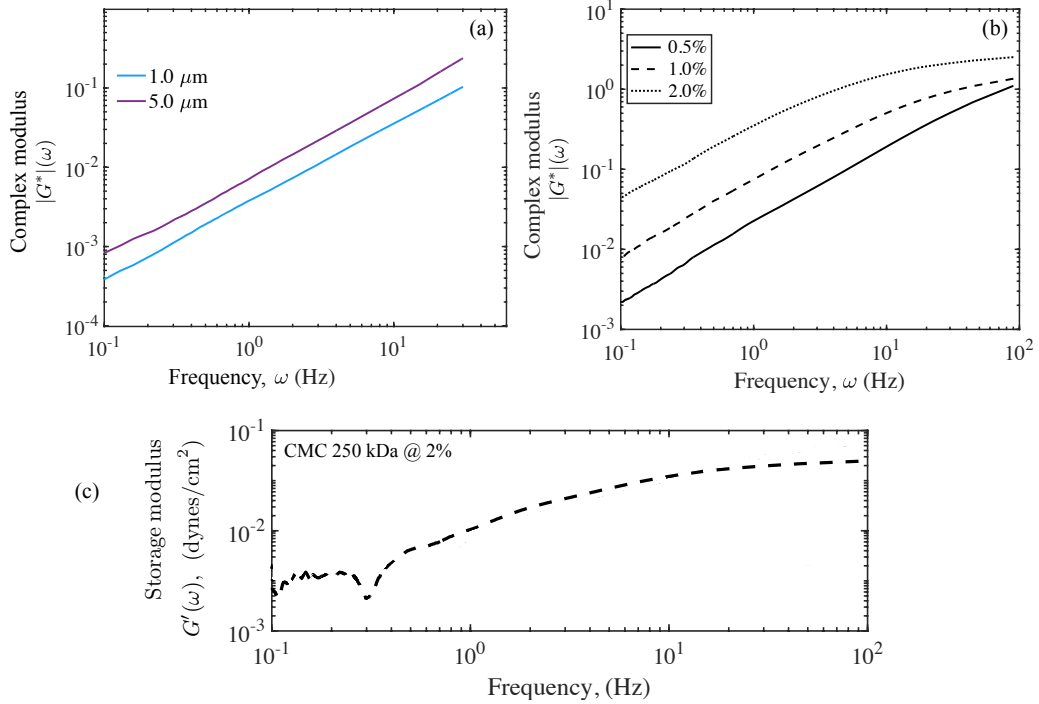
Figure 4.6: Magnitude of the complex moduli, $|G^*(\omega)|$, of the unloaded 10 wt% mucin (control sample), and of solutions of 250 kDa CMC at varying concentrations obtained using microrheology. **(a)** The Generalized Stokes-Einstein formulation was used to calculate the complex (G^*) moduli and its magnitude of control mucin using tracer sizes of 1.0 μm (blue), and 5.0 μm (maroon). For the small to moderate frequencies ω shown here, a nearly linear behavior is seen with frequency for both, indicating that the mucin solution is dominantly viscous. **(b)** Microrheology results for 250 kDa CMC solution at 0.5, 1.0, and 2.0% (w/v) for 0.87 μm tracers are shown here. The storage modulus $G'(\omega)$ and the loss modulus $G''(\omega)$ were also estimated separately for the CMC solutions, with significant elastic components suggesting strong viscoelastic response unlike for the 10% mucin solution. (c) The elastic modulus $G'(\omega)$ obtained from analysis of trajectories for 0.87 μm tracers.

Therefore, this methodology and algorithm may be used in future works to further study swarm's rheological properties.

4.3 Chamber preparation and imaging settings

4.3.1 PDMS Chamber Setup

PDMS chamber are fabricated in a 10:1 base-to-curing ratio with SYLGARD$^{\text{TM}}$ 182 Silicone Elastomer Kit. We mix 13.5 g of base with 1.5 g (total volume 15 g) of curing agent and slowly pour the mixture in a 100x15 mm petri dish. The PDMS is then placed in a vacuum chamber for at least 1 hour or until bubbles are removed. Then, the dish is placed in at 65 °C oven (Fisher Scientific IsoTemp oven) for at least 2 hours to cure. Once the PDMS has cured and solidified, concentric rings with an inner diameter of 15.9 mm and outer diameter of 25.4 mm are punched out using metal hole punchers. With this method, we fabricated PDMS rings with a height of 2 mm and a volume of $\approx$ 394 μL (1 mm^3 = 1 μL) which molten agar can be poured into and solidified for subsequent inoculation and imaging.

4.3.2 Agar Preparation

Agar samples were prepared as one would for microbiological studies by mixing media suitable for microorganism growth and motility studies [15, 18, 29] (in this paper we use Luria-Bertani media) and granulated agar. Agar samples were prepared by mixing Luria-Bertani media (0.5% m/v yeast extract, 0.5% m/v NaCl, 1% m/v Bacto Tryptone, in deionized water) and 0.5, 0.75, 1.0, and 2.0 m/v % Difco Bacteriological agar (Sigma-Aldrich, 214510). The agar solution was then autoclaved on the liquid cycle (Primus Sterilizer Co. LLC Autoclave, at least 121 °C at 20 PSI) to melt and sterilize the solution. Unused aliquots were stored in parafilmed 15 mL Falcon™tubes for up to 2 weeks. Aliquots were reheated in a 1550 watt microwave at 10 % power (Toshiba EM131A5C-BS) until fully melted and pipetted into the PDMS chambers for use.

4.3.3 Culturing methods

To prepare cultures of *Serratia marcescens* (WT ATCC 274) for experiments, we culture from frozen, -80°C glycerol stock in approximately 5 mL of Luria Broth media (LB media). We culture at 37°C and shake at 300 RPM overnight, until the culture reaches an OD600 of at least 0.5 to indicate that the culture is the exponential phase of growth. We then dilute the culture down to an OD600 = 0.01 to ensure we can capture individual cell growth and cluster formation as the experiment runs.

4.3.4 Imaging setup and chamber preparation

Due to the geometry of the Zeiss Axioimager.A2, only glass slides and the lid of 60x15 mm petri dishes fit under the objective. Larger dishes or imaging chambers either do not fit, are cumbersome to maneuver, or too tall for the working distance of most objectives. Other upright microscopes may not have this limitation. The PDMS chambers described previously are placed at the center of the lid of the 60x15 mm petri dish and pressed down upon to seal. No additional sealant is necessary. Then, the chamber is filled with ≈ 390 μL of molten agar and 8 μL of 25 % glucose solution. The lid is gently swirled to mix the solution and left to set for 10-15 minutes.

Once the agar is set, 1 μL of bacteria culture is pipetted at the center of the chamber and left to dry for 5-10 minutes (this allows the liquid culture to properly adhere to the agar and not slide around when being transported to the microscope. Once the culture is set, a coverslip (Corning No.1) is placed on top of the PDMS chamber and sealed by gently pressing the coverslip on top along the chamber walls.

Serratia has been shown to be sensitive to wide-spectrum light exposure as discussed in **chapters 1** & **2** [30, 18]. Therefore, consideration must be made for two factors (in regards to transmitted light microscopy): 1) Light intensity, 2) Exposure duration. Details regarding the appropriate intensity and duration have been reported in this dissertation, but briefly, exposure to wide-spectrum light under 40 s and intensities less than 220 mW should have no effect on the motility of *Serratia*. The imaging protocol presented here is well under the time and intensity thresholds.

4.3.5 Imaging methods

We image on a Zeiss Axioimager.A2 in PH1 with a 40x LD Achroplan (NA = 0.6, WD = 1.8 mm) with a corrective numerical aperture collar. The camera used was a Hamamatsu ORCA-Flash4.0 V3 Digital CMOS camera (C13440-20CU) Images are taken every 1 minute

over a duration of 7-9 hours at an exposure time of 100 ms and 10% relative intensity (84.7 $\mu W \cdot cm^{-2}$, measured at 535 nm, Thor Labs PM100D). Experiments were imaged at ambient room temperature (20-22 °C).

4.3.6 Scalar order parameter

To quantify how the alignment will change, we will measure the order parameter, S, of the colonies at different length scales as the microcolonies grow. The order parameter describes how aligned cells are with the mean orientation (referred to as the *director*) and is given by Eq.4.13. $S = 1$ describes a system where all cells in the domain are aligned with the director and $S = 0$ is a disordered system where orientations are isotropic [31]. The domain sizes will span from small clusters of cells ($\approx 2\mu m$ box), to the entire microcolony in order to capture both local and global ordering.

The orientation vector of the ith cell in the system at an angle ψ is given by:

$$\mathbf{P}_i = \cos\psi_i \mathbf{e}_x + \sin\psi_i \mathbf{e}_y \tag{4.10}$$

and define orientations from $+\frac{\pi}{2}$ to $-\frac{\pi}{2}$ as shown in figure 4.7.

The director/mean orientation over a domain is defined as:

$$\psi_{domain} = \frac{1}{N_{domain}} \Sigma_i^{N_{domain}} \psi_i \tag{4.11}$$

where i is the ith cell in the domain and N is the total number of cells.

We define $\langle\rangle_{\text{cells}}$ as the ensemble average of a cell cluster, that is to say, an average taken over the entire population of cells in a system. Similarly, we define an ensemble average over the entire viewable domain window (which can contain multiple clusters) as $\langle\rangle_{\text{domain}}$. All ensemble averages in this chapter are calculated as cell averages, $\langle\rangle_{\text{cells}}$ and drop the notation for the remainder of this text.

The order parameter will be evaluated at each individual cell i:

$$S_A = \frac{1}{2}\langle 3\cos(\theta_i)^2 - 1\rangle_{\text{cells}} \tag{4.12}$$
$$\theta_i = \psi_D - \psi_i$$

where A is the domain window centered at the centroid of the ith cell, θ is the angle between the ith cell's orientation and the director, ψ_D, and $\langle\rangle$ denotes an ensemble average of all cells within the specified domain A. The director is the average orientation of all cells within the domain window.

4.4 Post-processing of experimental images for analysis

High-quality images and analysis should come primarily come from good experimental setup and imaging settings. It is important to understand that to accurately resolve individual cells, proper preparation and understanding of what imaging settings to use will yield the best results. Post-processing/image editing cannot make-up the deficit from an improper setup. Keeping that in mind, post-processing of images for analysis can allow for more accurate cell
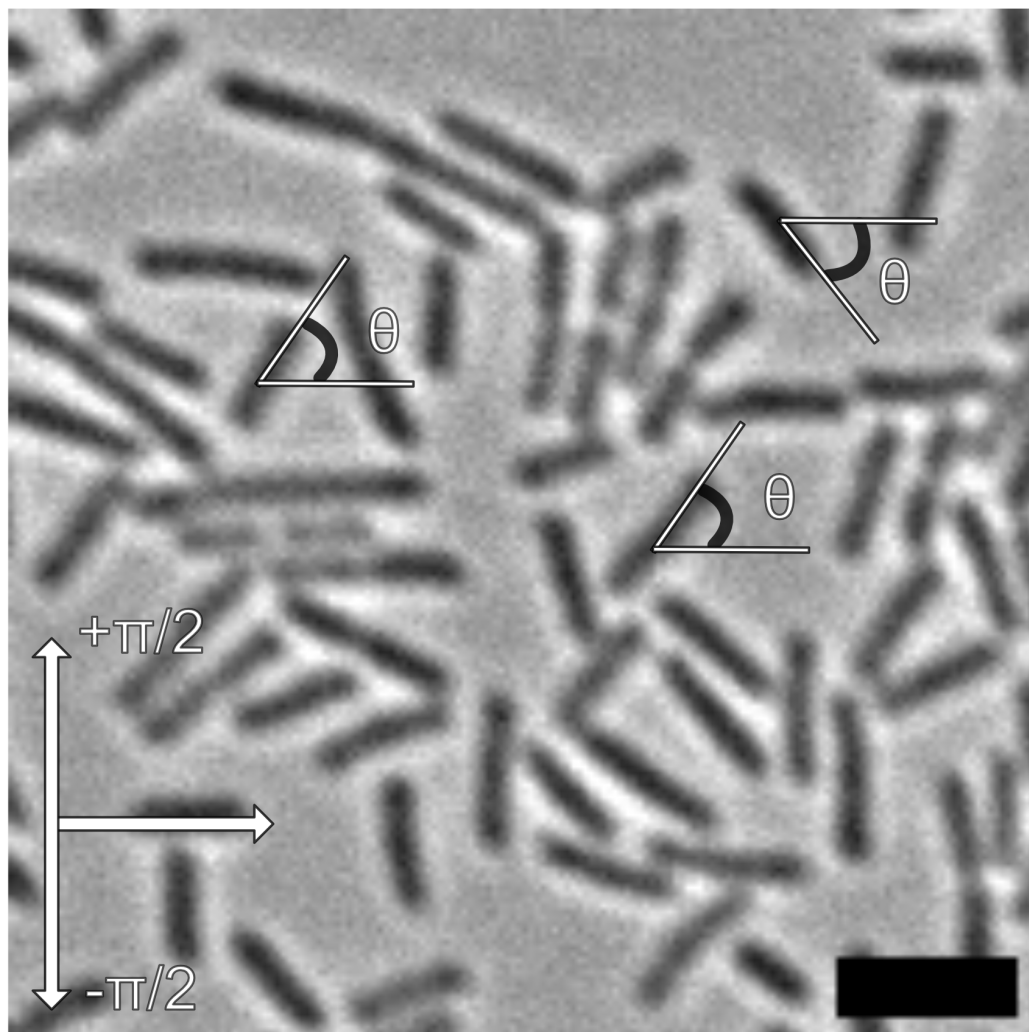
Figure 4.7: Schematic of how cells orientations (θ) are measured in FAST. Scale bar is 5 μm. Orientations that are measured in FAST measure from the positive x-axis and measure from $+\pi/2$ and $-\pi/2$.

detection as processing routines such as thresholding and background subtraction will better distinguish cells from the background and each other.

The steps for post-processing of images are as follows and are further classified by [Manual process], which requires full user input and [Semi-automated process] which does require some use input, but routines and functions are ran on the backend to process the image:

1. Identify region of interest (ROI) [Manual process]
2. Crop ROI from the rest of the image [Manual process]
3. Contrast the image stack to better resolve cells [Semi-automated process]
4. Apply background subtraction [Semi-automated process]
5. Save as ".ome.tif" extension

Firstly, we identify and crop the ROI as it is typically not reasonable to process the entire imaged region as the agar surface is uneven and while some regions are in focus, other regions may not be. Thus, to speed up processing and make later analysis easier, only crop the ROI (Fig. 4.8).

Figure 4.8: Selecting a cluster as a region of interest.

Then, we open up the Brightness/Contrast editing window and let the program automatically contrast our image stack (Image → Adjust → Brightness/Contrast → Auto → Apply).

From there, we apply a background subtraction by opening: Process → Subtract Background. From the sub-menu, we adjust the Rolling Ball Radius. The Rolling Ball Radius takes an average grayscale intensity from a circle of the specified radius and subtracts that value from the entire image with the goal of making the cells stand out more to the background. The appropriate radius depends on the size of your ROI, but typically values of 20 pixels and higher are sufficient and the preview window should be used to select the appropriate rolling ball radius. Once the background subtraction is applied, the background and foreground (cells) should look distinct from one another (Fig. 4.9).
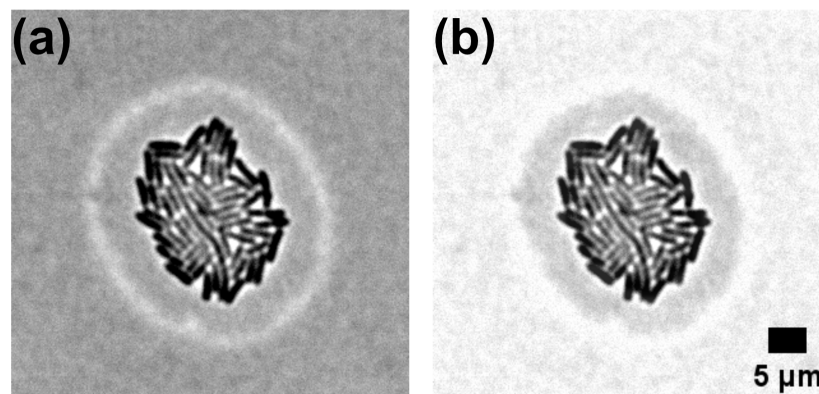

Figure 4.9: Applying contrasting and background subtraction to the image set generated from cropping in Fig. 4.8. **(a)** Raw image of a cluster of *S. marcescens.* **(b)** Processed image after contrasting and background subtraction. The resolution of the cropped cluster is 55.0x56.5 μm.

Finally, the image stack is saved as an ".ome.tif" extension (other formats are acceptable, see FAST documentation for other formats) as this is the recommended format for use with the Feature-Assisted Segmenter/Tracker described in the following section.

4.5 Segmentation and features from the Feature-Assisted Segmenter/Tracker

A longstanding problem that biologists encounter is processing images of dense systems of cells and discriminating cells in these systems in such a way that each cell can be tracked for the purposes of obtaining useful information such as cell position, cell length, orientation, etc. Various methods exist to detect individual cells and extract these features, but have costly computation times or a large amount of adjustable parameters that requires significant time to adjust [32, 33, 34].

The Feature-Assisted Segmenter/Track (FAST) [6] is a program designed to do such a task in a user-friendly manner. In the following sections, I briefly describe the modules used in FAST and the general values for the parameters. In-depth documentation and explanations are available through Meacock *et al.*, 2022 [6].

4.5.1 Required add-ons

The MATLAB variant of FAST requires the Bio-Formats package (Available at https://www.openmicroscopy.org/bio-formats/downloads/). Before using FAST, this package should be downloaded and added to your set path to ensure functionality of the FAST.

4.5.2 Opening FAST and loading your dataset

Once you have saved your dataset as an ".ome.tif" extension, the steps to upload are as follows:

1. Open FAST by typing *homePanel* into the command window
2. Click "Choose root directory" and navigate to the folder where your dataset is stored
3. If prompted, Upsample imaging data. This doubles the imported resolution for easier segmentation. This step takes longer for larger ROIs.

4.5.3 Segmentation and feature extraction

In the segmentation module, the user inputs values into an interactive GUI (Fig. 4.10) that illustrates: the size of detected objects and how foreground and background should be separated (texture), how cells in close proximity should be separated and discriminated against one another (ridge detection), how cells that have not been separated by ridge detection should be separated (watershed), and finally, filtering out spuriously detected regions based on size (segmentation area).
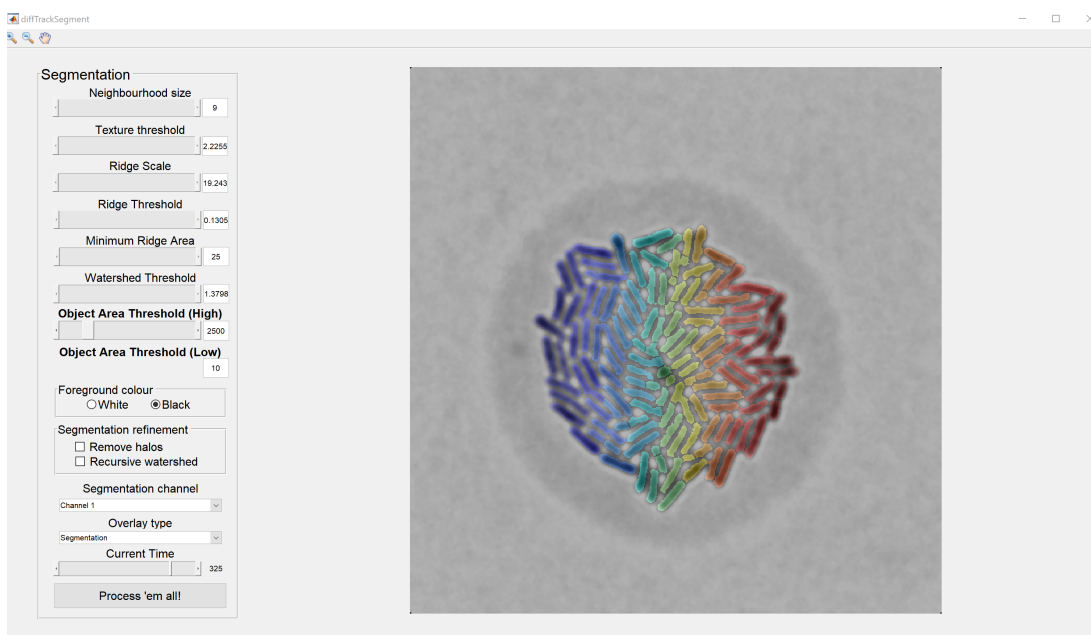

Figure 4.10: The GUI for the segmentation routine in FAST. Cells are individually color coded. The parameters are on the sidebar and are as follows: **Neighborhood size**: 9, **Texture threshold**: 2.2255, **Ridge Scale**: 19.243, **Ridge threshold**: 0.1305, **Minimum ridge area**: 25, **Watershed threshold**: 1.3798, **Object area threshold (high)**: 2500, **Object area threshold (low)**: 10.

The exact values for the parameters does depend on the domain size of the ROI, camera used for imaging, magnification, and lighting settings. When analyzing multiple datasets with varying domain sizes, the parameters will need to be adjusted accordingly. For example, looking at a growing colony at 100x as opposed to 40x will require vastly different values than what is shown. Similar changes will need to be made if the resolution of the image is different. If all subsequent datasets are taken with the same objective and imaging settings, the values for parameters do not change much. In Fig. 4.10, the values of each parameter are listed and would generally work for similar datasets, but always double-check the segmentation and adjust.

Ridge Detection: Ridge detection allows for separation of adjacent cells based on the ridge scale (how big the ridges should be), ridge threshold (allowable ridge size), and minimum ridge area (the smallest allowable ridge, useful for isolated cells or small cells relative to the mean size in the system). Figure 4.11 highlight how improper ridge detection settings affect highlighting of cells.
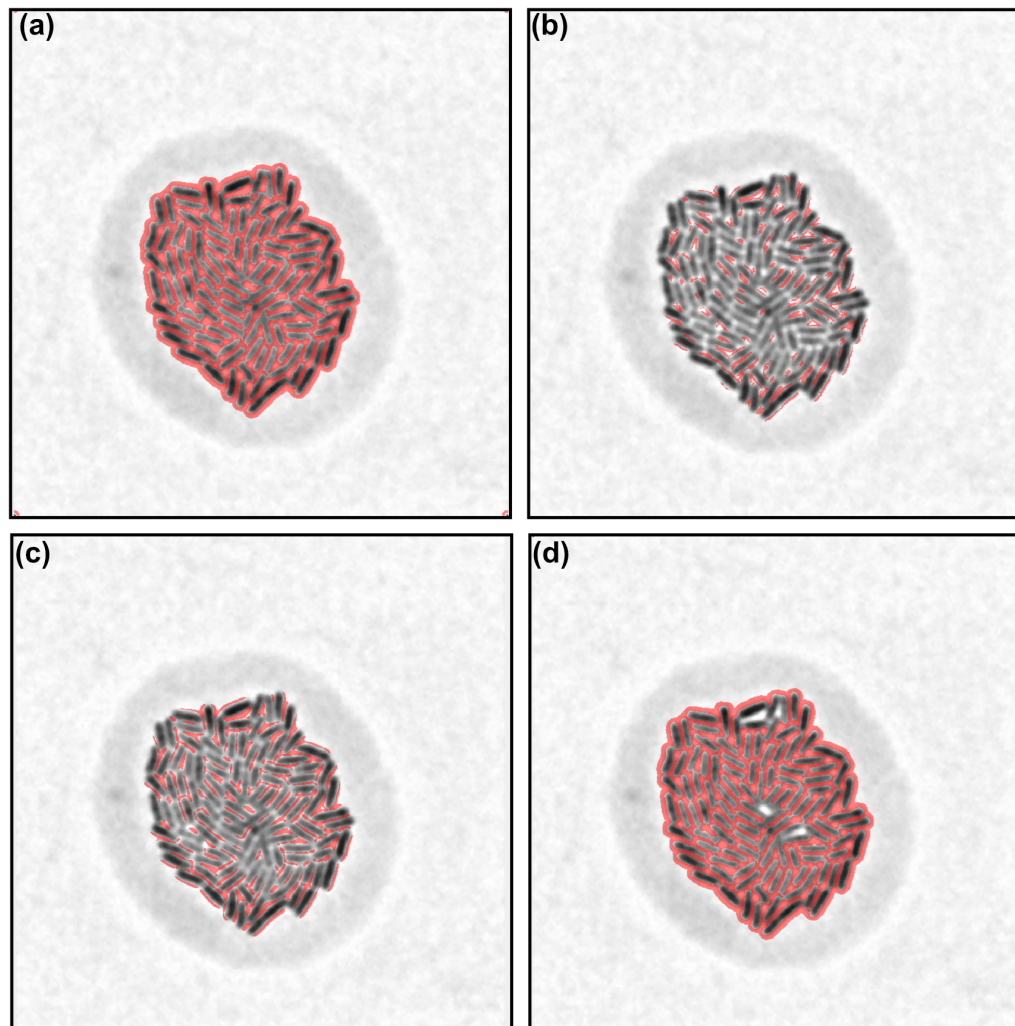

Figure 4.11: Ridge Detection settings. Red indicates where ridges are being formed by the program. Cells that are fully enclosed by ridge will likely be detected as a cell at the end of processing by FAST. **(a)** Properly set ridge settings outlining every cell in the cluster. **Ridge scale**: 19.24, **Ridge threshold**: 0.13, **Minimum ridge area**: 25. **(b)** Low ridge scale (Ridge scale = 10) only tracing small sections of cells, none of which are fully enclosed by a ridge. **Ridge scale**: 10, **Ridge threshold**: 0.13, **Minimum ridge area**: 25. **(c)** High ridge threshold (Ridge Threshold = 0.4) only tracing sections of the cluster. **Ridge scale**: 9.243, **Ridge threshold**: 0.4, **Minimum ridge area**: 25. **(d)** High minimum ridge area (Minimum ridge area = 100) where most cells are outlined, but a few large gaps exist (white spots where there should be red) **Ridge scale**: 19.243, **Ridge threshold**: 0.13, **Minimum ridge area**: 500. All other settings are the same throughout the figure and are as follows: **Neighborhood size**: 17, **Texture threshold**: 5.638, **Watershed threshold**: 1.379, **Object area threshold (high)**: 2500, **Object area threshold (low)**: 10.

Watershed: Watershedding separates cells picked up by ridge detection as occasionally, cells may be caught mid-division or may be too close to one another for ridge

detection to properly separate them. Therefore, the watershed slider allows for separation of these cells. Figure 4.12 highlights what too low of a watershed threshold can do, creating too many divisions within already detected cells and erroneously counting single cells as multiple cells.

Object area thresholding: After the previous steps are done, cells are detected and color coded in the segmentation window. Here, settings need to be adjusted in order to filter out as many erroneously detected cells as possible. Erroneous cell detection is due to imaging settings where some of the background is detected as foreground.

Object area threshold (high) sets the maximum allowed area (in pixels) for a cell. This can filter out large blobs around the periphery that are picked up, but can also filter out elongated cells if set too low. Object area threshold (low) sets the minimum allowed area for a cell. This setting can help filter out small spots that are picked up. Setting this too high can filter out cells that are small, but still relevant for analysis,

With the current imaging setup as described in the *Methods* section that requires constant refocusing of the objective, the imported images will include sections of images that are out of focus and appear as the background instead of the foreground and result in erroneously detected cells or missed cells (Figure 4.14). There are two avenues of approach to account for this. Firstly, manually removing images from the stack that are out of focus. This would yield in accurate datasets, however one will need a way to account for the temporal position of the remaining images as FAST and many other programs will assume a constant timestep between images. An alternative approach, and an approach further described in the following section in *MATLAB routines*, is to take advantage of the fact that poor detection results in low detection count and shapes that are not ellipsoids with high aspect ratios. Knowing that, one can run the segmentation will all images in the stack and remove timepoints that have low detection counts and remove individually tracked regions that do not resemble rod-like cells.

Finally, once the entire image stack has been analyzed, the next module "Features" can be used to obtain the length, width, orientation, cell area, and by proxy, the number of cells present at each timepoint, from the segmentation data. In the following section, I describe the various MATLAB routines designed to obtain statistics about the growing colonies from the features extracted from the Feature Assisted Segmenter/Tracker from the previous section.

4.6   MATLAB Routines

4.6.1   Loading extracted features from FAST analysis

In the previous section, I describe how segmentation settings are set in FAST, and what features are extracted from the dataset. These features are saved to the working directory as *CellFeatures.mat.* Your working directory will look something like Fig. 4.15. *Channel_1* is the stack of images imported into FAST. *Segmentations* are binary, segmented images of the stack. *CellFeatures.mat* is the data file with the saved lengths, widths, orientations, and cell areas at each timepoint. *Metadata.mat* is a data file storing the resolution, dt, and max time of your dataset. *SegmentationSettings.mat* are the settings applied in segementation settings in FAST (Fig. 4.10).

Cell counting and correcting for erroneous "cells"

At the end of the previous section, I describe two approaches to accounting for out-of-focus images in an image stack. Using the information that: 1) Out-of-focus images
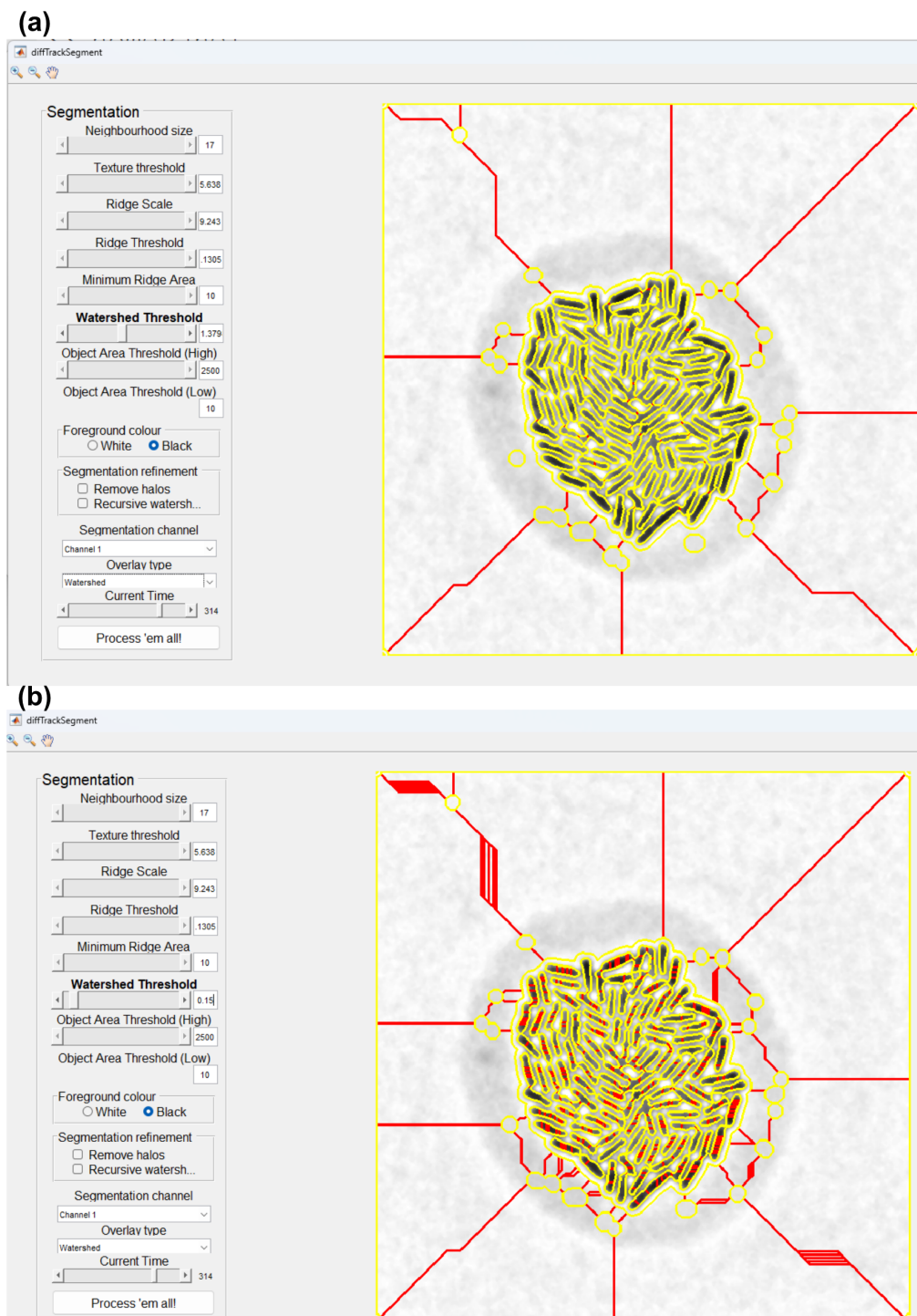
Figure 4.12: Watershed settings. **(a)** Properly set watershed settings that outline cells (in yellow) and divides cells that are too close to one another (red lines). While there are some erroneously selected cells with this setting, they are filtered out in subsequent processing steps. **(b)** Watershed settings that are too low (Watershed Threshold = 0.15). This leads to too many separations. For example, single cells should remain single cells, but due to the lowered threshold, single cells are cut up into multiple cells.

result in low detection counts, and 2) Erroneously detection regions do not typically look like rods, and therefore have low aspect ratios compared to detected cells.
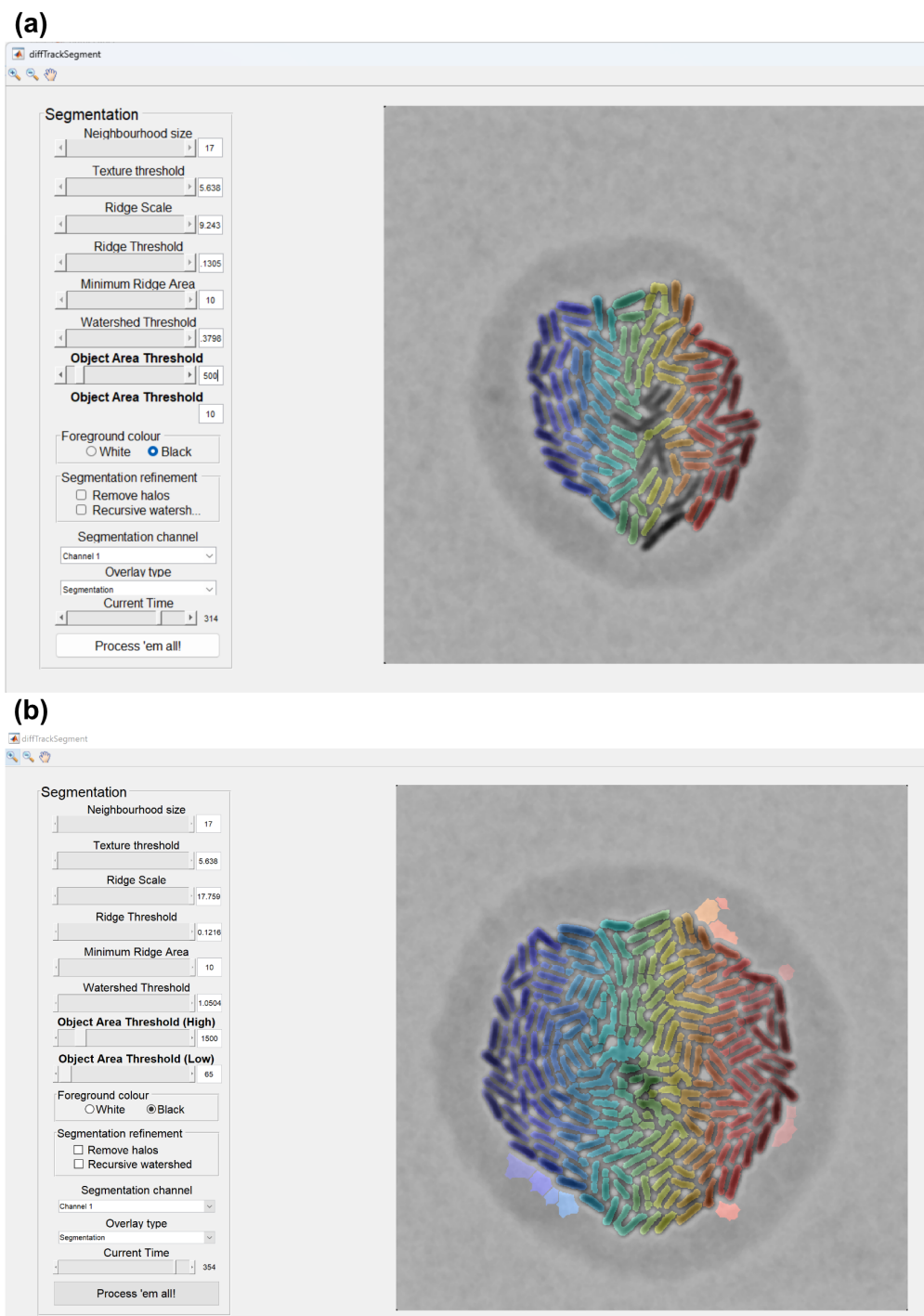
(a)

(b)

Figure 4.13: Object Area Thresholding. **(a)** Reduced object area threshold (high) (Object area threshold [high] = 500). While most cells are picked up by FAST, cells whose area exceeds 500 are left out. **(b)** Increased Object Area Threshold (low) = 500. Because this setting was increased, FAST only includes detected cells with an area over 500.

The MATLAB routine, *OrderParameter.m*, accounts for both before calculating the global and local order parameters. To account for low detection counts, we track the number of detected cells at each timepoint and filter out timepoint where the cell count decreases. We expect that the number of cells to increase as time passes (but not every timepoint), so any
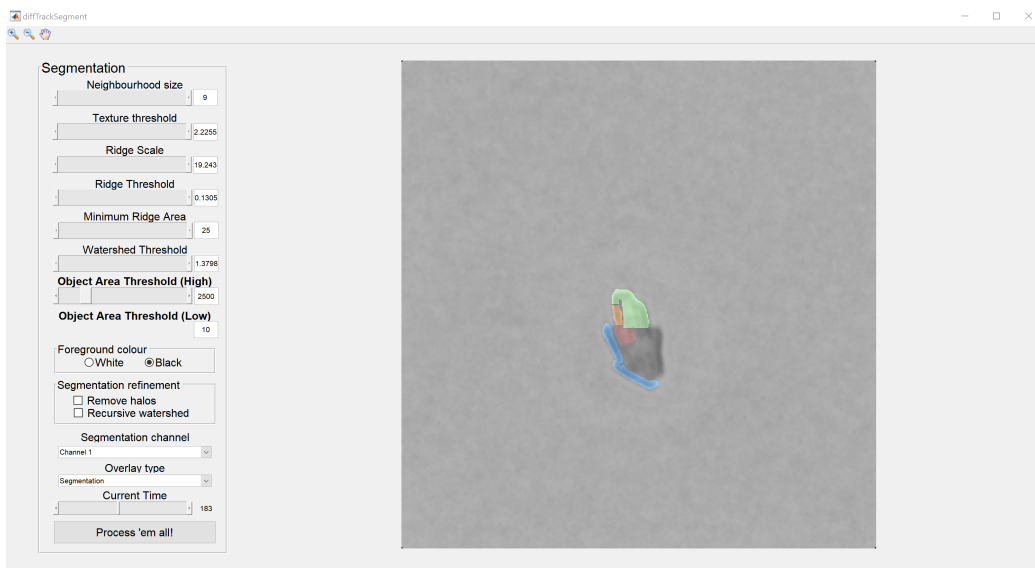
Figure 4.14: Using the same settings in FAST as in Fig.4.10, out of focus images will result in poor detection of cells.
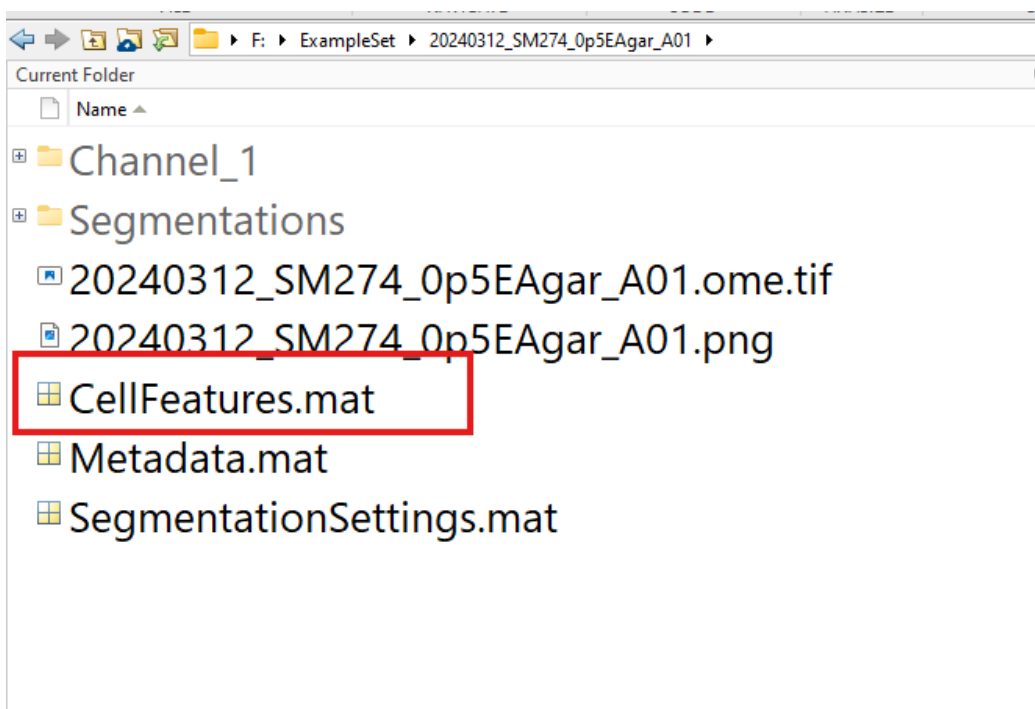

Figure 4.15: Snapshot of the what the working directory looks like once features have been extracted from FAST. CellFeatures.mat stores each cell length, width, orientation, and area.

decreases in cell count must be due to poor detection. After account for out-of-focus images, FAST may detect "ghost" cells, which are detected regions that satisfy the parameter criterion listed previously. These "ghost" cells can be seen in around the periphery of the cluster in Fig. 4.14. One can go back and fine tune settings to eliminate these, but care must taken as to not remove correctly detected cells. This becomes an even greater problem with datasets with many timepoints. These erroneous cells are not rod-shaped and look like circular blobs. We take advantage of this by calculating the aspect ratio of each detected cell and threshold the dataset

to include cells with aspect ratios above the set threshold (ARCutoff), which is typically aspect ratios greater than 2. The aspect ratio of the ith cell is calculated as: $AR_i = \text{Length}_i/\text{Width}_i$. After these two filtering steps are completed, the remaining code will calculate the local order parameters (Eq. 4.13, Fig. 4.17).
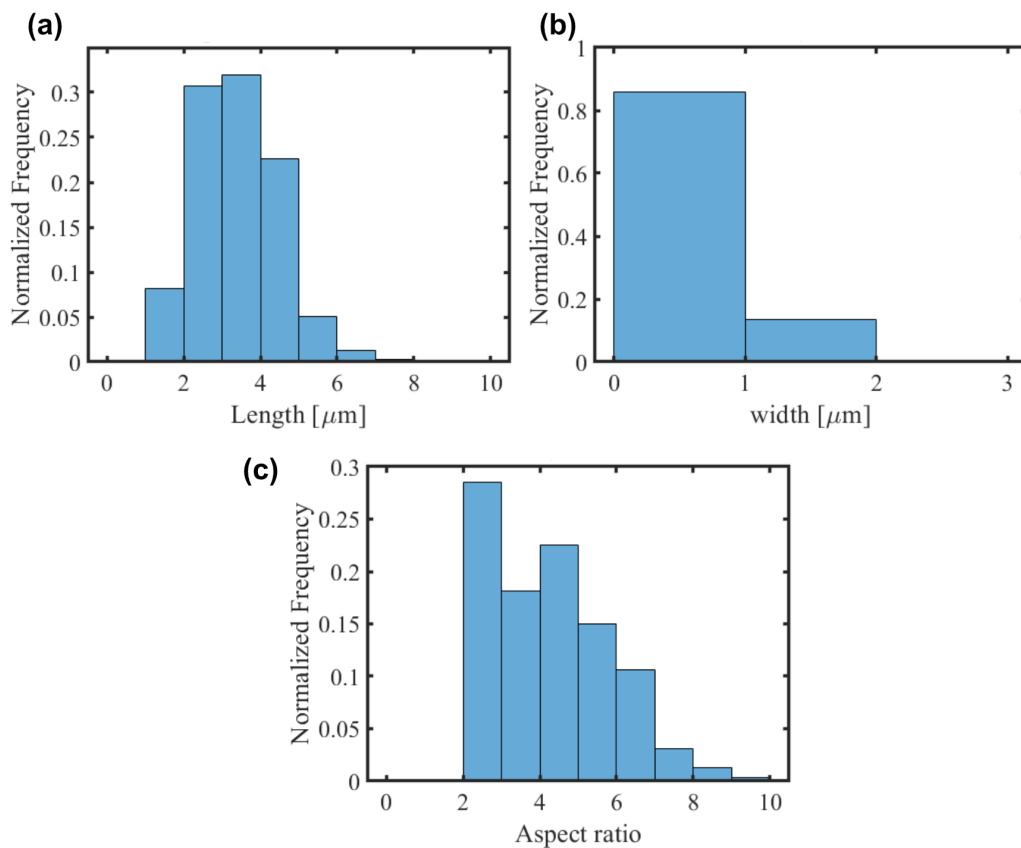

Figure 4.16: Statistics from the image in Figure 4.10. Statistics were taken oven N = 319 cells. **(a)** Length distribution. **(b)** Width distribution. **(c)** Aspect ratio distribution.
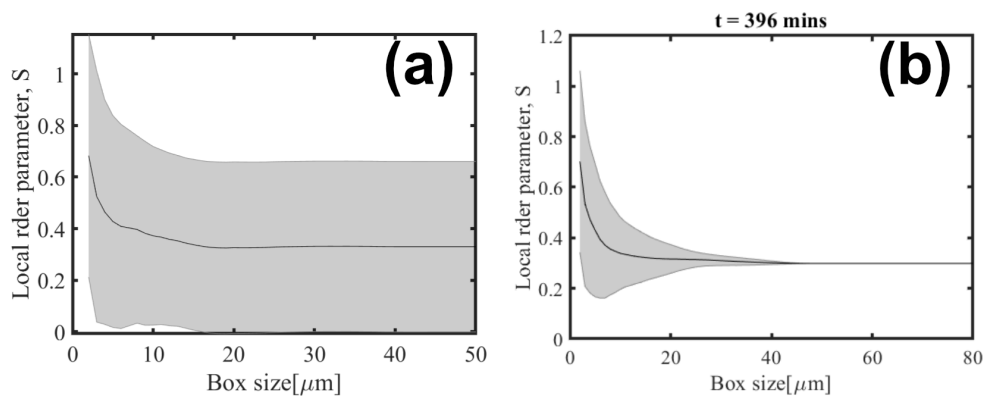

Figure 4.17: Local order parameters averaged over time **(a)** and at the last timepoint of the example dataset **(b)**. Grey shaded regions are 1 standard deviation away from the mean.

4.7 Conclusion

In this chapter, I presented a method/workflow to image a swarming strain of *S. marcescens* from an inoculum at immotile, low density to high density swarming and process the images to obtain useful statistics. Custom-made imaging chambers were made with PDMS in order to capture images with a specific microscope (Zeiss Axioimager.A2) but future research on this topic may be done on any range of microscope, provided that high resolution images can be taken at consistent intervals. For example, an inverted microscope or higher magnification objectives may increase the resolution of images and allow for more accurate segmentation and feature extraction. The images were post-processed to remove as much background noise as possible, then subsequently used in FAST to segment the cells. Multiple programs already exist in various programs and coding languages, but often these contain many parameters which may potentially increase the robustness of segmentation over FAST, but lack the ease of use and may be too difficult to reasonable learn and use. Finally, the segmented cells were analyzed with in-house MATLAB routines to obtain statistics from those segmented cells. These routines and statistics have potential in studying growing clusters, the pre-swarming phase of swarming bacteria species, and active nematic systems that resemble growing bacteria clusters.

Bibliography

[1] P. Kumar, J. Tamayo, R.-F. Shiu, W.-C. Chin, and A. Gopinath, "Size-dependent diffusion and dispersion of particles in mucin," *Polymers*, vol. 15, no. 15, p. 3241, 2023.

[2] D. B. Kearns, "A field guide to bacterial swarming motility," *Nature Reviews Microbiology*, vol. 8, no. 9, p. 634–644, 2010.

[3] D. B. Kearns and R. Losick, "Swarming motility in undomesticated bacillus subtilis," *Molecular Microbiology*, vol. 49, no. 3, p. 581–590, 2003.

[4] D. B. Kearns and R. Losick, "Cell population heterogeneity during growth of bacillus subtilis," *Genes & Development*, vol. 19, no. 24, p. 3083–3094, 2005.

[5] R. M. Harshey, "Bees aren't the only ones: swarming in gram-negative bacteria," *Molecular Microbiology*, vol. 13, no. 3, p. 389–394, 1994.

[6] O. J. Meacock and W. M. Durham, "Tracking bacteria at high density with fast, the feature-assisted segmenter/tracker," *PLOS Computational Biology*, vol. 19, pp. 1–26, 10 2023.

[7] Y. F. Dufrêne and A. Persat, "Mechanomicrobiology: how bacteria sense and respond to forces," *Nature Reviews Microbiology*, vol. 18, no. 4, p. 227–240, 2020.

[8] A. E. Patteson, M. E. Asp, and P. A. Janmey, "Materials science and mechanosensitivity of living matter," *Applied Physics Reviews*, vol. 9, no. 1, p. 011320, 2022.

[9] A. E. Patteson, A. Gopinath, and P. E. Arratia, "Active colloids in complex fluids," *Current Opinion in Colloid & Interface Science*, vol. 21, pp. 86–96, 2016.

[10] R. Bansil, J. Hardcastle, and M. Constantino, "Microrheology of mucin: Tracking particles and helicobacter pylori bacteria," *Epitoanyag - Journal of Silicate Based and Composite Materials*, vol. 67, no. 4, p. 150–154, 2015.

[11] M. D. Koch, M. E. Black, E. Han, J. W. Shaevitz, and Z. Gitai, "Pseudomonas aeruginosa distinguishes surfaces by stiffness using retraction of type iv pili," *Proceedings of the National Academy of Sciences*, vol. 119, no. 20, p. e2119434119, 2022.

[12] J. A. Kochanowski, B. Carroll, M. E. Asp, E. C. Kaputa, and A. E. Patteson, "Bacteria colonies modify their shear and compressive mechanical properties in response to different growth substrates," *ACS Applied Bio Materials*, 2024.

[13] M. E. Asp, M.-T. H. Thanh, S. Dutta, J. A. Comstock, R. D. Welch, and A. E. Patteson, "Mechanobiology as a tool for addressing the genotype-to-phenotype problem in microbiology," *Biophysics Reviews*, vol. 4, no. 2, p. 021304, 2023.

[14] A. Yang, W. S. Tang, T. Si, and J. X. Tang, "Influence of physical effects on the swarming motility of pseudomonas aeruginosa," *Biophysical Journal*, vol. 112, no. 7, p. 1462–1471, 2017. This paper is of interest because it tells us different factors of the substrate that affect swarming.

[15] M. E. Asp, M.-T. Ho Thanh, D. A. Germann, R. J. Carroll, A. Franceski, R. D. Welch, A. Gopinath, and A. E. Patteson, "Spreading rates of bacterial colonies depend on substrate stiffness and permeability," *PNAS Nexus*, vol. 1, no. 1, 2022.

[16] A. E. Patteson, A. Gopinath, M. Goulian, and P. E. Arratia, "Running and tumbling with E. coli in polymeric solutions," *Scientific Reports*, vol. 5, no. 1, p. 15761, 2015.

[17] A. E. Patteson, A. Gopinath, P. K. Purohit, and P. E. Arratia, "Particle diffusion in active fluids is non-monotonic in size," *Soft Matter*, vol. 12, pp. 2365–2372, 2016.

[18] J. Yang, P. E. Arratia, A. E. Patteson, and A. Gopinath, "Quenching active swarms: effects of light exposure on collective motility in swarming Serratia marcescens," *Journal of The Royal Society Interface*, vol. 16, no. 156, p. 20180960, 2019.

[19] B. Qin, A. Gopinath, J. Yang, J. P. Gollub, and P. E. Arratia, "Flagellar kinematics and swimming of algal cells in viscoelastic fluids," *Scientific Reports*, vol. 5, no. 1, p. 9190, 2015.

[20] A. Vaziri, A. Gopinath, and V. Deshpande, "Continuum-based computational models for cell and nuclear mechanics," *Journal of Mechanics of Materials and Structures*, vol. 2, no. 6, p. 1169–1191, 2007.

[21] J. C. Crocker and D. G. Grier, "Methods of Digital Video Microscopy for Colloidal Studies," *Journal of Colloid and Interface Science*, vol. 179, no. 1, pp. 298–310, 1996.

[22] B. Zhang, J. Zerubia, and J.-C. Olivo-Marin, "Gaussian approximations of fluorescence microscope point-spread function models," *Appl. Opt.*, vol. 46, pp. 1819–1829, Apr 2007.

[23] H. Berg, *Random Walks in Biology*. Princeton paperbacks, Princeton University Press, 1993.

[24] T. Gisler and D. A. Weitz, "Tracer microrheology in complex fluids," *Current Opinion in Colloid & Interface Science*, vol. 3, no. 6, pp. 586–592, 1998.

[25] T. G. Mason, "Estimating the viscoelastic moduli of complex fluids using the generalized Stokes–Einstein equation," *Rheologica Acta*, vol. 39, no. 4, pp. 371–378, 2000.

[26] M. Gómez-González, "One-and two-point particle tracking microrheology of complex viscoelastic fluids," *University of California, San Diego*, 2015.

[27] J. C. Crocker and B. D. Hoffman, "Multiple-particle tracking and two-point microrheology in cells," *Methods in Cell Biology*, vol. 83, p. 141–178, 2007.

[28] T. G. Mason, K. Ganesan, J. H. v. Zanten, D. Wirtz, and S. C. Kuo, "Particle Tracking Microrheology of Complex Fluids," *Physical Review Letters*, vol. 79, no. 17, pp. 3282–3285, 1997.

[29] J. D. Partridge, "Surveying a swarm: Experimental techniques to establish and examine bacterial collective motion," *Applied and Environmental Microbiology*, vol. 88, no. 3, pp. e01853–21, 2021.

[30] A. E. Patteson, A. Gopinath, and P. E. Arratia, "The propagation of active-passive interfaces in bacterial swarms," *Nature Communications*, vol. 9, no. 1, p. 5373, 2018.

[31] L. S. Hirst, *Fundamentals of soft matter science*. CRC press, 2019.

[32] O. Al-Kofahi, R. J. Radke, S. K. Goderie, Q. Shen, S. Temple, and B. Roysam, "Automated cell lineage construction: a rapid method to analyze clonal development established with murine neural progenitor cells," *Cell cycle*, vol. 5, no. 3, pp. 327–335, 2006.

[33] A. Ducret, E. M. Quardokus, and Y. V. Brun, "Microbej, a tool for high throughput bacterial cell detection and quantitative analysis," *Nature microbiology*, vol. 1, no. 7, pp. 1–7, 2016.

[34] E. Meijering, O. Dzyubachyk, I. Smal, and W. A. van Cappellen, "Tracking in cell and developmental biology," in *Seminars in cell & developmental biology*, vol. 20, pp. 894–902, Elsevier, 2009.

Appendix

Example Dataset from Chapter 4

The example dataset and relevant analysisyy code (excluding the FAST program) is given in the attached folder. This corresponds to "20240312_SM274_0p5EAgar_A01".

FAST segmentation settings

1. Neighborhood size: 9
2. Ridge Scale: 19.243
3. Ridge threshold: 0.1305
4. Minimum ridge area: 25
5. Watershed threshold: 1.3798
6. Object area threshold (high): 2500
7. Object area threshold (low): 10

Trajectory histogram formulation

For each trajectory, we divide the overall displacement time history (from time $t = 0$ to the final time for which the trajectory exists) into intervals of τ. We then compute the squared displacement between reference times t_R and time $t_R + \tau$ repeating this exercise for all possible values of t_R. Thus by averaging over t_R, we obtain the trajectory averaged mean square displacement *for a single tracer* as a function of the delay time τ. We then bin the results using bin-widths of 0.05 μm^2 and generate a histogram using

$$\text{Probability}[\text{MSD}(\tau)] = \frac{n_i}{N}. \tag{.13}$$

Here, N is the total number of samples and n_i is the number of estimated samples (the number of MSD values) within a bin. Note that via this calculation, each trajectory (tracer particle) is assigned a mean value of a squared displacement for a delay time τ. The histogram merely provides the probability distribution from the many trajectories. Values and histograms are generated for 3 time increments $\tau = 0.1$, 1, and 10 s to assess the motility of particles within the networks at short and long time scales. All errors bars correspond to 1 standard deviation.

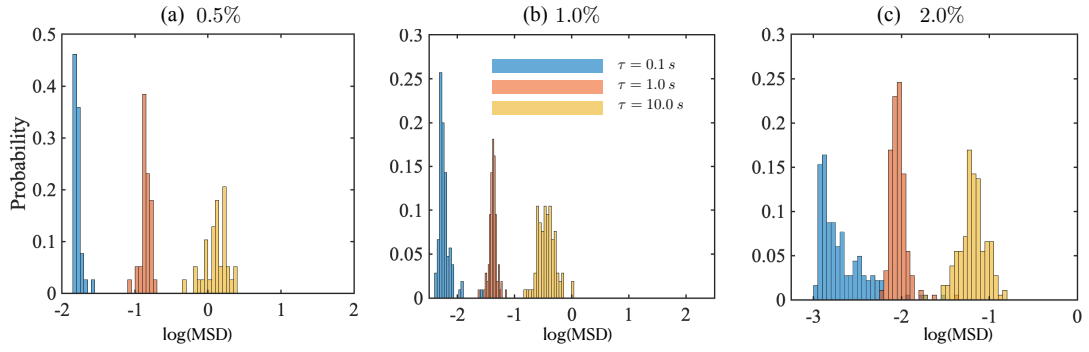Figure .18: Histograms denoting the discrete probability distribution of (trajectory averaged) mean square displacements (MSD) for 1 μm tracer particles in 250 kD CMC solution at three delay times $\tau = 0.1, 1, 10$ seconds. We show results for three CMC concentrations from 0.5% to 2%.
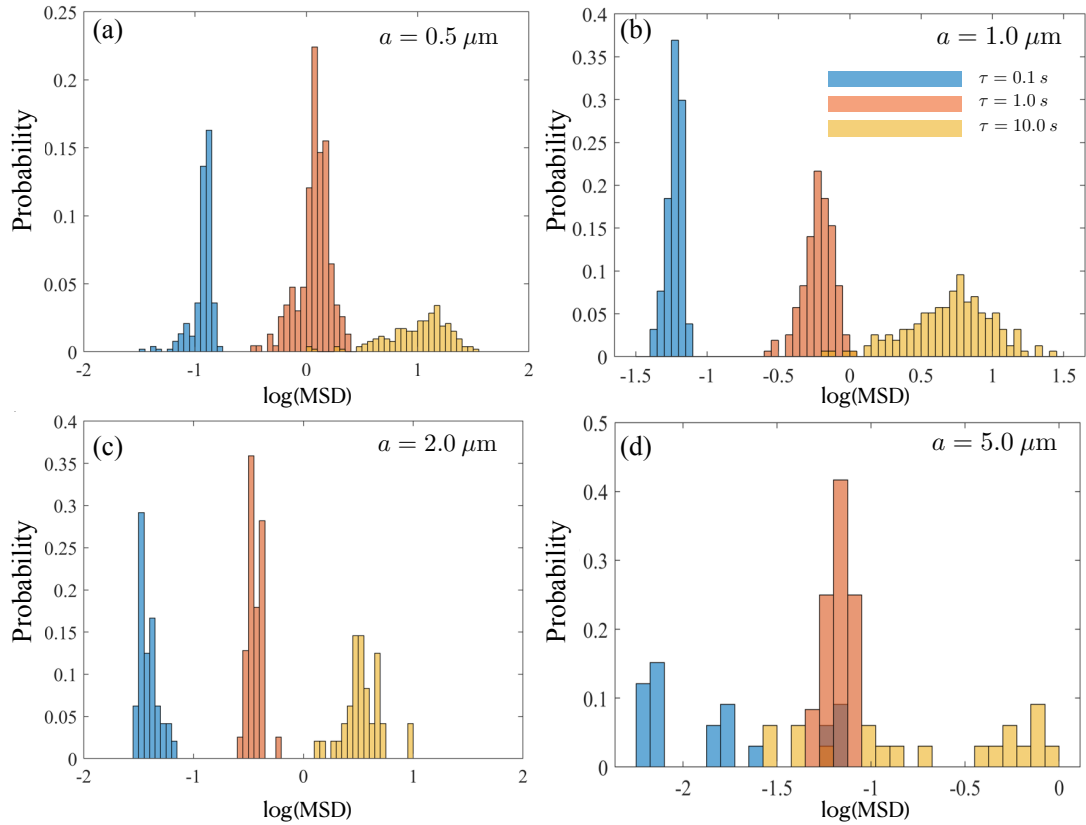

Figure .19: Histograms denoting the probability distribution of trajectory-averaged MSD, shown for the 10 wt% control mucin solution at delay times $\tau = 0.1, 1, 10$ seconds. We show data for $a =$ (a) 0.5 μm, (b) 1 μm, (c) 2 μm, and (d) 5 μm. For the largest tracer size of 5.0 μm, the variation in values is larger compared to smaller tracer sizes. The number of trajectories analyzed are (a) $N = 270$, (b) $N = 157$, (c) $N = 76$, and (d) $N = 20$. Images were taken on Zeiss 200M Axiovert microscope with 40x/NA 0.75 objective at 30 fps, 30 ms exposure time.